

Numerical Assessment on the Mechanical Performance of  
Pressure Pipe CIPP Liner with Local Defects in the Outer  
Host Pipe

by

Xiaoan He

A thesis submitted to the Faculty of Graduate and Postdoctoral  
Affairs in partial fulfillment of the requirements for the degree of

Master of Applied Science

in

Civil Engineering

Carleton University  
Ottawa, Ontario

© 2019, Xiaoan He

## Abstract

Due to technical, economic and logistical factors, cured in place pressure pipe (CIPP) liner systems have become one of the preferred options to rehabilitate damaged, ageing water pipe. There is a need to better understand the mechanical performance and limit states of the CIPP liner across a range of practical design parameters. In this study, the three-dimensional continuum finite element analysis was conducted to assess the effects of local defects in the host pipe on the mechanical performance of the CIPP liner subject to internal pressure, axial deformation and flexure loading conditions.

For a CIPP liner subject to internal pressure with local circular void defects in the host pipe, the limit state was governed by axial tension when the defect diameter to CIPP diameter ( $d/D$ ) ratio was greater than 0.4. A yield response was observed for the higher liner diameter to wall thickness ratios ( $D/t > 60$ ) and hoop stress to yield ratios ( $\sigma_h/\sigma_y \geq 0.6$ ). The effects of a circumferential gap defect on the CIPP liner mechanical response were evaluated. For internal pressure loading, the longitudinal distribution of normalized radial displacement for the CIPP liner was primarily influenced by the width of the circumferential gap defect width to CIPP liner diameter ( $g/D$ ) and the CIPP  $D/t$  ratio. The CIPP liner mechanical performance with circumferential gap defects in the host pipe when subject to internal pressure and pipe rotation was also investigated. The defect gap ratio ( $g/D$ ) had an impact on the CIPP liner deformation pattern. The host pipe/CIPP liner interface friction coefficient had a negligible effect due to the mobilization of a virtual anchor.

## **Co-authorship**

This thesis contains material prepared in the manuscript format. The principal investigator was Xiaoan He where he was the primary responsible person to define the problem statement, establish the analysis matrix used in the parameter study, develop the numerical modelling procedures, conduct the numerical simulations, and report on the data synthesis, analysis and conclusions. Guidance, mentorship and editorial support was provided by the supervisor, Dr. Shawn Kenny, in the development of the conference manuscript. The publication status (i.e. prepared for submission, submitted for review, accepted for publication) is stated in the preface of each manuscript.

## **Acknowledgements**

Firstly, I would like to thank my supervisor, Dr. Shawn Kenny for his guidance and support throughout my graduate studies. I appreciate the opportunity to work with such a knowledgeable and approachable professor in the geotechnical field. I never would have been able to complete this master program without the great patience and help he has given me. I hope I can apply all the knowledge obtained from him in my future career.

I would also like to thank my family, not only in the past two years but over my entire life. Without their continuous support, I would never have been able to accomplish anything.

Finally, I would like to thank all the friends I have made in past two years at Carleton University. This is a precious memory that I will never forget in my life.

# Table of Contents

<b>Abstract.....</b>	<b>ii</b>
<b>Co-authorship.....</b>	<b>iii</b>
<b>Acknowledgements .....</b>	<b>iv</b>
<b>Table of Contents .....</b>	<b>v</b>
<b>List of Tables .....</b>	<b>viii</b>
<b>List of Illustrations.....</b>	<b>ix</b>
<b>Nomenclature .....</b>	<b>xiii</b>
<b>Chapter 1: Introduction .....</b>	<b>1</b>
1.1    Background.....	1
1.2    Pipeline deterioration.....	3
1.3    Host Pipe Rehabilitation techniques.....	5
1.4    Limitations: Six potential limit states .....	9
1.5    Thesis Outline.....	10
<b>Chapter 2: Influence of Local Void Defect for Internal Pressure Loading.....</b>	<b>13</b>
2.1    Preface .....	13
2.2    Introduction .....	14
2.3    Finite element modelling procedures .....	19
2.3.1    Pipe Geometry, Modelling Considerations and Boundary Conditions .....	19
2.3.2    Numerical Procedures .....	22
2.4    Parameter study .....	26
2.4.1    Overview .....	26
2.5    Finite element predictions – influence of void defects .....	28

2.5.1	Variation in Liner Dimension ( $D/t$ ), Hoop Stress ( $\sigma_h/\sigma_y$ ) and Void Defect ( $d/D$ ) Ratios	28
2.5.2	Variation in the CIPP Liner/Host Pipe Interface Friction Coefficient ( $\mu$ )	36
2.6	Conclusions	38
<b>Chapter 3: Influence of Local Gap Defect for Internal Pressure Loading</b>		<b>41</b>
3.1	Preface	41
3.2	Introduction	41
3.3	Problem Statement and Study Objectives	45
3.4	Finite Element Modelling Procedures	46
3.4.1	Pipe Geometry, Topology and Boundary Conditions	46
3.4.2	Solution Procedures and Material Properties	48
3.5	Assessment of Gap Defects on CIPP Liner Mechanical Response	51
3.5.1	Parameter Study	51
3.5.2	CIPP Liner Stress	52
3.5.3	CIPP Liner Radial Deflection	55
3.5.4	Influence of Interface Friction Coefficient	60
3.6	Gap Defects Due to Relative Axial Motion	63
<b>Chapter 4: Influence of Local Gap Defect for Combined Internal Pressure and Flexural Loading</b>		<b>66</b>
4.1	Preface	66
4.2	Introduction	66
4.2.1	Problem Statement and Study Objectives	67
4.3	Finite Element Modelling Procedures	69
4.3.1	Pipe Geometry, Topology and Boundary Conditions	69
4.3.2	Solution Procedures and Material Properties	71

4.4	Assessment of Gap Defects on CIPP Liner Mechanical Response for Combined Loading.....	72
4.4.1	Parameter Study .....	72
4.4.2	Influence of Essential Boundary Conditions and Defect Gap Length .....	73
4.4.3	Influence of Loading Condition and Interface Friction Coefficient.....	88
4.4.4	Influence of Pipe Length.....	90
<b>Chapter 5: Conclusions and Recommendations .....</b>		<b>94</b>
5.1	Conclusions .....	94
5.2	Recommendations .....	98
5.2.1	Overview .....	98
5.2.2	Physical Modelling Studies.....	98
5.2.3	Numerical Modelling Studies.....	100
5.2.4	Engineering Practice .....	102
<b>References.....</b>		<b>103</b>
<b>Appendices.....</b>		<b>107</b>
	Appendix A Mesh topology, sensitivity and calibration studies .....	107

## List of Tables

Table 2.1 Orthotropic elastic material properties .....	22
Table 2.2 Parameter range assessed in this study .....	26
Table 2.3 Radial and through thickness location for maximum stress .....	36
Table 3.1 Orthotropic properties of Allouche et al., (2005) .....	44
Table 3.2 Orthotropic elastic material properties .....	49
Table 3.3 Parameter range assessed of 1829 mm .....	52
Table 3.4 Parameter range assessed of 152 mm .....	52
Table 3.5 Parameter range assessed of 152 mm in relative axial motion .....	64
Table 4.1 Parameter range for 152 mm CIPP liner pipe diameter .....	73
Table 4.2 Loading and interface friction study parameters .....	88
Table A.1 Numbers of elements used in each direction .....	109
Table A.2 Hoop stress through liner thickness .....	112

## List of Illustrations

Figure 1.1 Cracked pipes (After Seica et al., 2002).....	3
Figure 1.2 Failure modes (After Makar et al., 2001).....	5
Figure 1.3 Cross-section of woven hose (From AWWA) .....	7
Figure 1.4 Stress–strain curves for the exhumed and fabricated liners in the longitudinal direction (After Brown et al., 2008).....	8
Figure 1.5 Stress-strain curve for the fabricated liner in the circumferential direction (After Brown et al., 2008).....	8
Figure 1.6 Cross-section of exhumed cast iron pipe (After Brown et al., 2008).....	9
Figure 1.7 Six limit states (After Allouche et al., 2005).....	10
Figure 2.1 Principal geometric parameters for the CIPP liner and cast iron pipe with void defect.....	20
Figure 2.2 One-quarter model of CIPP liner and cast iron pipe .....	21
Figure 2.3 Stress-strain curves (After Brown et al., 2008).....	24
Figure 2.4 Anisotropic material properties based on Hill potential function .....	25
Figure 2.5 Normalized (a) axial, (b) hoop and (c) equivalent stress response with void ratio ( $d/D$ ) across a range of liner dimension ( $D/t$ ) and hoop stress to yield ( $\sigma_h/\sigma_y$ ) ratios for an un-bonded CIPP liner/host pipe interface ( $\mu = 0$ ) .....	30
Figure 2.6 Normalized radial displacement of the CIPP liner as a function of the normalized distance from the void center along the pipe length .....	34
Figure 2.7 Location diagram.....	36

Figure 2.8 Normalized (a) axial, (b) hoop and (c) equivalent stress response with void ratio ( $d/D$ ) across a range of liner dimension ( $D/t$ ) and hoop stress to yield ( $\sigma_h/\sigma_y$ ) ratios for a fully bonded CIPP liner/host pipe interface ( $\mu = 1$ ) .....	38
Figure 3.1 Circumferential crack (After Seica et al., 2002).....	43
Figure 3.2 Circumferential break.....	43
Figure 3.3 Principal geometric parameters for the CIPP liner and cast iron pipe with circumferential crack .....	45
Figure 3.4 One-quarter model of gap defect.....	47
Figure 3.5 Stress-strain curves (After Brown et al., 2008).....	50
Figure 3.6 Anisotropic material properties based on Hill potential function .....	51
Figure 3.7 Axial stress .....	54
Figure 3.8 Equivalent (Von Mises) stress.....	55
Figure 3.9 Thick-walled cylinder (From Ugural, A.C et al., 2003).....	56
Figure 3.10 Normalized radial displacement profile for $D=1829$ mm, $GAP=450$ mm, $\mu=0.4$ .....	58
Figure 3.11 Normalized radial displacement profile for $D=1829$ mm, $GAP=180$ mm, $\mu=0.4$ .....	59
Figure 3.12 Radial displacement for $D=1829$ mm, $GAP=180$ mm, $\mu=0.4$ , $D/t=50$ .....	60
Figure 3.13 Axial displacement profile ( $\mu = 0.4$ ) .....	62
Figure 3.14 Axial displacement profile ( $\mu = 0.2$ ) .....	62
Figure 3.15 Shear stress along pipe length .....	63
Figure 3.16 Maximum axial stress vs gap length of $D/t=35$ .....	65
Figure 3.17 Maximum axial stress vs gap length of $D/t=60$ .....	65

Figure 4.1 Rotation at ring fracture or pipe joint (After Allouche et al., 2005) .....	67
Figure 4.2 Principal geometric parameters for the CIPP liner and cast iron pipe with circumferential crack .....	68
Figure 4.3 One-quarter model of CIPP liner and cast iron pipe .....	69
Figure 4.4 Idealized models for the liner (A) Pin end (B) Roller end .....	71
Figure 4.5 True stress-strain curves in the axial and hoop directions.....	72
Figure 4.6 Liner ovality-global curvature relationship ( $L = 5D$ , $g/D = 10\%$ , $\sigma_h/\sigma_y = 0.8$ , $\mu = 0.4$ ) .....	74
Figure 4.7 Geometry of a segment of pipe .....	75
Figure 4.8 Total displacement contour of 5D case ( $g/D = 10\%$ , $\sigma_h/\sigma_y = 0.8$ , $\mu = 0.4$ ) .....	76
Figure 4.9 Ovality-global curvature relationship ( $g/D = 25\%$ , $\sigma_h/\sigma_y = 0.8$ , $\mu = 0.4$ ) .....	78
Figure 4.10 Total displacement contour of 5D case ( $g/D = 25\%$ , $\sigma_h/\sigma_y = 0.8$ , $\mu = 0.4$ ) ...	79
Figure 4.11 Normalized longitudinal distribution of liner section ovality ( $L = 5D$ , $g/D = 10\%$ , $25\%$ , $\sigma_h/\sigma_y = 0.8$ , $\mu = 0.4$ ) for the rotation angle of $15^\circ$ .....	80
Figure 4.12 Local moment-curvature relationship for the section at 0.5D ( $L = 5D$ , $g/D = 10\%$ , $\sigma_h/\sigma_y = 0.8$ , $\mu = 0.4$ ).....	82
Figure 4.13 Deformed modes (a) $g/D = 10\%$ for section collapse (Brazier effect) (b) $g/D = 25\%$ for local buckling mode.....	83
Figure 4.14 Normalized profile of different gap lengths ( $L = 5D$ , $g/D = 10\%$ , $\sigma_h/\sigma_y = 0.8$ , $\mu = 0.4$ ) .....	83
Figure 4.15 Ovality vs global curvature (Roller, $L = 5D$ , $g/D = 10\%$ , $25\%$ , $\sigma_h/\sigma_y = 0.8$ , $\mu = 0.4$ ) .....	84

Figure 4.16 Global moment-curvature (Roller, $L = 5D$ , $g/D = 10\%$ , $25\%$ , $\sigma_h/\sigma_y = 0.8$ , $\mu = 0.4$ ) .....	85
Figure 4.17 Ovality distribution at certain increments (Brazier effect) (Roller, $L = 5D$ , $g/D = 10\%$ , $\sigma_h/\sigma_y = 0.8$ , $\mu = 0.4$ ) .....	86
Figure 4.18 Ovality distribution at certain increments (local buckling) (Roller, $L = 5D$ , $g/D = 25\%$ , $\sigma_h/\sigma_y = 0.8$ , $\mu = 0.4$ ) .....	87
Figure 4.19 Profile of bottom edge (Brazier effect) (Roller, $L = 5D$ , $g/D = 10\%$ , $\sigma_h/\sigma_y = 0.8$ , $\mu = 0.4$ ) .....	87
Figure 4.20 Profile of bottom edge (local buckling) (Roller, $L = 5D$ , $g/D = 25\%$ , $\sigma_h/\sigma_y = 0.8$ , $\mu = 0.4$ ) .....	88
Figure 4.21 Local moment-curvature curves at the location of $0.5D$ (Pin, $L = 5D$ , $g/D = 10\%$ ).....	89
Figure 4.22 Ovality distribution of different cases (Pin, $L = 5D$ , $g/D = 25\%$ ) .....	90
Figure 4.23 Ovality vs global curvatures (Pin, $g/D = 10\%$ , $\sigma_h/\sigma_y = 0.8$ , $\mu = 0.4$ ).....	91
Figure 4.24 Ovality vs global curvatures (Pin, $g/D = 25\%$ , $\sigma_h/\sigma_y = 0.8$ , $\mu = 0.4$ ).....	92
Figure 4.25 Local moment-curvature curves (Pin, $g/D = 25\%$ , $\sigma_h/\sigma_y = 0.8$ , $\mu = 0.4$ ).....	93
Figure A.1 Comparison of Brown's results and S4R results .....	108
Figure A.2 Comparison of Brown's results and C3D8I results .....	108
Figure A.3 Comparison of Brown's results and the results of one layer model.....	110
Figure A.4 Comparison of Brown's results and the results of two layers model.....	110
Figure A.5 Comparison of Brown's results and the results of three layers model.....	111

## Nomenclature

Abbreviation or Symbol	Unit	Description
CIPP	#	Cured in place pressure pipe
$D$	mm	CIPP liner outside diameter
$t$	mm	CIPP wall thickness ratio
$d$	mm	Void diameter
$DR$	#	Ratio of the CIPP nominal pipe diameter to nominal wall thickness ratio
$\mu$	#	CIPP liner/host pipe interface friction coefficient
$t_p$	mm	External cast iron pipe wall thickness
$E$	GPa	Elastic modulus
$\nu$	#	Poisson ratio
$G$	Pa	Shear modulus
$\sigma_h$	MPa	Hoop stress
$\sigma_y$	MPa	Yield stress
$\sigma_u$	MPa	Ultimate stress
$\varepsilon_y$	%	Yield strain
$g$	mm	Host pipe wall of width
$u$	mm	Radial displacement
$a$	mm	Inner radius of pipe
$b$	mm	Outer radius of pipe
$r$	mm	Location at which the displacement is calculated
$p_i$	MPa	Internal pressure
$p_o$	MPa	External pressure
$u_r$	mm	Radial displacement of the liner
$u_t$	mm	Theoretical radial displacement
$U_{axial}$	mm	Axial displacement
$\alpha$	radian	Rotation angle
$M_R$	kN·m	End moment on the buried pipe
$M_L$	kN·m	Limiting moment on the compression face
$T_L$	kN	Axial tension
$L$	mm	Pipe segment length
$D_{max}$	mm	Maximum diameter of cross-section
$D_{min}$	mm	Minimum diameter of cross-section

$D_o$	mm	Nominal diameter of cross-section
$\kappa$	mm <sup>-1</sup>	Global curvature
$R$	mm	Radius of curvature
$\theta$	radian	Overall change of angle
$M_x$	kN·m	Moment with respect to x axis
$U_y$	mm	Y displacement of the liner
$U_{ymax}$	mm	Maximum Y displacement of the liner

# **Chapter 1: Introduction**

## **1.1 Background**

Pipelines such as energy pipelines and civil lifeline pipelines are critical elements of civil infrastructure within modern society. The safety and well-being of the general public highly depends on the service quality that the pipelines can provide. Due to the different working environment and material properties, the behavior of energy pipes and civilian pipes are quite different. This study will focus on the cast iron pipe for civilian application.

Cast iron pipes have been extensively used for water supply and sewage during the 19<sup>th</sup> and 20<sup>th</sup> centuries. As the pipes age, the deterioration mechanisms, such as environmental conditions (e.g. corrosion effects), non-uniform ground movement or unexpected loading events, affect the pipe performance. This may pose a threat not only to the integrity of the pipe line system but also to the safety of the public. A significant waste of the water through a deteriorated water distribution system is estimated as 10% to 30% of the total water supplied. At the same time, contaminants can penetrate through the leaks into the pipeline (Seica et al., 2002).

As a result, there is an increasing need for the rehabilitation of these pipelines, which can be categorised by two general approaches including (1) conventional open-trench and (2) trenchless methods. Jeyapalan, (2003) reported that over 50% of the rehabilitation work on sanitary, storm and combined sewers has been performed using trenchless

technologies while 90% of the repair work on water distribution system has used conventional digging techniques, which has caused physical disturbance to the streets as well as logistical and economic problems due to traffic disruption. Furthermore, more than 50% of the existing water pipe network in the United States comprises cast iron.

There are a number of important trenchless construction techniques for rehabilitating damaged pipes. These construction methods require less excavation so that the interruption to the community can be reduced significantly. American Water Works Association (AWWA) Manual M28 describes four typical types of trenchless techniques:

- (1) Spray-on Polymer Lining: Polymeric materials are sprayed on the inner surface of the old pipe to form a liner that eliminates pipeline internal corrosion.
- (2) Slip Lining: A new pipe is pulled inside the existing pipeline.
- (3) Pipe Bursting: A new pipe is pulled into the space created by breaking up the existing pipeline.
- (4) Cured-in-Place Pipe: A new pipe is formed within the host pipeline.

Compared with conventional open-trench replacement, the trenchless methods are more efficient, environmental friendly, cost-effective and less disruptive to the traffic. These attributes may influence decision making in the maintenance, repair or replacement of pipelines that do not meet serviceability requirements or result in emergency action due to pipeline failure.

## 1.2 Pipeline deterioration

Seica et al., (2002) conducted a three year study (1998 to 2000) to establish an improved understanding on the governing failure modes of Toronto region iron water mains through an evaluation of the pipe material and mechanical properties, and characterization of the surrounding soil characteristics. During the study, 100 pipe samples, comprising mostly cast iron, were exhumed and evaluated with respect to geometric properties, uniaxial tensile strength and ring bearing strength. For the cast iron water main samples, a circumferential crack, longitudinal crack, or combination of these two features were observed (i.e. Figure 1.1). From the geometrical assessment, over 95% of the samples suffered moderate to severe corrosion damage. The study suggested conventional cement-mortar lining material or trenchless technologies (e.g. cured-in-place plastic liners) could be used for the rehabilitation of deteriorated pipes. Results from the mechanical testing demonstrated the strength of cast iron pipes was influenced by corrosion due to the presence of stress concentration sites and cracks that reduced the pipe strength.



Figure 1.1 Cracked pipes (After Seica et al., 2002)

Makar et al., (2001) reported four main failure modes including blowout holes, circumferential cracking, bell splitting, longitudinal cracking (i.e. Figure 1.2). The root causes identified were corrosion, manufacturing defects, human error and unexpected loading levels. The study identified the tendency for smaller diameter pipes (i.e. lower second moment of area and flexural resistance) were more susceptible to longitudinal bending failures whereas larger pipes (i.e. greater second moment of area and flexural resistance) were more prone to longitudinal cracking and shearing at the bell joint. Rajani et al., (1996) observed similar failure modes characterized as circumferential break, longitudinal break or split, joint failure, corrosion holes and corporation cock failure. Circumferential break was associated with critical axial tensile stress, whereas longitudinal failure was due to hoop stress or in-plane bending action. Several probable mechanisms for imposing longitudinal tensile stress were identified including seasonal changes in the ground temperature, soil volume; particularly in sensitive clay, change due to variations in the water table and soil moisture content, and flexural action due to inadequate base support or expansion of clays underneath. Circumferential stress can be caused by the volume increase due to water freezing or unusual surge pressures.

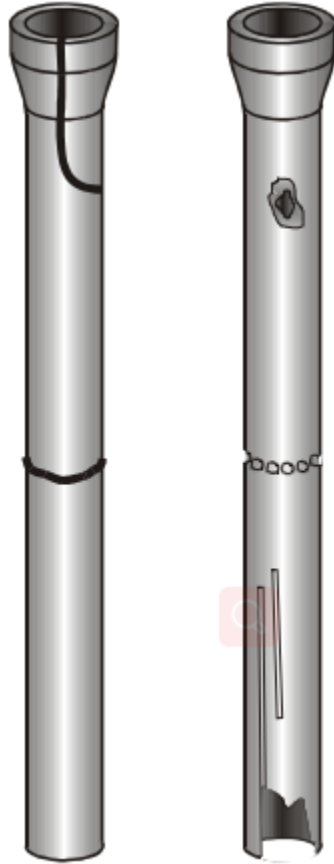


**Figure 1.2 Failure modes (After Makar et al., 2001)**

### **1.3 Host Pipe Rehabilitation techniques**

For rehabilitation techniques, Appendix A of the AWWA Manual M28 categorizes liners into four types according to the mechanical performance.

- Class I Liners: are “...nonstructural systems used primarily to protect the inner surface of the host pipe from corrosion...”; such as, cement–mortar lining and epoxy resin lining.
- Class II and Class III Liners: are interactive, semistructural systems with lower stiffness than the host pipe and transfer the internal pressure loads to the

external host pipe. The liner, however, carries internal pressure loads at local discontinuities in the host pipe. If the long-term (50-year) internal burst strength of a liner is less than the maximum allowable operating pressure of the pipeline, it is considered as Class II or Class III. The difference between Class II and Class III liners is the resistance to external buckling forces and dependence on liner/host pipe wall adhesion for structural stability.

- Class IV Liners: are fully structural liners with a long-term (50-year) internal burst strength, relative to the maximum allowable operating pressure (MAOP), equal to or greater than the host pipe. The liner should maintain structural integrity even if the host pipe fails; that is, the Class IV liner can be viewed as an equivalent, replacement pipe.

AWWA classifies CIPP systems into three main groups: felt-based systems, woven hose systems and membrane systems. Due to the composite structure of the hose and resin, woven hose systems can be designed to carry varying internal pressures and external loads. In this study, the woven hose system is examined (i.e. Figure 1.3). The woven polyester fiber hoses are impregnated with resin before they are pulled into the pipe. Then the resin is cured in field at a high temperature (usually hot water or steam).

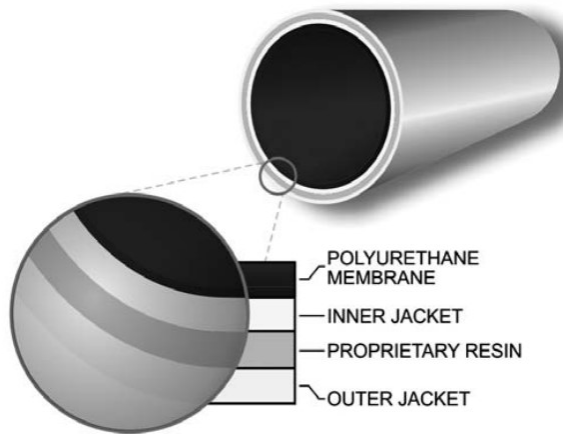


**Figure 1.3 Cross-section of woven hose (From AWWA)**

Brown et al., (2008) performed physical experiments on a cured-in-place polymer pipe liner to identify the constitutive characteristics of the composite pressure pipe liner. The composite liner consists of inner and outer jackets with polymeric resin injected within the two jackets. It should be capable of resisting the internal pressure without the host pipe. Tensile tests in both longitudinal and circumferential directions have been performed (i.e. Figure 1.4, 1.5, 1.6). The study concluded that the composite liner generally has a bilinear stress-strain behavior, with a curved transition zone followed by strain-hardening behavior. The initial modulus and ultimate tensile strength in the hoop direction are 45% higher than in the longitudinal direction.

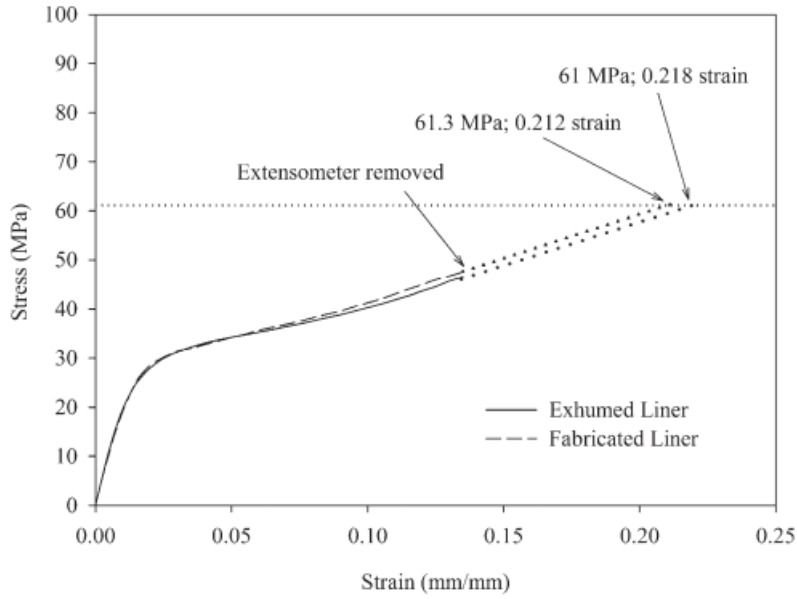


**Figure 1.4 Stress–strain curves for the exhumed and fabricated liners in the longitudinal direction (After Brown et al., 2008)**

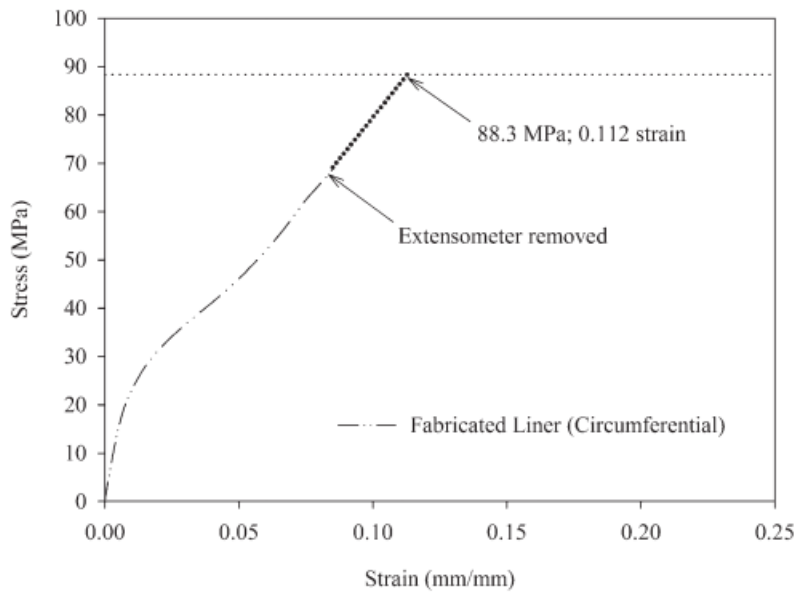


**Figure 1.5 Stress-strain curve for the fabricated liner in the circumferential direction (After Brown et al., 2008)**

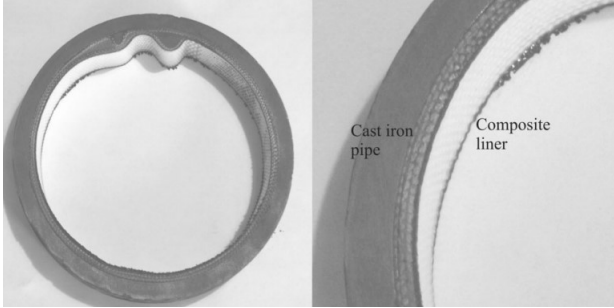


**Figure 1.6 Cross-section of exhumed cast iron pipe (After Brown et al., 2008)**

#### **1.4 Limitations: Six potential limit states**

Considering the effects of internal water pressure and nonuniform ground movements, Allouche et al., (2005) identified six potential limit states that can influence the stability of the liner during its service life. The six limit states are illustrated in Figure 1.7 and denoted as following:

- “...LS1: Simple hoop tension in the liner induced by internal fluid pressure in sections where the metal ‘host’ pipe has fractured longitudinally, Figure 1.7(a)
- LS2: Axial bending in the wall of the liner where the liner spans from a section of host pipe that has split, to one that is maintaining its integrity, Figure 1.7(b)
- LS3: Axial bending in the liner where it passes through a pipe section fitted with a ring clamp, Figure 1.7(c)
- LS4: Overall bending moment for the liner  $M_R$  or local bending moment  $M_L$  and stretching force  $T_L$  in the liner wall can occur across ring fractures or joints, Figure 1.7(d); rotation angle  $\alpha$  of one segment relative to the next results from differential ground movement due to frost or moisture changes in ‘reactive’ clays.

- LS5: Local bending where the liner spans across circular plugs formed by graphitization of cast iron, Figure 1.7(e);
- LS6: Local stresses associated with liner in the vicinity of a lateral connection, Figure 1.7(f)...”.

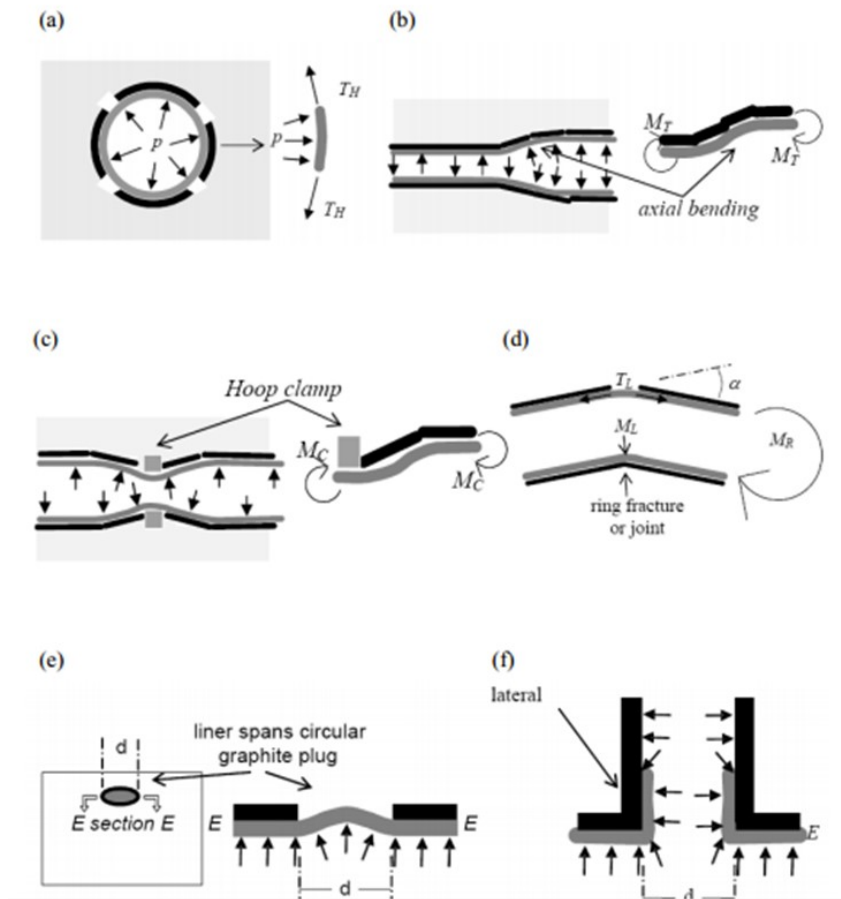


Figure 1.7 Six limit states (After Allouche et al., 2005)

### 1.5 Thesis Outline

The objective of the study is to analyze the mechanical performance of a pressure pipe CIPP liner with stress concentration effects due to local defects including circular voids, ring fracture and joint rotation. In particular, the limit states (d) and (e) as defined by Allouche et al., (2005), as shown in Figure 1.7, are of interest. A third loading case will

also be examined, for internal pressure load effects on the development of an axial gap in the host pipe due to (i) full circumferential deterioration and loss of contact, and (ii) axial gap discontinuity due to effects of adjacent relative ground motion.

In this study, continuum finite element modelling (FEM) procedures are used to examine the mechanical response and performance of the Class # CIPP liner for pressure pipe. The numerical modelling procedures are calibrated against available public domain literature. The finite element analysis is conducted with Abaqus/Standard v6.13. Three-dimensional brick (C3D8I) elements are used to model both the CIPP liner and the host pipe. Multiple layers of elements through liner's thickness are used depending on the CIPP liner diameter to wall thickness ( $D/t$ ) ratio. The liner elastic-plastic behaviour is modeled, while only elastic behaviour is considered for the host pipe due to the relative difference in pipe stiffness.

The liner mechanical response (i.e. state of stress or strain, deformation modes) is examined as a function of key design parameters including the diameter to wall thickness ratio ( $D/t$ ), relative pipe stiffness (host and liner), load effects (i.e. internal pressure, external moment) including the hoop stress due to internal pressure and yield stress ratio ( $\sigma_h/\sigma_y$ ), host pipe/CIPP liner interface friction coefficient ( $\mu$ ), and the deteriorated state (i.e. type, magnitude) such as void diameter to pipe diameter ratio ( $d/D$ ).

The second chapter examines the limit state for the liner section spanning across a circular void in the cast iron pipe (LS5) using continuum finite element modelling

procedures. A sensitivity analysis is conducted across a range of practical design parameters. The liner response is assessed with respect to axial, hoop and equivalent stress states, radial liner displacement and longitudinal profile response.

The third chapter investigates the limit state for the liner section spanning across a circumferential gap in the cast iron pipe using finite element modelling procedures. The liner response is assessed with respect to axial, hoop and equivalent stress states, radial liner displacement and longitudinal profile response.

The fourth chapter examines the limit state for the liner section spanning across a circumferential gap under rotational deformation. This scenario is corresponding to the liner/pipe system under differential ground movement. Numerical analysis is conducted under different lengths and boundary conditions. The liner response is assessed with respect to stress states, moment-curvature relationship, ovality rate of the liner and longitudinal profile response.

The last chapter summarizes the conclusions and results obtained from the analysis conducted in this study. The application of this research is discussed and potential subsequent study is recommended.

## **Chapter 2: Influence of Local Void Defect for Internal Pressure Loading**

### **2.1 Preface**

This chapter is based on a paper submitted to the 2019 American Society of Civil Engineers (ASCE) Utility Engineering & Surveying Institute (UESI) Pipelines Conference. The paper citation is:

He, X. and Kenny, S. (2019). "Mechanical performance of a pressure pipe CIPP liner with stress concentration effects associated with local defects." Submitted to ASCE UESI Pipelines Conference, 13p.

The current status of this manuscript is "in press".

The principal investigator was Xiaohan He where he was the primary responsible person to define the problem statement, establish the analysis matrix used in the parameter study, develop the numerical modelling procedures, conduct the numerical simulations, and report on the data synthesis, analysis and conclusions. Guidance, mentorship and editorial support was provided by the supervisor, Dr. Shawn Kenny, in the development of the conference manuscript.

## 2.2 Introduction

Components of our modern water distribution system, where in some municipalities may have been built in the later part of the 19<sup>th</sup> century, have experienced deterioration and, at times, failure through the pipe body or at pipe joints due to manufacturing defects (e.g. imperfections), transient loads (e.g. surge pressure), time dependent mechanisms (e.g. corrosion, embrittlement) and mechanical action (e.g. outside force, ground movement). Observed failure modes for these systems include pitting, splitting, cracking, circumferential breaks and joint rupture (Allouche et al., 2005; Brown et al., 2008; Makar et al., 2001; Paradkar, 2012). These systems are critical components of our core municipal assets that meet our daily functional needs and promote healthy living standards. For deteriorated water distribution systems, it is estimated that 10% to 30% of the total water supplied is lost during transport. Furthermore, contaminants may penetrate through these deteriorated pipelines and may affect public health and safety through degraded water quality (Seica et al., 2002).

Historically, the majority (greater than 90%) of pipe repair actions were performed using conventional open trench digs with pipe replacement (Brown et al., 2008; Jeyapalan, 2003). Modernization and rehabilitation of the existing water distribution network, using these conventional techniques with wholesale asset replacement, is not practical due to logistics, cost and public disruption (i.e. temporary loss of water service and road access). Over the past 20 years, the development of lining and trenchless technologies has provided a more practical, robust, more cost effective and less invasive approach for the

rehabilitation of damaged pipe in comparison with conventional open trench practices. Some of these techniques include (AWWA, 2014):

- Spray-on Polymer Lining: Polymeric materials are sprayed on the inner surface of the old pipe to form a liner that eliminates pipeline internal corrosion,
- Slip Lining: A new pipe is pulled inside the existing pipeline,
- Pipe Bursting: A new pipe is pulled into the space created by breaking up the existing pipeline, and
- Cured-in-Place Pipe (CIPP): A new pipe is formed within the host pipeline.

These techniques can be used in non-structural (Class I) applications (e.g. spray lining) whereas others (e.g. thin walled polyethylene liners) may be used in semi-structural (Class II/III) applications (AWWA, 2014). There are practical constraints and limitations such as blocking lateral service connections and mechanical design performance when subject to operational loads without composite action from the original cast iron pipe.

The CIPP technique was developed in the 1970's and successfully applied for the rehabilitation of a sewer pipe in the London Borough of Hackney (Bueno, 2011). Since that time, a body of research and practical industrial experience on the use of CIPP with gravity flow pipe (e.g. sewer lines) has been developed. For gravity flow pipelines, CIPP can extend rehabilitation and improve asset performance and extend the service life through a cost effective and minimally invasive technique. There are three broad

classification of CIPP systems that include felt, woven hose and membrane systems (AWWA, 2014).

For pressure pipe, CIPP systems are reinforced felt/glass liners or composite layers with epoxy resins that have minimum initial tensile yield strengths of 21 MPa for polyester and 28 MPa for vinyl ester systems (ASTM F1216, 2016; ASTM F1743, 2017). In comparison with CIPP systems for gravity pipe, there are relatively few studies on CIPP applications for pressure pipe where the application of this technology is the subject of continued research and development (Brown et al., 2008). One of the constraints for CIPP systems in pressure pipe applications is the limitation on manufactured bends to 45°.

Allouche et al., (2005) identified six possible limit states that could affect the liner performance, stability and integrity including

- LS1 Hoop Tension: liner section through host pipe segment that does not provide pressure containment resistance
- LS2 Axial Stress: liner section transitioning between host pipe segments with and without pressure containment resistance
- LS3 Axial Stress: liner section through a host pipe segment with a ring clamp
- LS4 Axial Stress and Rotation: liner section spanning a host pipe segment with a local ring fracture or pipe joint with relative rotation
- LS5 Local Stress: liner section spanning across a void

- LS6 Local Stress: liner section transitioning through an open lateral connection

In collaboration with the City of Hamilton, the researchers conducted a case study for a CIPP liner rehabilitation project on a potable water distribution system. A 75 year old, 150 mm diameter cast iron water main was lined with Aqua Pipe™. Following installation, 12 rehabilitated pipe segments (1.5 m length) were removed for post-installation assessment. The laboratory tests included uniaxial tension tests (i.e. direct longitudinal properties), parallel plate loading (i.e. inferred circumferential properties), 7 burst tests and one long-term pressure test. The initial (short term) elastic modulus was 2.0 GPa with yield strength of approximately 25 MPa, yield strain of 1.3% and tangent modulus of 180 MPa. Continuum finite element analysis was conducted to assess three limit states including LS2, LS3 and LS5. For voids in the cast iron pipe with a radius greater than 30 mm ( $>0.4D$ ), the tensile bending stress exceeded the unconfined hoop tension stress by 30%. For a void of 40 mm radius ( $0.533D$ ), the numerical simulations predicted tensile bending stresses more than twice the unconfined hoop tension stress (Allouche et al., 2005). The finite element analysis (FEA) indicated the presence of longitudinal folds on significantly reducing the liner pressure rating.

Through a series of laboratory tests, Brown et al., (2008) compared the uniaxial tension stress-strain behaviour of fabrication liner coupons with the in-situ liner material recovered during the studies conducted by Allouche et al., (2005). The observed behaviour for the coupons, regardless of origin, was identical with a nonlinear

(approximately bilinear) response. The initial longitudinal elastic modulus was 2.0 GPa, which was governed by the resin, yield strain of 1% and yield strength of 23.5 MPa (0.2% offset) and ultimate strength of 61 MPa. The liner material exhibited orthotropic material behaviour with an initial circumferential elastic modulus of 3.0 GPa, yield strain of 0.9%, yield strength of 24 MPa (0.2% offset) and ultimate strength of 88.4 MPa. The post-yield tangent modulus in the circumferential direction was greater than the longitudinal direction by a factor of 3.5, which indicates a stiffer post-yield response. Physical modelling and numerical simulation studies on the local buckling response of high strength steel pipe suggest the anisotropic behaviour of the CIPP liner may trigger bifurcation mechanisms in the longitudinal direction through interaction between the axial and circumferential mode response when subject to combined loads of internal pressure and bending (e.g. Fatemi and Kenny, 2017; Kenny et al., 2016).

Brown et al., (2014) used continuum FEA to examine the performance of the CIPP liner for LS3, as defined by Allouche et al., (2005). The numerical simulations observed no significant differences in the hoop or axial bending stress, for the 700 kPa maximum surge reference pressure, when using 3D continuum (Brown et al., 2014) or axisymmetric (Allouche et al., 2005) modelling approaches. The FEA indicated the effects of interface friction were not significant for this limit state and the initial (short term) circumferential material properties could be used to predict the burst pressure. The study recommended an assessment of strength reduction due to creep on the burst limit state.

In this study, the limit state for the liner section spanning across a void in the cast iron pipe (LS5) is examined using continuum finite element modelling procedures. The numerical modelling procedures are calibrated using available public domain data. A sensitivity analysis is conducted across a range of practical design parameters including for both limit state scenarios. The liner response is assessed with respect to axial, hoop and equivalent stress states, radial liner displacement and longitudinal profile response.

## 2.3 Finite element modelling procedures

### 2.3.1 Pipe Geometry, Modelling Considerations and Boundary Conditions

The primary structural configuration, examined in this study, is a cast iron pipe with a local void, which may be due to pitting corrosion or other defect, and CIPP liner subject to internal pressure (Figure 2.1). The CIPP liner pipe has an outer diameter,  $D$ , liner wall thickness,  $t$ , external cast iron pipe wall thickness,  $t_p$ , and circular void diameter,  $d$ . The liner is subject to a uniform internal pressure.

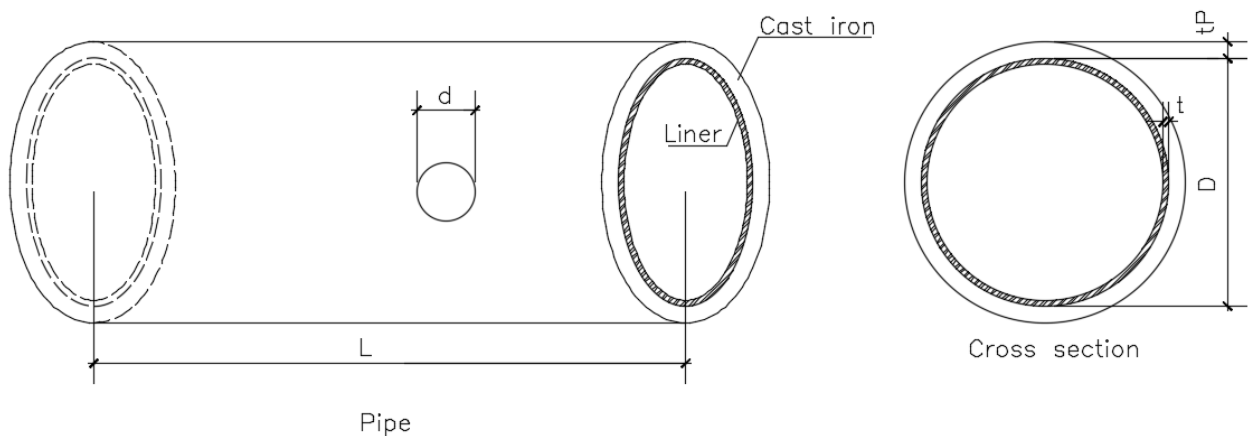


**Figure 2.1 Principal geometric parameters for the CIPP liner and cast iron pipe with void defect**

The three-dimensional (3D) continuum finite element analysis was conducted using the software program Abaqus v6.13. To reduce the computational expense, a one-quarter

pipe model was used in analysis with the symmetric planes defined at the void center along the longitudinal and circumferential pipe directions (Figure 2.2).

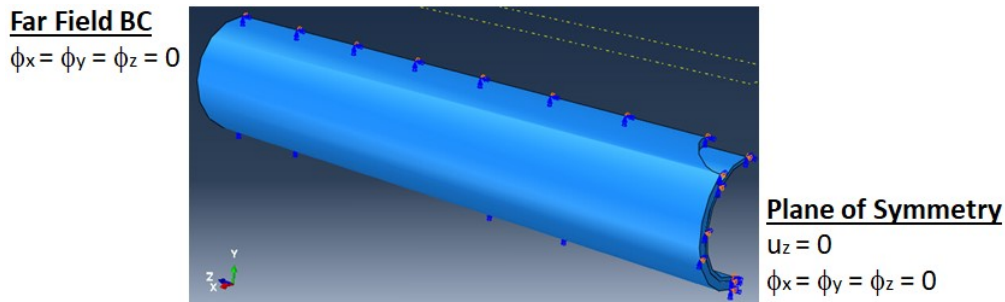


**Figure 2.2 One-quarter model of CIPP liner and cast iron pipe**

The CIPP liner and host pipe were modelled using the 3D, 8-node general purpose continuum element (C3D8I-8), which is a lower-order quadrilateral element enhanced by incompatible modes to improve bending behaviour. Incompatible deformation modes are used to mitigate ‘shear locking’ effects, which can be observed in fully integrated first-order isoparametric elements, and artificial stiffening due to Poisson's effect when subject to bending. For the deformation modes examined in the study, these mechanisms are not of direct significance but the response will provide a baseline for future studies examining the effects of flexural loading. The C3D8I element has three translational degrees of freedom per node.

The pipe boundary conditions were defined at reference points (RP#) located at far field end of the pipe on the longitudinal axis that was coincidental with the centroid of the vertical cross-section. The RP coupled nodal degrees of freedom (DOFs) for the

continuum elements discretizing the CIPP liner and cast iron pipe. The pipe centreline boundary condition was defined using symmetric boundary conditions and RP2 was defined as an ideal roller connection. RP2 was longitudinally unconstrained while other degrees of freedom were constrained. In the radial direction, the pipe was unconstrained and allowed to freely expand when subject to internal pressure with plane sections remaining plane during the analysis. These kinematic constraints were defined by the DOFs coupling.

### 2.3.2 Numerical Procedures

The finite element analysis was conducted using nonlinear procedures using Newton-Raphson iterations to account for large deformations and plastic material behaviour in the CIPP liner, and interface contact between the CIPP liner and host pipe.

The cast iron pipe material properties were defined as an elastic modulus of 120 GPa with a Poisson ratio of 0.3. In the numerical simulations, the mechanical deformation response of the cast iron pipe remained in the linear elastic range.

**Table 2.1 Orthotropic elastic material properties**

Elastic Modulus			Poisson's Ratio			Shear Modulus		
$E_{11}$	$E_{22}$	$E_{33}$	$\nu_{12}$	$\nu_{13}$	$\nu_{23}$	$G_{12}$	$G_{13}$	$G_{23}$
(GPa)	(GPa)	(GPa)	(#)	(#)	(#)	(GPa)	(GPa)	(GPa)
2.0	3.0	2.0	0.3	0.3	0.3	1.0	1.0	1.5

The CIPP liner elastic constitutive behaviour was modelled using orthotropic material parameters, which must be consistent with the material orientation in the local coordinate

system. Based on the study by Brown et al., (2014), the material properties, assigned for each material direction, are summarized in Table 2.1 for the elastic modulus ( $E$ ), Poisson's ratio ( $\nu$ ) and shear modulus ( $G$ ).

The nominal (engineering) stress-strain data, determined from laboratory tests, was modified into true stress-strain relationships (Figure 2.3). The plastic material response was defined using the Hill potential function. The anisotropic stress-strain relationships for the CIPP liner, in the longitudinal and circumferential directions, were based on the data provided by Brown et al., (2008). The Hill potential function relates the anisotropic behaviour through a stress ratio parameter with the datum defined by the reference stress parameter. In this study, the reference stress-strain curve was the circumferential material behaviour with a stress ratio of 0.94, which is relative to the longitudinal stress-strain material behaviour. As shown in Figure 2.4, this approximation is reasonably accurate for true strain magnitudes less than 0.01, which is greater than the predicted liner strain for this study. As discussed by Fatemi and Kenny (2017), depending on the nature of the anisotropic behaviour then the Hill potential function could be utilized for larger strain magnitudes associate with local buckling of high strength steel pipelines subject to internal pressure and bending loads.

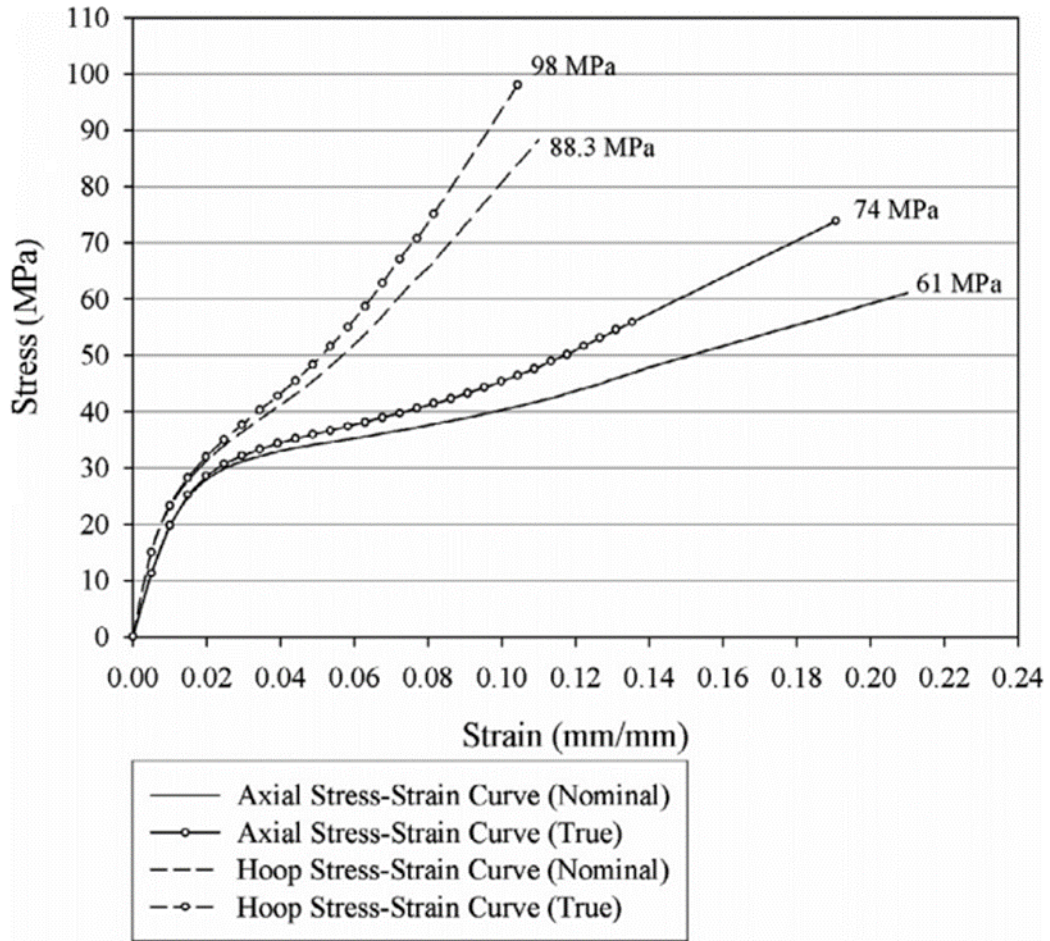


Figure 2.3 Stress-strain curves (After Brown et al., 2008)

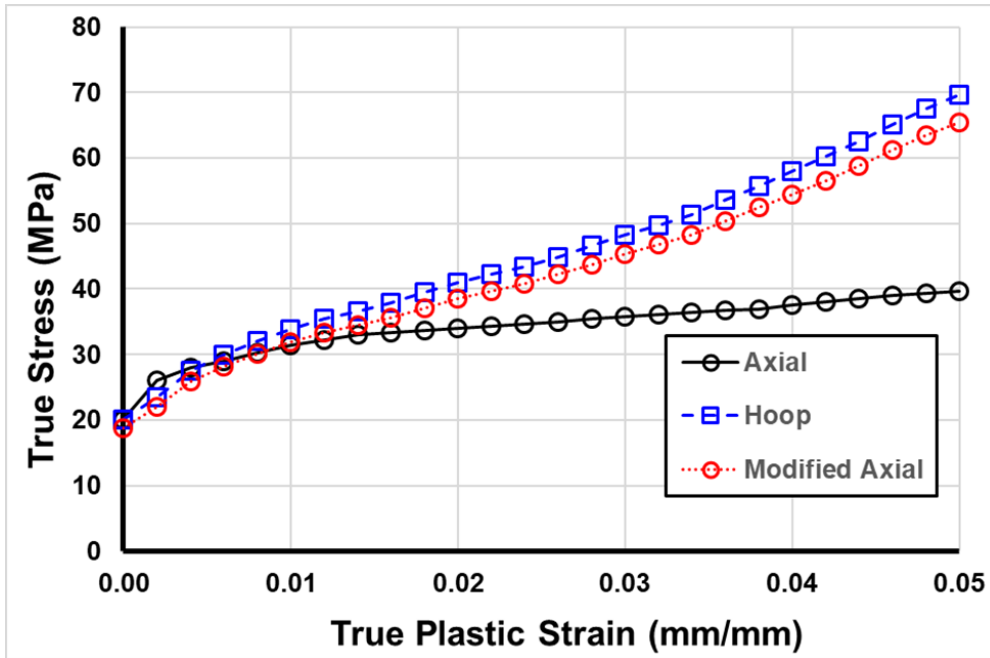


Figure 2.4 Anisotropic material properties based on Hill potential function

The CIPP liner/host pipe interface contact pressure, shear stress and slip potential introduces nonlinear behaviour, even for elastic material response, that was defined through surface contact pairs. Based on relative stiffness, the host pipe was the master surface and CIPP liner was the slave surface. The interaction was modelled using a finite sliding surface-to-surface discretization method with frictionless or frictional interface contact depending on the defined interface friction coefficient. The interface shear stress was modelled using the Coulomb friction mode and defined as a fraction of the contact pressure based on the interface coefficient of friction and normal contact pressure. In this study, the interface friction coefficient was defined as sliding or non-bonded ( $\mu = 0$ ) and sticking or fully bonded ( $\mu = 1$ ), which are the lower and upper bounds, respectively. A critical interface shear stress ( $\tau_{crit}$ ) can be defined where if the shear stress across the

interface is less than the critical shear stress, then no relative slip (i.e. motion) occurs between the paired contact surfaces.

## 2.4 Parameter study

### 2.4.1 Overview

In this study, four key parameters that influence the CIPP liner mechanical behaviour are assessed including the CIPP liner outside diameter to CIPP wall thickness ratio ( $D/t$ ), host pipe void diameter to host pipe inside diameter ratio ( $d/D$ ), hoop stress due to internal pressure to yield stress ratio for the CIPP liner ( $\sigma_h/\sigma_y$ ), and CIPP liner/host pipe interface friction coefficient ( $\mu$ ). The study parameter range is summarized in Table 2.2.

**Table 2.2 Parameter range assessed in this study**

Parameter		Range
Term	Symbol	
Dimension ratio	$DR$	40, 60 & 80
Void ratio	$d/D$	0.2, 0.4, 0.6 & 0.8
Hoop stress ratio	$\sigma_h/\sigma_y$	0.2, 0.4, 0.6 & 0.8
Friction coefficient	$\mu$	0,1

The *DR* ratio is a key non-dimensional geometric parameter influencing the pipe mechanical performance when subject to internal pressure and external loads (e.g. Fatemi and Kenny, 2017; Kyriakides et al., 2007; Timoshenko and Gere, 1961). The CIPP liner yield strength of 20 MPa was based on the study by Brown et al., (2008) with the hoop stress to yield ratios ( $\sigma_h/\sigma_y$ ) selected across a range of design parameters for the sensitivity analysis.

For partially deteriorated pressure pipe, ASTM F1216 (2016) defines limits on the void damage  $d/D$  ratio where the CIPP liner can be considered a fixed flat plate subject to transverse pressure load, as stated in Eq 2.1.

$$\frac{d}{D} \leq 1.83 \left(\frac{t}{D}\right)^{0.5} \quad \text{Equation 2.1}$$

For the  $D/t$  ratio investigated in this study, of 40, 60 and 80 as summarized in Table 2.2, based on Eq 2.1, the corresponding  $d/D$  limits are 0.29, 0.24 and 0.20, respectively. Otherwise the CIPP liner is considered to be in a state of ring tension (i.e. governed by hoop stress).

The CIPP liner/host pipe friction interface represented the bounding limits of fully bonded ( $\mu = 1$ ) and non-bonded ( $\mu = 0$ ) interface.

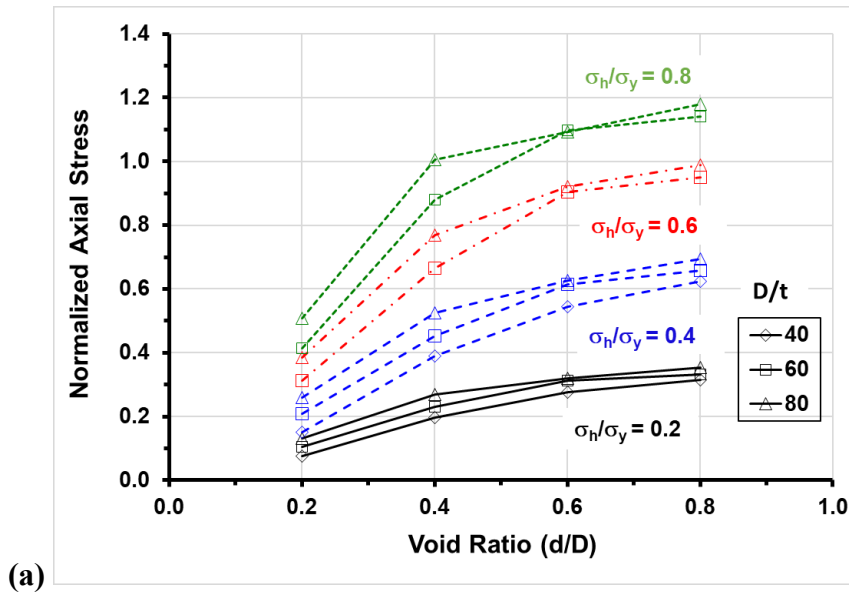
## **2.5 Finite element predictions – influence of void defects**

### **2.5.1 Variation in Liner Dimension ( $D/t$ ), Hoop Stress ( $\sigma_h/\sigma_y$ ) and Void Defect ( $d/D$ ) Ratios**

The predicted normalized axial, hoop and equivalent (von Mises) stress states for a variation in the liner dimension ( $D/t$ ), hoop to yield stress ( $\sigma_h/\sigma_y$ ) and void defect ( $d/D$ ) ratios are shown in Figure 2.5 for the non-bonded liner interface ( $\mu = 0$ ). The liner diameter was 155 mm based on the studies by Brown et al., (2014, 2008), which were the basis for calibrating the numerical modelling procedures used in this study. The stress magnitudes were normalized with respect to the longitudinal tensile yield strength ( $\sigma_{yL}$ )

for the axial stress and circumferential or hoop tensile yield strength ( $\sigma_{yH}$ ) for the hoop and equivalent (von Mises) stress response.

As a general observation, the normalized axial, hoop and equivalent stress response proportionally increased with changes to the liner dimension ( $D/t$ ) and hoop stress to yield ( $\sigma_h/\sigma_y$ ) ratio. The stress values shown in the figures are average nodal stresses. This behaviour is consistent with the response of simple cylinders, without defects, subject to internal pressure. For the lower void ( $d/D \leq 0.4$ ) and hoop stress ( $\sigma_h/\sigma_y \leq 0.4$ ) ratios, the predicted CIPP liner response (Figure 2.5) is generally consistent with Eq 2.1 and highlights the inherent conservative approach, which has an upper bound of 0.29 for the parameters investigated in this study.



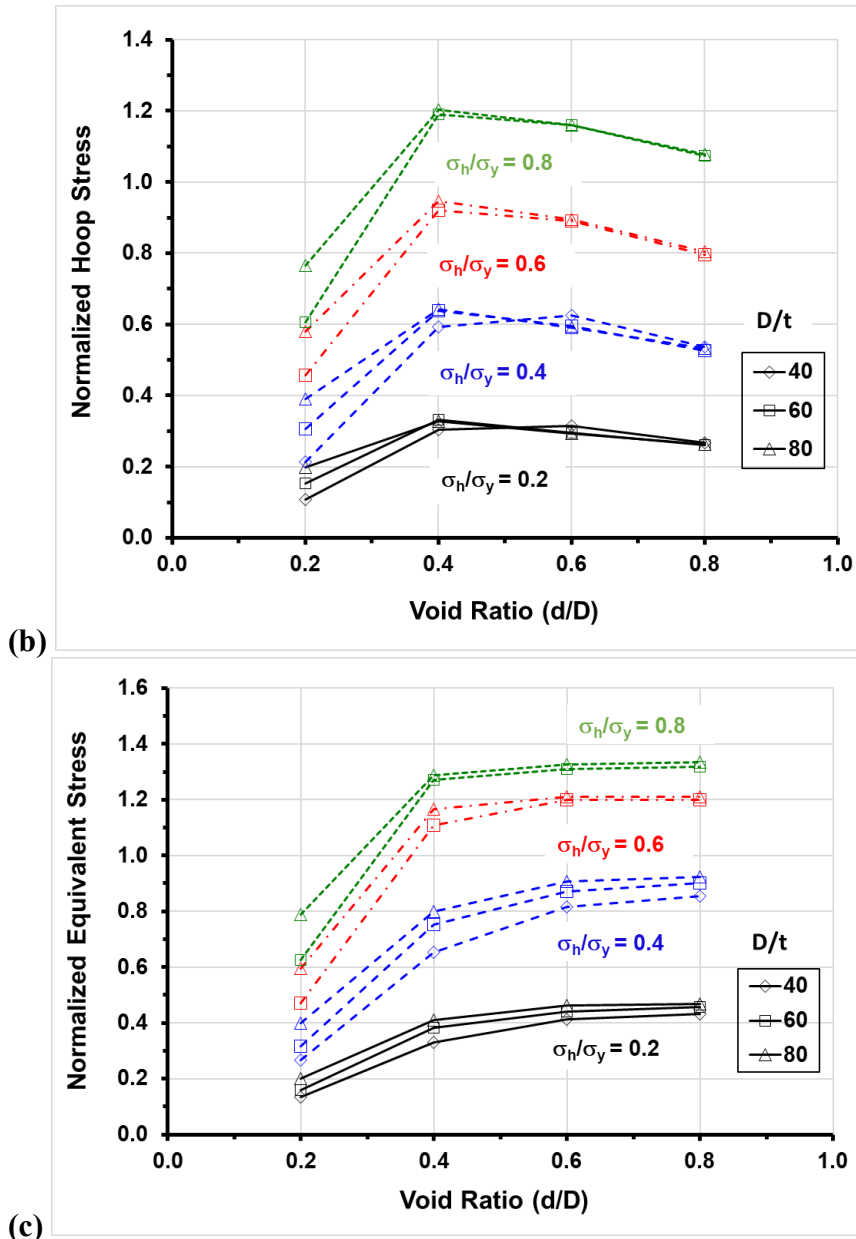


Figure 2.5 Normalized (a) axial, (b) hoop and (c) equivalent stress response with void ratio ( $d/D$ ) across a range of liner dimension ( $D/t$ ) and hoop stress to yield ( $\sigma_h/\sigma_y$ ) ratios for an un-bonded CIPP liner/host pipe interface ( $\mu = 0$ )

These observations (Figure 2.5) are consistent with the general findings of Allouche et al., (2005) where continuum FEA was conducted to assess LS5 for a 150 mm diameter pipe with circular perforations of 10 mm, 20 mm, 30 mm and 40 mm (i.e.  $d/D = 0.10, 0.13,$

0.20 & 0.27). For a perforation of 30 mm ( $d/D = 0.20$ ), the tensile bending stress exceeded the hoop tension stress by 30%. The study concludes: "...Liner use where perforations of 30 mm or greater (i.e.  $d/D \geq 0.20$ ) are expected will likely reduce time to failure relative to those obtained from testing of unconfined liner under internal pressure...".

In this study, the normalized hoop stress was observed to be a local maximum, across the range of liner dimension ( $D/t$ ) and hoop stress to yield ( $\sigma_h/\sigma_y$ ) ratios examined, at a void ratio ( $d/D$ ) of 0.4, which is consistent with the findings by Allouche et al., (2005). The hoop stress response tends to decrease towards the applied loading condition (i.e. hoop to yield stress ratio,  $\sigma_h/\sigma_y$ ) and behave as an unconstrained liner in the radial direction (Figure 2.5b). For the lower stress ratios ( $\sigma_h/\sigma_y \leq 0.4$ ), the liner response remained elastic across the parameter range for the liner dimension ( $D/t$ ) and void defect ( $d/D$ ) ratios (Figure 2.5b,c). At higher stress ratios ( $\sigma_h/\sigma_y \geq 0.6$ ), the liner response was elastic across the liner dimension ( $D/t$ ) parameters range for the lowest void defect ( $d/D = 0.2$ ) ratio. Transition to plastic material behaviour for the CIPP liner occurs with a void defect ( $d/D$ ) of approximately 0.3. An analysis case with the full yield condition due to internal pressure (i.e.  $\sigma_h/\sigma_y = 1.0$ ) was also examined, with no significant differences for the plastic response being observed.

However, in this study, for larger void ( $d/D \geq 0.4$ ) and hoop stress ( $\sigma_h/\sigma_y \geq 0.6$ ) ratios, plastic material behaviour (i.e. normalized stress > 1) for the axial and equivalent stress response was observed (Figure 2.5a,c). This suggests the CIPP liner limit state may not

only be governed by ring tension (i.e. internal pressure effects as shown in Figure 2.5b), which was discussed by Allouche et al., (2005), but governed by local plastic behaviour dependent upon the void ( $d/D$ ) and hoop stress ( $\sigma_h/\sigma_y$ ) ratios. The maximum normalized axial (Figure 2.5a) and equivalent stress (Figure 2.5c) response continued to increase with void ratio ( $d/D$ ), whereas the hoop stress (Figure 2.5b) decreased in magnitude for each hoop stress ratio ( $\sigma_h/\sigma_y$ ) examined. Consequently, the equivalent stress exhibited a plateau or limiting response for higher void ratios ( $d/D > 0.6$ ) for both elastic and plastic material behaviour.

As the void ratio ( $d/D$ ) increases, the axial stress increases due to a local flexural response (i.e. curvature change) of the CIPP liner through interaction with the host pipe and deflection through the void space. This is supported through observations on the radial displacement of the CIPP liner, as shown in Figure 2.6, where the relationship between the normalized radial displacement of the CIPP liner with the normalized axial distance measured from the void center along the pipe longitudinal axis (i.e. length) is presented. The radial displacement, which is measured in the CIPP liner at the center of the void, is normalized with respect to the theoretical radial displacement (0.4 mm) of an unconstrained CIPP liner pipe subject to internal pressure. The normalized axial distance is the distance measured along the pipe axis, starting from the void center, with respect to the CIPP liner diameter. For the data presented in Figure 2.6, the analysis parameters included a CIPP liner diameter of 155 mm,  $D/t$  ratio of 60, hoop stress ( $\sigma_h/\sigma_y$ ) ratio of 0.8 with an un-bonded interface ( $\mu = 0$ ) condition.

As shown in Figure 2.6, the normalized radial displacement profile exhibited a non-linear, sinusoidal pattern with distance from the void center that tended toward zero amplitude due to the host pipe radial constraint. Effect of the void defect edge or shoulder on the liner radial displacement can be observed at normalized distance of 0.1, 0.2, 0.3 and 0.4, which corresponds to void ( $d/D$ ) ratios of 0.2, 0.4, 0.6 and 0.8, respectively. The maximum normalized radial displacement amplitude occurs at the void center (i.e. normalized distance = 0), which develops a distinct plateau (i.e. limiting amplitude) for higher the void ratios ( $d/D \geq 0.6$ ). The plateau response is related to the biaxial (principal) stress interaction (i.e. axial, hoop stress) with increasing void ratio ( $d/D$ ) and plastic material behaviour for the equivalent stress response (Figure 2.5c). Interaction effects between the host pipe void and local relative stiffness (i.e. void edge or shoulder) were also observed. For higher void ratios ( $d/D \geq 0.4$ ), the negative normalized radial displacement magnitudes are due to changes in local curvature within the CIPP liner in response to the applied internal pressure with changes in the local relative stiffness, between the void space and intact host pipe, and resultant lateral deflection through the void. The amplitude and wavelength of the negative radial deflection, adjacent to the void shoulder, increases with increasing void ratio ( $d/D$ ).

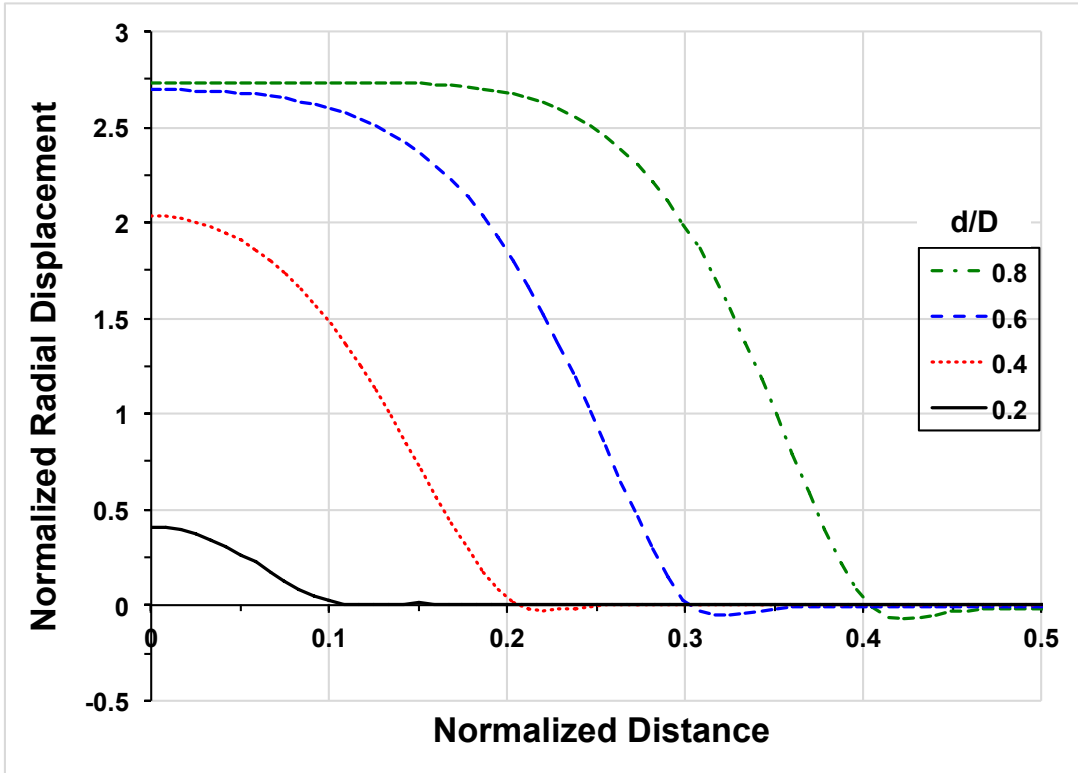


Figure 2.6 Normalized radial displacement of the CIPP liner as a function of the normalized distance from the void center along the pipe length

As shown in Figure 2.5, these interaction effects appear to have greater significance, for a specific void ( $d/D = 0.6$ ) and liner dimension ( $D/t = 60$ ) ratio, that may have influenced the numerical predictions. For these specific analysis cases, the data exhibits slight deviation from the global general trend observed in the parameter study. This may be attributed to the relationship among relative stiffness effects on the pipe deformation mode response including circumferential (i.e. pipe ring) and axial (i.e. bending stress and deformations through the void) material and mechanical behaviour of the CIPP liner, discretization (i.e. number and type of elements) effects, and edge constraint from the void and relatively stiff host pipe.

Correspondence between the maximum stress amplitude, stress state and location was also examined (Figure 2.7, Table 2.3). The liner one-quarter section (Figure 2.7), bounded by the axial (i.e. longitudinal, horizontal) pipe direction and hoop (i.e. vertical) direction, was subdivided into 4 clock positions (6, 7, 8 & 9) or radial sectors. The FE results were analysed to extract the location of the maximum stress amplitude for the hoop (i.e. circumferential), axial (i.e. longitudinal) and equivalent (i.e. von Mises) stress states across the range of void ratios ( $d/D$ ) examined. The results are summarized in Table 2.3 across a range of void ratios ( $d/D$ ) with the locations (Notation: c – void center; # - clock position on void perimeter; o - outer liner surface; i - inner liner surface). For lower void ratio ( $d/D = 0.2$ ), the maximum hoop and axial stress occurred at the void center on the outer liner surface. As the void ratio increased, in response to the local constraints, relative stiffness and natural deformation modes of the CIPP liner, then the maximum hoop stress moved towards the 6 clock position (i.e. void edge in the circumferential direction), the maximum axial stress moved towards the 9 clock position (i.e. void edge in the longitudinal direction) and the maximum equivalent stress moved towards the 8 clock position due to the biaxial stress interaction (Figure 2.5). For these cases, the maximum stress was located in the inner liner surface.

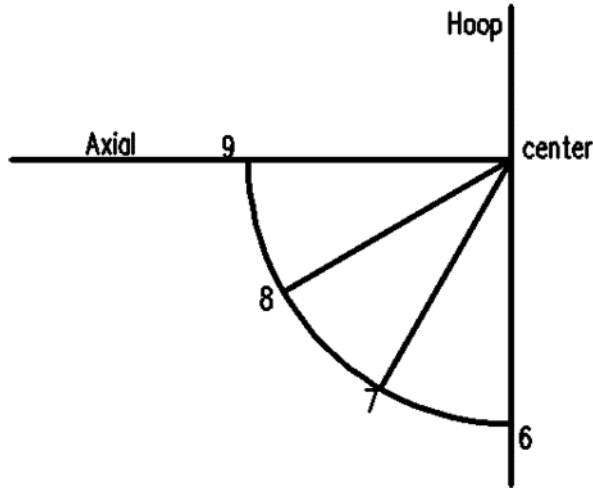


Figure 2.7 Location diagram

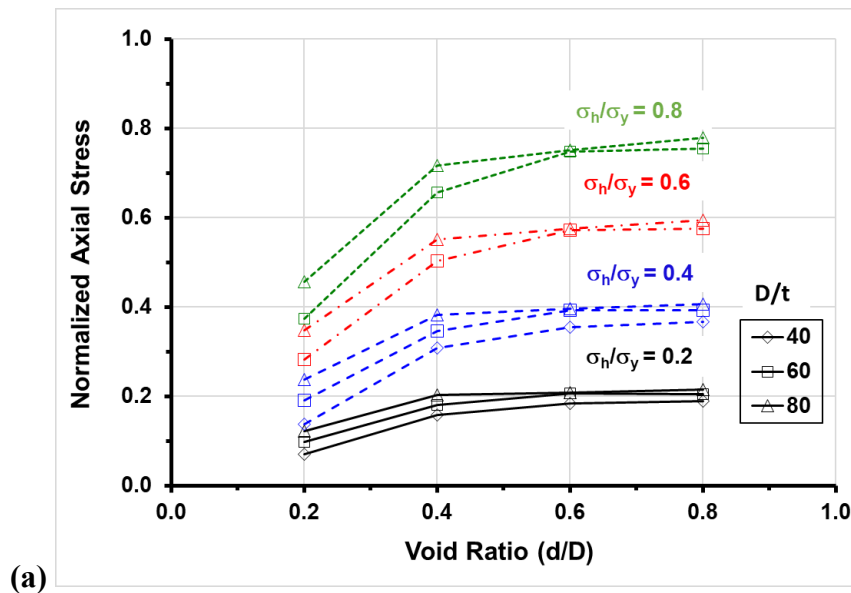
Table 2.3 Radial and through thickness location for maximum stress

$d/D$	Hoop Stress	Axial Stress	Equivalent Stress
0.2	co	co	7.5i
0.4	6.5i	8.5i	7.5i
0.6	6.5i	9i	8i
0.8	6i	8.5i	8i

### 2.5.2 Variation in the CIPP Liner/Host Pipe Interface Friction Coefficient ( $\mu$ )

The influence of a fully bonded CIPP liner pipe/host pipe interface (i.e.  $\mu = 1$ ) on the predicted stress response was also investigated across the same parameter range for the variation in the liner dimension ( $D/t$ ), hoop stress to yield ( $\sigma_h/\sigma_y$ ) and void defect ( $d/D$ ) ratios. There was consistent behaviour for the normalized hoop and equivalent stress response (Figure 2.8b,c) with the results for the un-bonded interface ( $\mu = 0$ ) simulations (Figure 2.5b,c) across the parameter range for the liner dimension ( $D/t$ ) and hoop stress to yield ( $\sigma_h/\sigma_y$ ) ratios.

One of the significant differences in the predicted response was the normalized axial stress remained in the elastic range with the tendency to exhibit plateau response for higher void ratios ( $d/D > 0.4$ ). Plastic behaviour was only observed for the highest hoop to yield stress ( $\sigma_h/\sigma_y = 0.8$ ) and larger void defect ( $d/D > 0.4$ ) ratios. For the fully bonded interface, the axial stress decreased by 30%, proportional with Poisson effect, and the von Mises stress decreased by 20% for the lower hoop stress to yield ( $\sigma_h/\sigma_y = 0.2$ ) and higher void ( $d/D = 0.8$ ) ratios. This difference was attributed to the virtual anchor or lock-in effects associated with the fully bonded interface, which constrains the CIPP liner deformation modes away from the void. Thus, the numerical simulations illustrate upper bound ( $\mu = 0$ ) and lower bound ( $\mu = 1$ ) response based on the CIPP liner/host pipe interface condition.



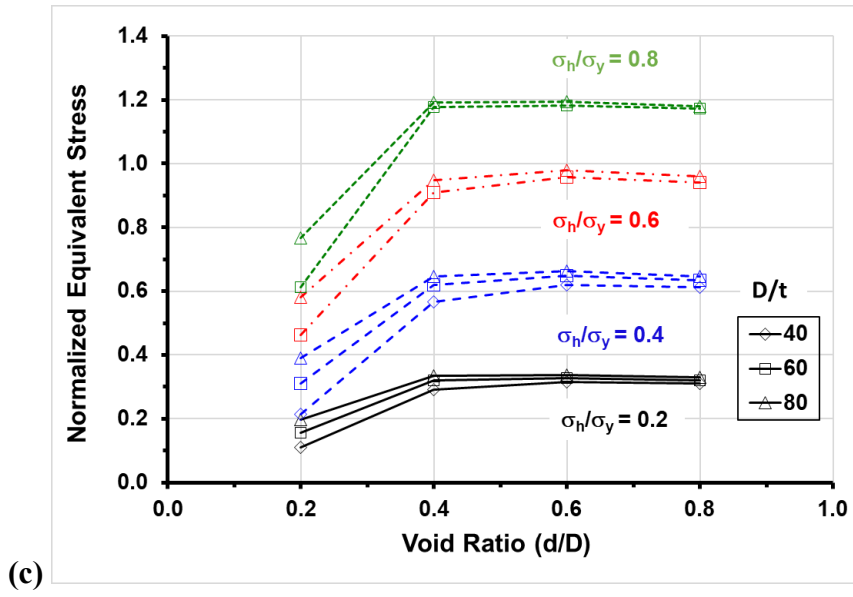
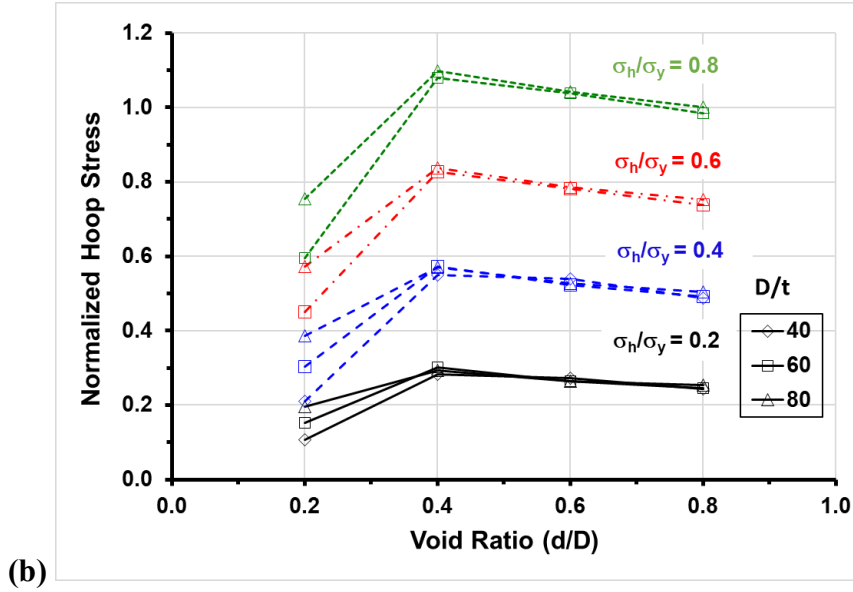


Figure 2.8 Normalized (a) axial, (b) hoop and (c) equivalent stress response with void ratio ( $d/D$ ) across a range of liner dimension ( $D/t$ ) and hoop stress to yield ( $\sigma_h/\sigma_y$ ) ratios for a fully bonded CIPP liner/host pipe interface ( $\mu = 1$ )

## 2.6 Conclusions

In the non-bonded cases, the normalized axial, hoop and equivalent stress response increased with increasing liner dimension ( $D/t$ ) and hoop stress to yield ( $\sigma_h/\sigma_y$ ) as expected. The equivalent stress yield behaviour was observed for the higher liner dimension ( $D/t > 60$ ) and hoop stress to yield ratios ( $\sigma_h/\sigma_y \geq 0.6$ ). The normalized hoop stress was observed to be a local maximum, across the range of liner dimension ( $D/t$ ) and hoop stress to yield ( $\sigma_h/\sigma_y$ ) ratios examined, at a void ratio ( $d/D$ ) of 0.4. In ASTM F1216 (2016), when the void ratio satisfies the limit of Eq 2.1, then the CIPP limit is governed by hoop stress. Based on this study, for larger void ( $d/D \geq 0.4$ ) and hoop stress ( $\sigma_h/\sigma_y \geq 0.6$ ) ratios, the von Mises yield stress may govern (Figure 2.8). This study has shown that the limit state may not be governed by ring tension with void ratios greater than 0.4. The maximum normalized axial and equivalent stress response continued to increase with the void ratio ( $d/D$ ), whereas the hoop stress decreases in magnitude. As the void ratio ( $d/D$ ) increases, the hoop stress tends to decrease towards the imposed hoop to yield stress ratio ( $\sigma_h/\sigma_y$ ) and behave as an unconstrained liner in the radial direction. This can also be observed from the radial displacement of the liner.

In terms of the effect of internal pressure, for the lower stress ratios ( $\sigma_h/\sigma_y \leq 0.4$ ), the liner response remained elastic across the parameter range for the liner dimension ( $D/t$ ) and void defect ( $d/D$ ) ratios. At higher stress ratios ( $\sigma_h/\sigma_y \geq 0.6$ ), the liner response was elastic across the liner dimension ( $D/t$ ) parameters range for the lowest void defect ( $d/D = 0.2$ ) ratio. Transition to plastic material behaviour occurs with a void defect ( $d/D$ ) of approximately 0.3.

For the fully bonded interface, differences were demonstrated due to the virtual anchor or lock-in effects. The normalized axial stress remained in the elastic range with the tendency to exhibit plateau response for higher void ratios ( $d/D > 0.4$ ). Plastic behaviour was only observed for the highest hoop to yield stress ( $\sigma_h/\sigma_y = 0.8$ ) and larger void defect ( $d/D > 0.4$ ) ratios. The axial stress decreased by 30%, and the effective stress decreased by 20% for the lower hoop stress to yield ( $\sigma_h/\sigma_y = 0.2$ ) and higher void ( $d/D = 0.8$ ) ratios.

## **Chapter 3: Influence of Local Gap Defect for Internal Pressure Loading**

### **3.1 Preface**

This chapter is prepared in the manuscript format. The current status of this manuscript is “prepared for submission” where the publication venue has yet to be identified. The principal investigator was Xiaohan He where he was the primary responsible person to define the problem statement, establish the analysis matrix used in the parameter study, develop the numerical modelling procedures, conduct the numerical simulations, and report on the data synthesis, analysis and conclusions. Guidance, mentorship and editorial support was provided by the supervisor, Dr. Shawn Kenny, in the development of the conference manuscript.

### **3.2 Introduction**

Components of our modern water distribution system, where in some municipalities may have been built in the later part of the 19th century, have experienced deterioration and, at times, failure through the pipe body or at pipe joints due to manufacturing defects (e.g. imperfections), transient loads (e.g. surge pressure), time dependent mechanisms (e.g. corrosion, embrittlement) and mechanical action (e.g. outside force, ground movement). Observed failure modes for these systems include pitting, splitting, cracking, circumferential breaks and joint rupture (Allouche et al., 2005; Brown et al., 2008; Makar et al., 2001; Paradkar, 2012). These systems are critical components of our core municipal assets that meet our daily functional needs and promote healthy living

standards. For deteriorated water distribution systems, it is estimated that 10% to 30% of the total water supplied is lost during transport. Furthermore, contaminants may penetrate through these deteriorated pipelines and may affect public health and safety through degraded water quality (Seica et al., 2002).

Circumferential cracking is one of the four failure modes reported by Makar et al., (2001). The author claimed that bending forces are usually the reason leading to this type of pipe failure. Once the circumferential crack develops, it proceeds across the circumference of the pipe (Figure 3.1). Rajani et al., (1996) also discussed the reasons behind this type of failure. Circumferential break is due to longitudinal tensile stresses. Several probable mechanisms can induce longitudinal tensile stresses into the water mains that includes:

- (1) Differential temperature: If the operational temperature of the pipe is different from the temperature during installation and back-fill, then the pipe will contract or expand relative to the initial configuration. Longitudinal tensile stress may develop when external soil restraint forces, developed at the pipe/soil interface, counteract pipe contraction.
- (2) Soil volume change: Longitudinal stress may develop due to volume changes in the soil surrounding the buried pipe. The volume change may be associated with the shrink-swell behaviour of some cohesive soils or the volume expansion associated with frost heave mechanisms due to

isotropic pore water expansion and anisotropic ice lens formation, where the latter is the dominant driving mechanism (Konrad, 2001).

- (3) Inadequate bedding: Pipe bending action may occur if the backfill and pipe bedding (i.e. foundation) is not appropriately designed and prepared (Figure 3.2).



**Figure 3.1 Circumferential crack (After Seica et al., 2002)**

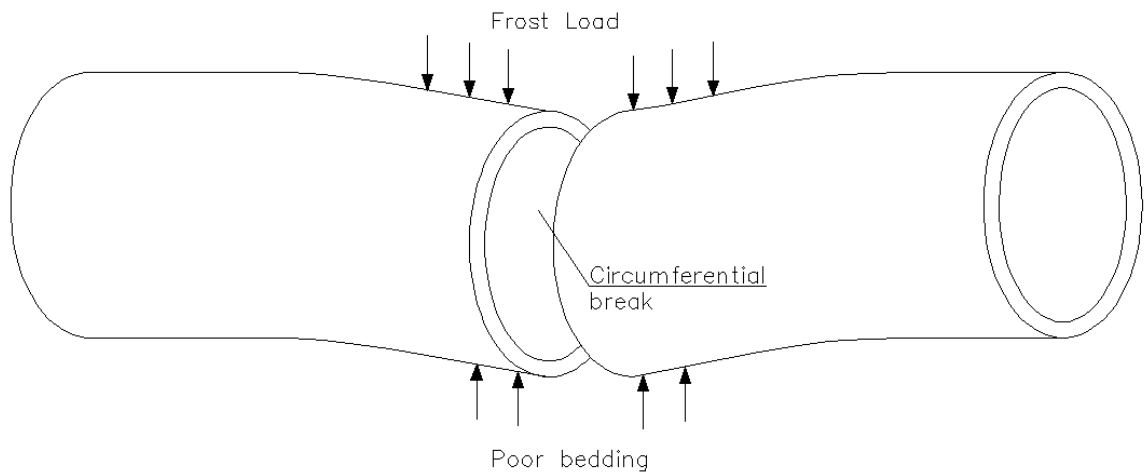


**Figure 3.2 Circumferential break**

On average, circumferential pipe fracture comprises the majority (approximately 70%) of water main breaks while other failure modes make up 30% (Rajani et al., 1996). Once the circumferential crack forms, the gap length could increase over time due to applied axial forces (e.g. thermal, adjacent tunneling action) and corrosive mechanisms.

Through a series of laboratory tests, Brown et al., (2008) compared the uniaxial tension stress-strain behavior of fabrication liner coupons with the in-situ liner material recovered during the studies conducted by Allouche et al., (2005) (i.e. Table 3.1). The observed behavior for the coupons, regardless of origin, was identical with a nonlinear (approximately bilinear) response.

**Table 3.1 Orthotropic properties (after, Allouche et al., 2005)**

Parameter			Circumferential	Longitudinal
Term	Symbol	Unit		
Elastic Modulus	$E$	GPa	2.0	3.0
Yield Strain	$\varepsilon_y$	(%)	1	0.9
Yield Stress	$\sigma_y$	MPa	23.5	24
Ultimate Stress	$\sigma_u$	MPa	61	88.4

The post-yield tangent modulus in the circumferential direction was greater than the longitudinal direction by a factor of 3.5, which indicates a stiffer post-yield response. Physical modelling and numerical simulation studies on the local buckling response of high strength steel pipe suggest the anisotropic behavior of the CIPP liner may trigger bifurcation mechanisms in the longitudinal direction through interaction between the axial and circumferential mode response when subject to combined loads of internal pressure and bending (e.g. Fatemi and Kenny, 2017; Kenny et al., 2016).

Brown et al., (2014) used continuum FEA to examine the performance of the CIPP liner for LS3, as defined by Allouche et al., (2005). The numerical simulations observed no significant differences in the hoop or axial bending stress, for the 700 kPa maximum surge reference pressure, when using 3D continuum (Brown et al., 2014) or axisymmetric (Allouche et al., 2005) modelling approaches. The FEA indicated the effects of interface

friction were not significant for this limit state and the initial (short term) circumferential material properties could be used to predict the burst pressure. The study recommended an assessment of strength reduction due to creep on the burst limit state.

### 3.3 Problem Statement and Study Objectives

The host pipe may develop a circumferential crack due to the local tensile stress state exceeding the fracture resistance of the host pipe material or may be caused by other mechanisms (e.g. wall loss due to corrosion). The CIPP liner pipe has an outer diameter,  $D$ , liner wall thickness,  $t$ , external cast iron pipe wall thickness,  $t_p$ , and is subject to a uniform internal pressure (Figure 3.3). In response to the imposed external geotechnical loads and relative pipe rotation, the circumferential crack may extend and create a local gap defect in the host pipe wall of width,  $g$ .

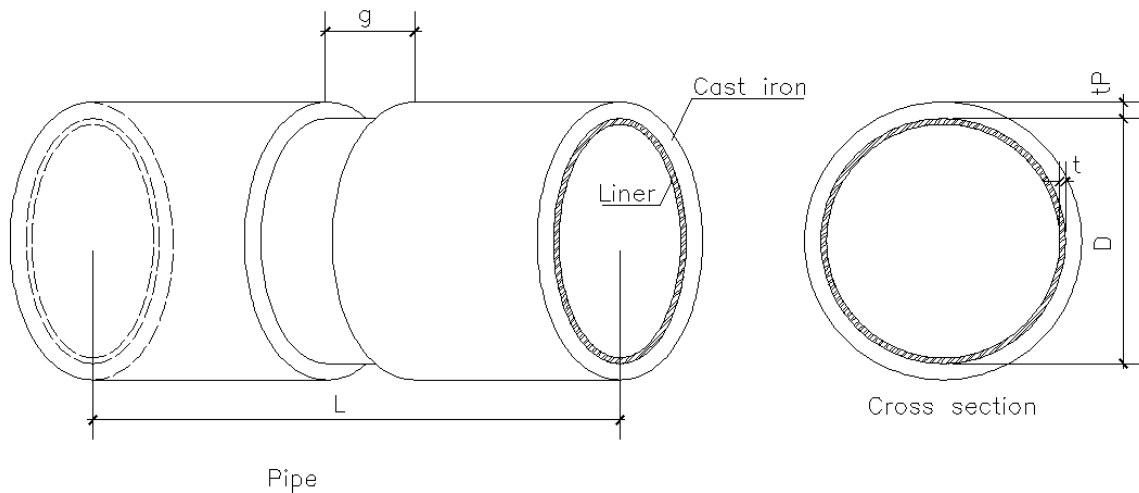


**Figure 3.3 Principal geometric parameters for the CIPP liner and cast iron pipe with circumferential crack**

In this study, the limit state for the liner section spanning across a gap in the cast iron pipe is examined using continuum finite element modelling procedures. A sensitivity analysis is conducted across a range of practical design parameters. The liner response is assessed with respect to axial, hoop and equivalent stress states, radial liner displacement and longitudinal profile response. The objective was to assess the effects of a gap defect (i.e. loss of contact) between the host pipe and CIPP Class II liner for two loading scenarios that included the (1) gap development due to deterioration mechanisms (e.g. splitting, corrosion) post-rehabilitation activities, and (2) gap development during operations due to relative ground movement causing axial slip (e.g. subsidence, tunneling, trenchless construction). For each of these scenarios, the initial fracture defect may extend or grow and create a local gap defect in the host pipe wall of width,  $d$ . The first scenario considers a rehabilitated pipe with a Class II CIPP liner that is being brought back into service (i.e. re-pressurization) with existing defects or discontinuities between the host pipe and liner. The second analysis case considers an intact host pipe/CIPP liner system experiencing relative ground motion, while in operation, that causes a gap to develop at a location where relative slip may occur (e.g. joint, circumferential crack or ring fracture).

### **3.4 Finite Element Modelling Procedures**

#### **3.4.1 Pipe Geometry, Topology and Boundary Conditions**

To reduce the computational expense, a one-quarter pipe model was used in the analysis (Figure 3.4) with the plane of symmetry located at the pipe mid-length, normal to the pipe longitudinal axis and in-plane with the pipe circumference (i.e. global XY-plane).

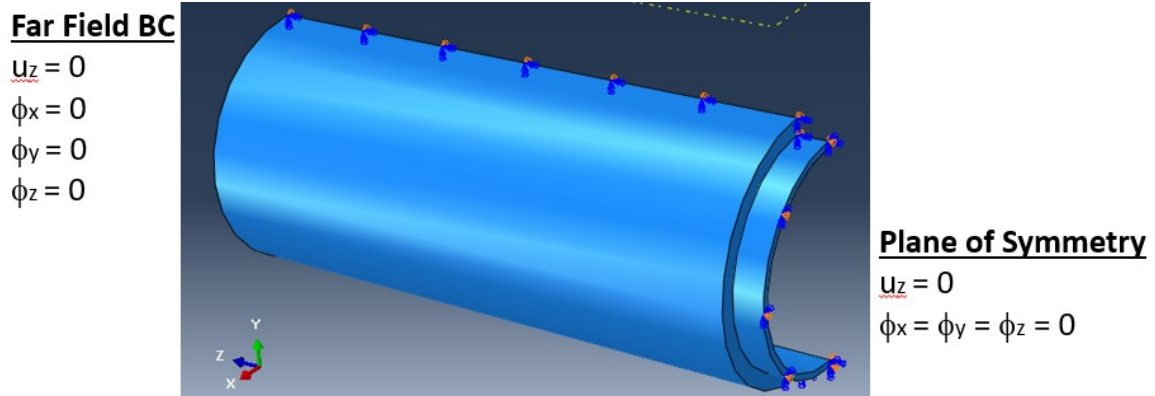


**Figure 3.4 One-quarter model of gap defect**

The CIPP liner and host pipe were modelled using the 3D, 8-node general purpose continuum element (C3D8I), with three translational degrees of freedom per node, that is a lower-order quadrilateral enhanced by an incompatible mode to improve element bending behavior. The incompatible deformation mode is used to mitigate ‘shear locking’ effects, which can be observed in fully integrated first-order isoparametric elements, and artificial stiffening due to Poisson's effect when subject to bending. For the load conditions and deformation modes examined in this study, these mechanisms are not of direct significance; however, the observed behavior will provide a baseline in the following companion study examining the effects of local defects on the CIPP liner mechanical behavior when subject to flexural loads.

For the cast iron (host pipe) section, which has lost structural integrity due to the formation of a gap (i.e. right pipe end as shown in Figure 3.4), the boundary condition was modeled as unconstrained in the radial (XY-plane) and longitudinal (XZ-plane) pipe directions. The circumferential interface between the cast iron/CIPP liner accounted for

tangential friction forces due to normal contact pressure. The boundary conditions for the opposite pipe end (i.e. left pipe end as shown in Figure 3.4), was modeled as longitudinally constrained (i.e. fixed) and radially unconstrained (i.e. free). The longitudinal constraint accounted for the virtual anchor that develops due to relative motion or slip between the host pipe and surrounding soil, which was established through an analytical solution. For the CIPP liner, centerline section (i.e. right hand side) was fixed while the other end was unconstrained with the longitudinal virtual anchor developing naturally in the numerical simulation. In the radial direction, the CIPP liner was allowed to freely expand when subject to internal pressure with plane sections remaining plane during the analysis.

### **3.4.2 Solution Procedures and Material Properties**

The three-dimensional (3D) continuum finite element analysis was conducted using the software program Abaqus v6.13. Nonlinear, static stress analysis, finite element modeling procedures, with Newton-Raphson iterations, were used to account for large deformations and plastic material behavior in the CIPP liner, and interface contact between the CIPP liner and host pipe. Default solution controls and convergence criteria was used in the analysis.

The CIPP liner elastic constitutive behavior was modelled using orthotropic material parameters, which must be consistent with the material orientation in the local coordinate system. Based on the study by Brown et al., (2014), the material properties, assigned for each material direction, are summarized in Table 3.2 for the elastic modulus ( $E$ ),

Poisson’s ratio ( $\nu$ ) and shear modulus ( $G$ ). The cast iron pipe material properties were defined as an elastic modulus of 120 GPa with a Poisson ratio of 0.3. In the numerical simulations, the mechanical deformation response of the cast iron pipe remained in the linear elastic range.

**Table 3.2 Orthotropic elastic material properties**

Elastic Modulus			Poisson’s Ratio			Shear Modulus		
$E_{11}$	$E_{22}$	$E_{33}$	$\nu_{12}$	$\nu_{13}$	$\nu_{23}$	$G_{12}$	$G_{13}$	$G_{23}$
(GPa)	(GPa)	(GPa)	(#)	(#)	(#)	(GPa)	(GPa)	(GPa)
2.0	3.0	2.0	0.3	0.3	0.3	1.0	1.0	1.5

The nominal (engineering) stress-strain data, determined from laboratory tests, was modified in order to create true stress-strain relationships (Figure 3.5). The anisotropic stress-strain relationships for the CIPP liner, in the longitudinal and circumferential directions, were based on the data provided by Brown et al., (2008). The plastic material response was defined using the Hill potential function. The Hill potential function relates the anisotropic behavior through a stress ratio parameter with the datum defined by the reference stress parameter.

In this study, the reference stress-strain curve was the circumferential material behavior with a stress ratio of 0.94, which is relative to the longitudinal stress-strain material behavior. As shown in Figure 3.6, this approximation is reasonably accurate for true strain magnitudes less than 0.01, which is greater than the predicted liner strain for this study. As discussed by Fatemi and Kenny (2017), depending on the nature of the anisotropic behavior, then the Hill potential function could be utilized for larger strain

magnitudes associated with local buckling of high strength steel pipelines subject to internal pressure and bending loads.

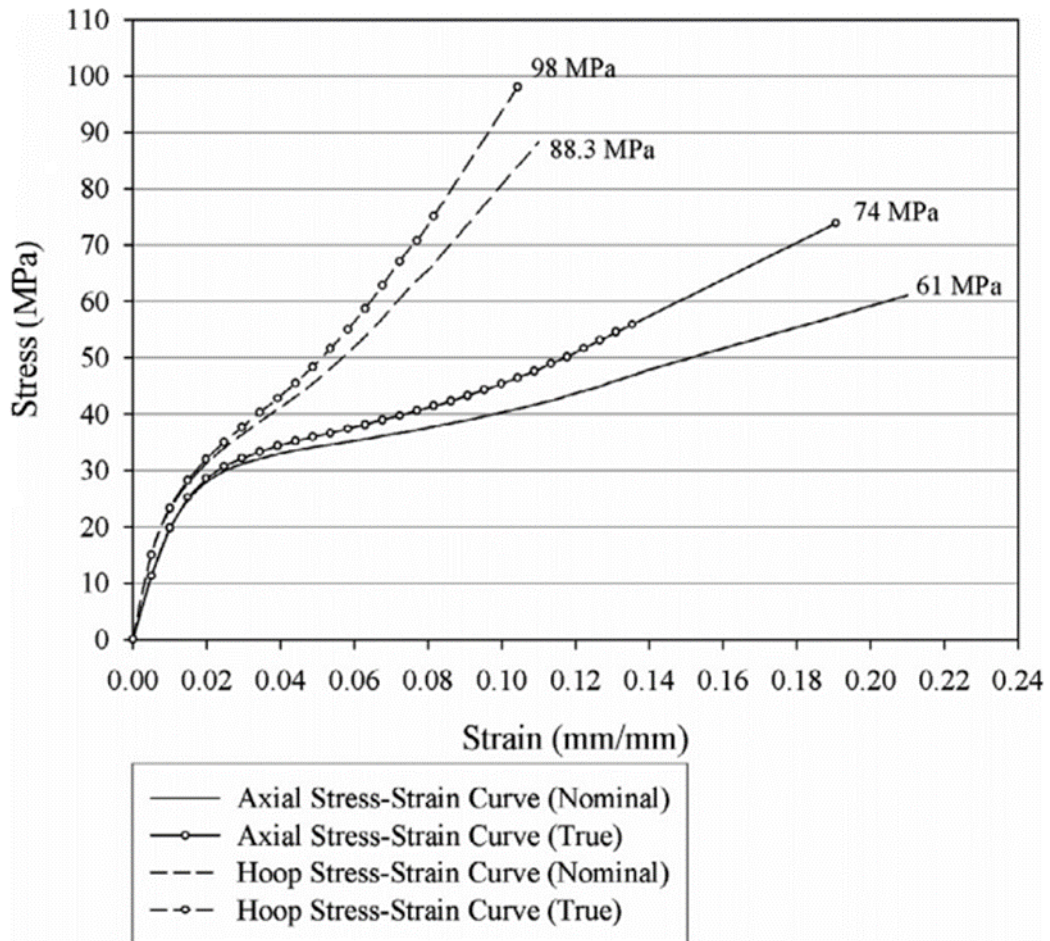


Figure 3.5 Stress-strain curves (After Brown et al., 2008)

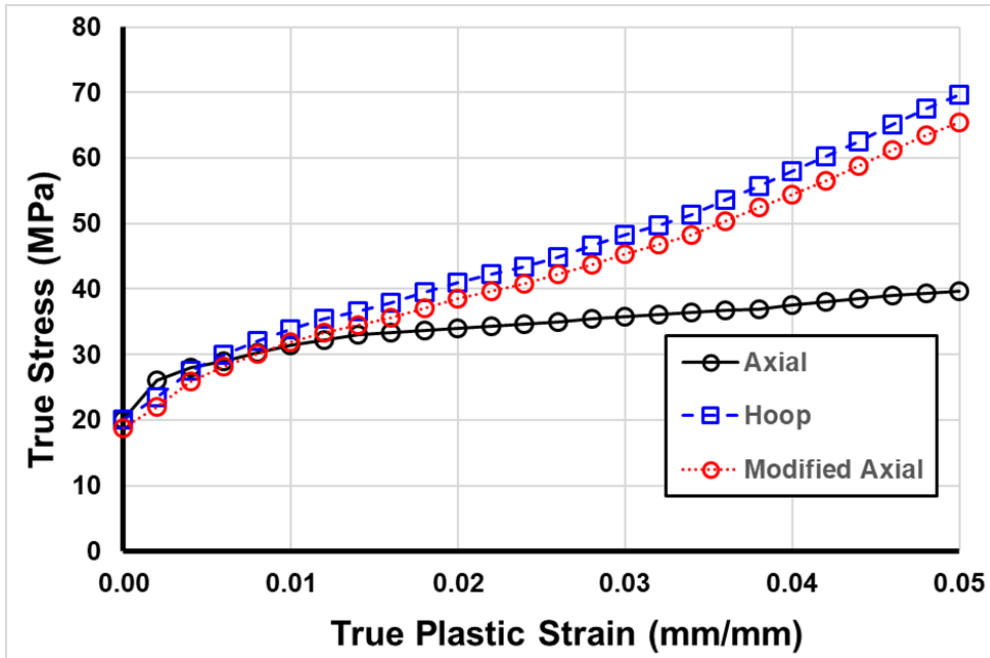


Figure 3.6 Anisotropic material properties based on Hill potential function

### 3.5 Assessment of Gap Defects on CIPP Liner Mechanical Response

#### 3.5.1 Parameter Study

In this study, four key parameters that influence the CIPP liner mechanical behavior are assessed including the CIPP liner outside diameter to CIPP wall thickness ratio ( $D/t$ ), host pipe gap length to host pipe inside diameter ratio ( $g/D$ ), hoop stress due to internal pressure to yield stress ratio for the CIPP liner ( $\sigma_h/\sigma_y$ ), and CIPP liner/host pipe interface friction coefficient ( $\mu$ ). Two pipe diameters of 1829 mm and 152 mm are examined with the study parameter range summarized in Table 3.3, 3.4. In this chapter, the CIPP liner/host pipe interface friction coefficient was selected as 0.2 and 0.4. A virtual anchor naturally develops for these interface friction analysis cases with limited sensitivity in the observed response, thus a fully bonded interface is not required.

**Table 3.3 Parameter range assessed of 1829 mm**

Parameter		Range
Term	Symbol	
Dimension ratio	$DR$	140, 80 & 50
Gap ratio	$g/D$	2.5%, 5%, 10% & 25%
Hoop stress ratio	$\sigma_h/\sigma_y$	0.4, 0.8
Friction coefficient	$\mu$	0.2, 0.4

**Table 3.4 Parameter range assessed of 152 mm**

Parameter		Range
Term	Symbol	
Dimension ratio	$DR$	60, 35
Gap ratio	$g/D$	2.5%, 5%, 17.8%, 10% & 25%
Hoop stress ratio	$\sigma_h/\sigma_y$	0.4, 0.8
Friction coefficient	$\mu$	0.2, 0.4

This study examined two mechanisms for gap development that included (1) localized deterioration (e.g. ring splitting, aggressive corrosion) with loss of host pipe wall and relative contact with CIPP liner and (2) axial motion of the host pipe where the pipe may experience relative slip (e.g. ground motion and subsidence due to adjacent geotechnical works such as tunneling, mining or earthquake) at a joint that exposes the CIPP liner. The FEA analysis explored the stress and deflection response across the parameter range.

### 3.5.2 CIPP Liner Stress

The relationship between axial stress and normalized gap length, across a range of hoop stress to yield stress ( $\sigma_h/\sigma_y$ ) and nominal CIPP liner diameter to wall thickness ( $D/t$ ) ratios, is presented in Figure 3.7. The normalized gap length ( $g/D$ ) was defined as the gap

distance ( $g$ ) divided by the nominal diameter ( $D$ ) of the CIPP liner. As the liner stiffness increases (i.e. from  $D/t = 140$  to  $D/t = 50$ ), the axial stress responses demonstrate transitions from a bilinear to approximately linear relationship with increasing normalized gap length ( $g/D$ ). The maximum axial stress (14.3 MPa) occurs for the most flexible ring stiffness (i.e.  $D/t = 140$ ) with the largest normalized gap ( $g/D$ ) distance. Across the parameters examined, the transition point for slope change in the response occurs at normalized gap ( $g/D$ ) distance of  $0.10D$ .

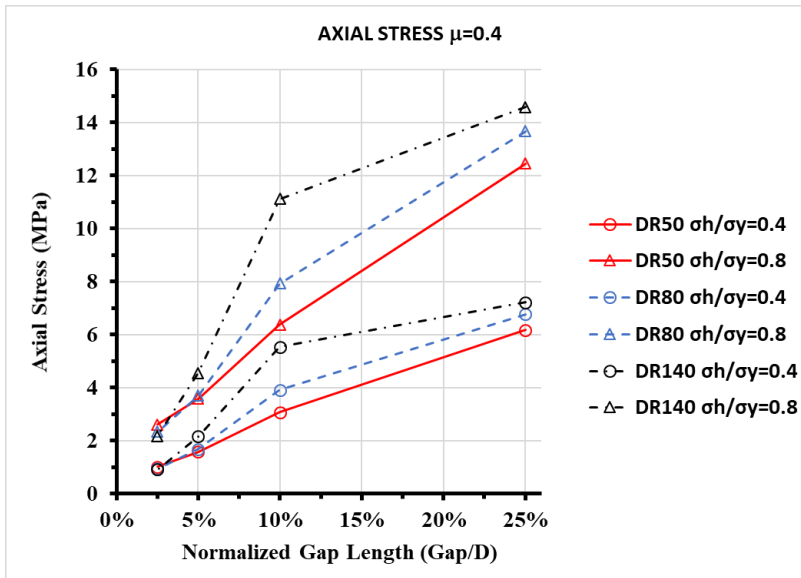


Figure 3.7 Axial stress

The equivalent stress (i.e. von Mises stress) response exhibits a similar relationship as the axial stress response shown in Figure 3.8. As the liner stiffness increases (i.e. from  $D/t = 140$  to  $D/t = 50$ ), the equivalent stress responses demonstrate transitions from a bilinear to approximately linear relationship with increasing normalized gap length ( $g/D$ ). Across the parameters examined, the transition point for slope change also occurs at normalized gap ( $g/D$ ) distance of  $0.10D$ . There is an obvious tendency that the maximum equivalent stresses for both hoop stress to yield stress ratios (i.e.  $\sigma_h/\sigma_y=0.4, 0.8$ ) converge to similar values at the largest normalized gap distance (i.e.  $g/D = 0.25$ ), respectively. The greatest equivalent stress (17.0 MPa) occurs in the case of medium stiffness (i.e.  $D/t = 80$ ) with the largest normalized gap distance.

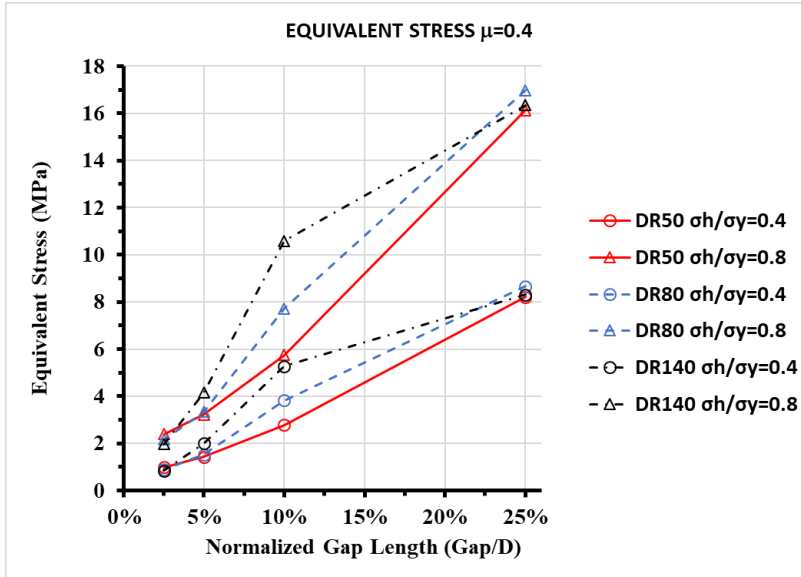


Figure 3.8 Equivalent (Von Mises) stress

### 3.5.3 CIPP Liner Radial Deflection

For a nominal wall thickness greater than approximately 10% of the inner radius, the cylinder can be considered as thick-walled cylinder (Figure 3.9) and the variation of stress with radius cannot be ignored (Ugural, 2003). When a thick-walled cylinder is subjected to uniform internal or external pressure, the radial displacement  $u$  is calculated with Eq 3.1 (derived by G.Lame, 1833), which is for plane stress condition and based on isotropic material. This equation is also applicable in thin-walled cylinder. Therefore, the radial displacement  $u$  can be used as theoretical solution for an unconfined CIPP liner subject to uniform internal pressure.

$$u = \frac{1-\nu}{E} \frac{(a^2 p_i - b^2 p_o) r}{b^2 - a^2} + \frac{1+\nu}{E} \frac{(p_i - p_o) a^2 b^2}{(b^2 - a^2) r} \quad \text{Equation 3.1}$$

$a$ —inner radius

$b$ —outer radius

$r$ —location at which the displacement is calculated

$p_i$ —internal pressure

$p_o$ —external pressure

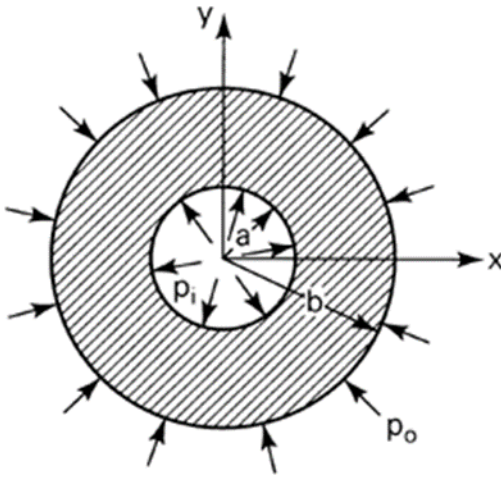


Figure 3.9 Thick-walled cylinder (From Ugural, A.C et al., 2003)

As the gap ratio ( $g/D$ ) increases, the axial stress (shown in Figure 3.7) increases due to a local flexural response (i.e. curvature change) of the CIPP liner through interaction with the host pipe and deflection through the gap. This is supported through observations on the radial displacement of the CIPP liner, as shown in Figure 3.10, where the relationship between the normalized radial displacement of the CIPP liner with the axial distance measured from the gap center along the pipe longitudinal axis (i.e. length) is presented.

The normalized radial displacement ( $ur/ut$ ), which is measured in the CIPP liner, is normalized with respect to the theoretical radial displacement of an unconfined CIPP liner pipe subject to internal pressure using Eq 3.1. The normalized axial distance is the distance measured along the pipe axis, starting from the gap center, with respect to the CIPP liner diameter. For the data presented in Figures 3.10 and 3.11, the analysis parameters included a CIPP liner diameter of 1829 mm,  $g/D$  ratio of 25%, 10% (i.e.

gap=450 mm, 180 mm, respectively), hoop stress ( $\sigma_h/\sigma_y$ ) ratio of 0.4, 0.8 with a frictional interface ( $\mu = 0.4$ ) condition.

Across these examined cases, the axial and equivalent (von Mises) stress state remains within the elastic range. The normalized displacements under different hoop stress ratio (i.e.  $\sigma_h/\sigma_y = 0.8, 0.4$ ) with the same  $D/t$  ratio generally demonstrate the same deflection pattern. The normalized maximum radial displacement is somewhat greater than the theoretical displacement, which indicates that the liner state at the center of the gap is close to an unconfined liner subject to internal pressure. The difference between them may be attributed to the orthotropic material properties used in the FEA simulation of the liner response that is not accounted for in the theoretical solution.

In contrast, the normalized radial displacement for a variation in the liner  $D/t$  ratio exhibits distinct deformation patterns with normalized gap distance. This may be attributed to the relationship among relative stiffness effects on the pipe deformation mode response including circumferential (i.e. pipe ring) and axial (i.e. bending stress and deformations through the gap) material and mechanical behavior of the CIPP liner, discretization (i.e. number and type of elements) effects, and edge constraint from the gap and relatively stiff host pipe. Particularly, the maximum radial displacement amplitude occurs at the gap center (i.e. normalized distance = 0), in the case of  $D/t$  ratio 140, which has the least ring stiffness.

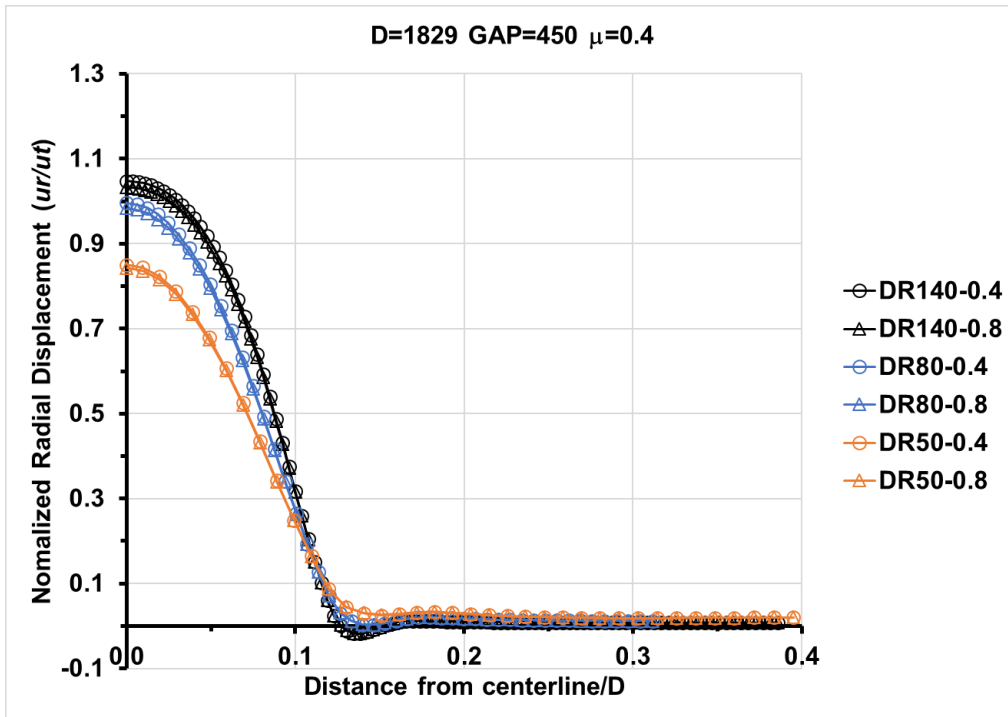


Figure 3.10 Normalized radial displacement profile for  $D=1829$  mm,  $GAP=450$  mm,  $\mu=0.4$

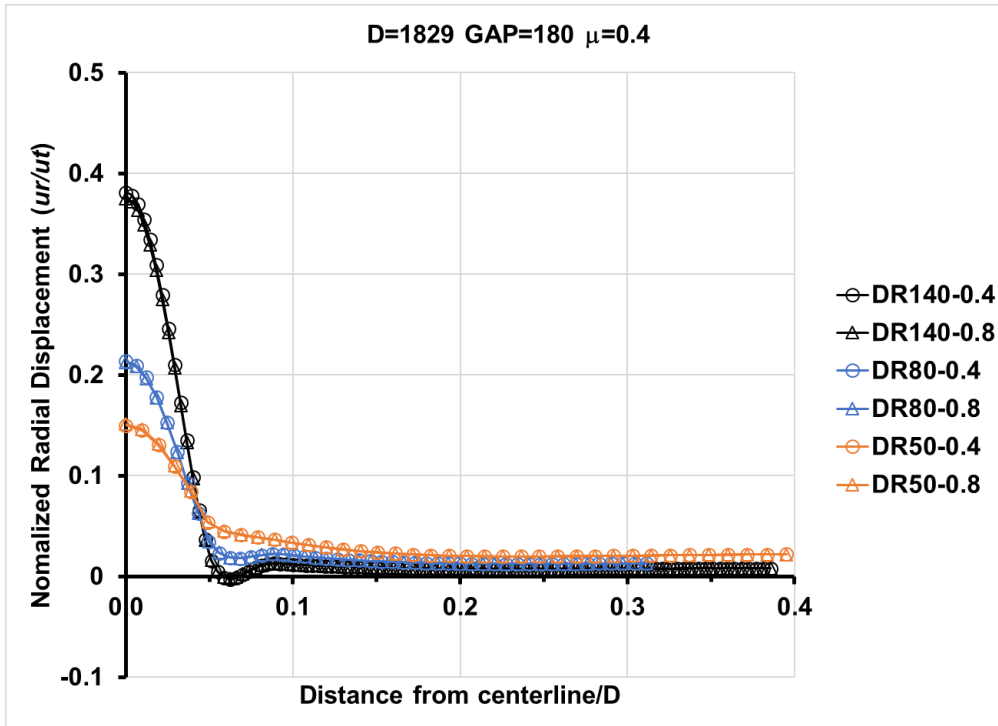


Figure 3.11 Normalized radial displacement profile for  $D=1829$  mm,  $GAP=180$  mm,  $\mu=0.4$

As shown in Figure 3.10, the normalized radial displacement profile exhibits a non-linear, sinusoidal pattern with distance from the gap center that tends toward zero amplitude due to the host pipe radial constraint. Effect of the gap defect edge or shoulder on the liner radial displacement can be observed at normalized distance of 0.125. This corresponds to void ratio of 0.25 (i.e.  $450\text{mm}/1829\text{mm}=0.25$ ), since symmetrical boundary conditions were employed in the numerical models. Interaction effects between the host pipe gap and local relative stiffness (i.e. gap edge or shoulder) were also observed. For higher liner dimension ( $D/t = 140$ ) ratio, the negative normalized radial displacement magnitudes are due to changes in local curvature within the CIPP liner in response to the applied internal pressure with changes in the local relative stiffness, between the gap space and intact host pipe, and resultant lateral deflection through the

void. The amplitude of the negative radial deflection, adjacent to the gap edge, increases with increasing liner dimension ( $D/t$ ) ratio. Figure 3.11 (i.e.  $g/D=0.10$ ) generally shows the same trend as shown in Figure 3.10. With the decrease of the dimension ratio (i.e. from  $D/t=140$  to  $D/t=50$ ), the maximum radial displacement at the centerline decreases. Besides that, comparing to case  $g/D=0.25$ , the magnitude of the maximum radial displacement at the centerline significantly decreases (e.g.  $ur/ut=0.38$  in case  $D/t=140$ ). This is because the constraint provided by the cast iron pipe in the case  $g/D=0.10$  is much stronger than that of case  $g/D=0.25$ . Figure 3.12 shows the radial displacement contour.

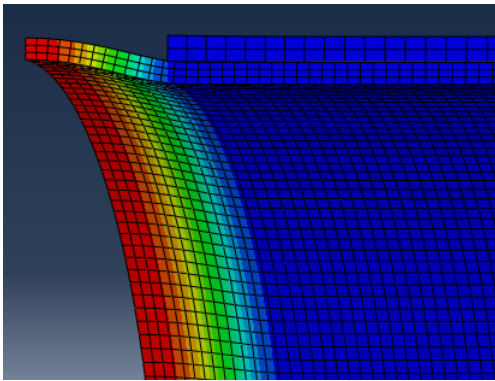


Figure 3.12 Radial displacement for  $D=1829$  mm,  $GAP=180$  mm,  $\mu=0.4$ ,  $D/t=50$

### 3.5.4 Influence of Interface Friction Coefficient

The influence of the CIPP/host pipe interface friction coefficient (i.e.  $\mu = 0.2, 0.4$ ) on the pipe stress and deformation response was also investigated. As the relative interface friction forces increase, which may be due to increased normal forces (e.g. higher internal pressure), higher interface friction coefficient ( $\mu$ ) and interface bond strengths (i.e. shear stress limits), then the required mobilization distance to develop a virtual anchor point (e.g. Palmer et al., 1981) reduces. The anchor point occurs at the location where the relative displacement between the liner and the host pipe is zero. This relationship was

observed in the current study with respect to increasing internal pressure and interface friction coefficient.

The axial displacement of the liner and the host pipe is presented in Figures 3.13 and 3.14. The virtual anchor develops at the location where the difference of axial displacement between the liner and the host pipe becomes zero. For the higher coefficient of friction ( $\mu = 0.4$ ), the virtual anchor occurs at approximate 1100 mm, while at 1400 mm when the lower coefficient of friction ( $\mu = 0.2$ ). It needs a longer distance to develop virtual anchor when the coefficient of friction is smaller. This is supported by the shear stress developing on the interface (Figure 3.15). The shear stress should decrease to zero when there is no slip between the liner and the pipe. Compared to the maximum shear stress value (0.47 MPa) developed on the interface, then a stress of 0.5 kPa can be considered approximately zero. The corresponding distances are approximately 1100 mm and 1400 mm for an interface friction coefficient of 0.4 and 0.2, respectively. In both cases, the axial displacement of the liner and pipe along the axial direction shows the same pattern. As shown in Figures 3.13 and 3.14, the axial displacement of the liner experiences a rapid increase before the location  $L=180$  mm and then drops dramatically until the location  $L=230$  mm. After that, it rises again until the virtual anchor occurs where there is no relative displacement between the liner and the pipe. Since the other end of cast iron pipe is constrained longitudinally, the axial displacement of the liner starts to decrease after the virtual anchor.

In terms of axial stress, equivalent stress and radial deflection, there is no significant difference observed between these two coefficients of friction cases.

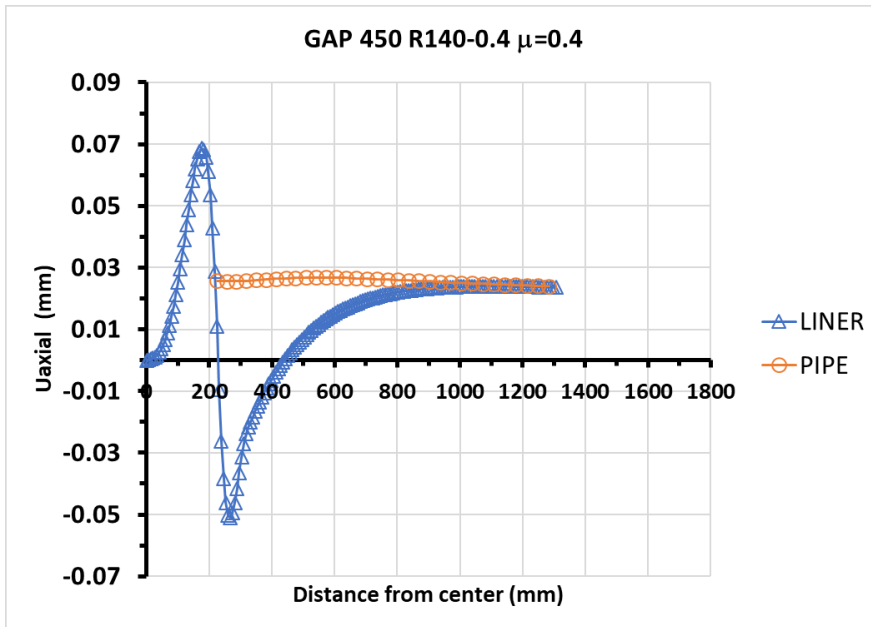


Figure 3.13 Axial displacement profile ( $\mu = 0.4$ )

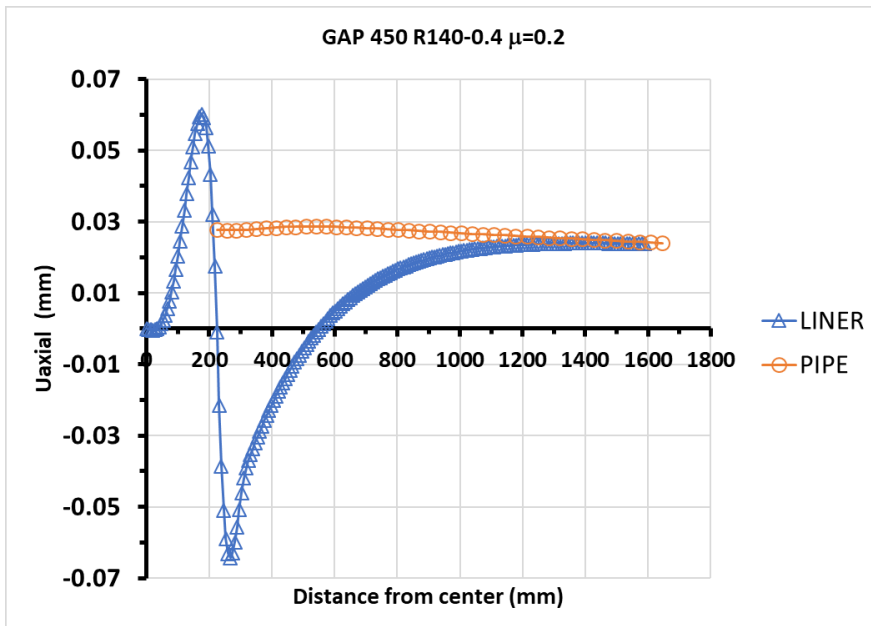


Figure 3.14 Axial displacement profile ( $\mu = 0.2$ )

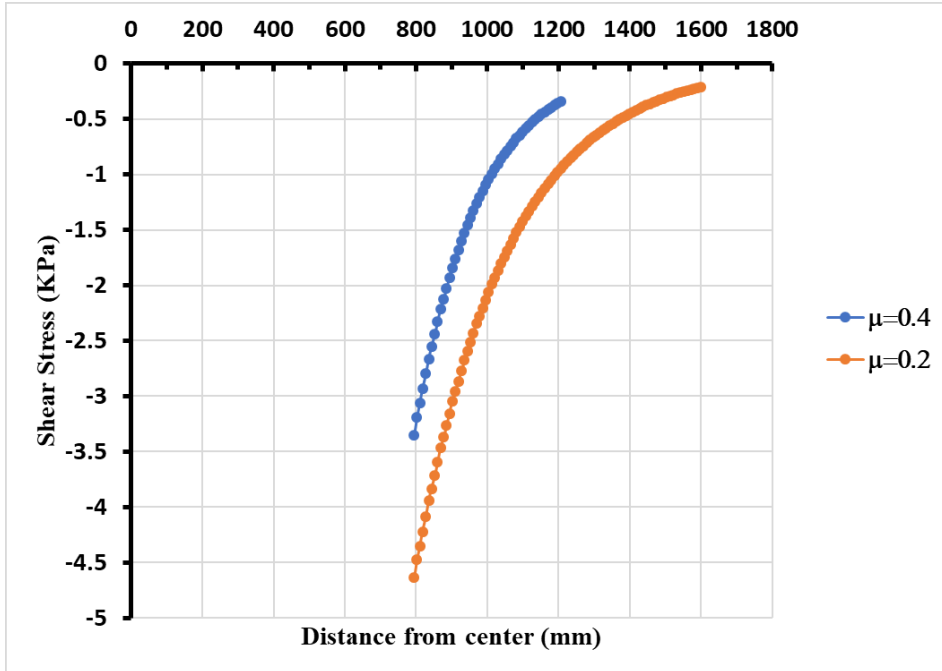


Figure 3.15 Shear stress along pipe length

### 3.6 Gap Defects Due to Relative Axial Motion

Previous analysis in this chapter considered gap defect existing before loading. There could be another scenario that the gap forms with the presence of the internal pressure. In this case, the gap is progressively forming with the axial movement of the host pipe which could be attributed to horizontal vehicle load, seismic load or other loads that could cause differential horizontal movement of the soil.

In order to model the process of gap forming, a three-dimensional model was developed. Both ends of the cast iron host pipe are unconstrained radially and longitudinally. An axial displacement of 2.5 mm was applied at the end of the host pipe that has lost its structural integrity. In the radial direction, the liner was unconstrained and allowed to freely expand when subject to internal pressure with plane sections remaining plane during the analysis.

In the longitudinal direction, the end of the liner at centerline is fixed while the other end is unconstrained. Table 3.5 shows the parameter range assessed.

**Table 3.5 Parameter range assessed of 152 mm in relative axial motion**

$D/t$	$t$ (mm)	$\sigma_h/\sigma_y$	Pressure (KPa)	$\mu$	Job
60	2.500	0.4	267	0.2	J-1
				0.4	J-2
		0.8	533	0.2	J-3
				0.4	J-4
35	4.200	0.4	457	0.2	J-1
				0.4	J-2
		0.8	914	0.2	J-3
				0.4	J-4

Figure 3.16, 3.17 show relations between the maximum axial stress and gap length. Both Figures of different  $D/t$  ratios (i.e. 60, 35) show similar axial results for each  $\sigma_h/\sigma_y$  ratio. As the gap length develops, the maximum axial stress of the liner increases in a nonlinear relation. Not surprisingly, the axial stresses of the case with higher  $\sigma_h/\sigma_y$  ratios are greater than that of those with lower  $\sigma_h/\sigma_y$  ratios. The friction coefficient has the same effect on axial stress as  $\sigma_h/\sigma_y$  ratio does. The maximum axial stress reaches its peak values as the gap reaches 5 mm in each case, except in the case  $\sigma_h/\sigma_y=0.4$ ,  $\mu=0.2$  (i.e. J-1). In this particular case, the axial stress reaches its peak value at gap =3.2 mm. After that, the axial stress does not change. This is because the friction force between the liner and cast iron pipe reaches the maximum value and the liner. Comparing to the results from the cases with gap exiting before loading, the magnitude of the axial stress is much greater when the gap is formed with the presence of the internal pressure. This indicates that the effects

of gap development of pressure pipe under axial motions have a greater impact on liner performance than that of a wider gap zone.

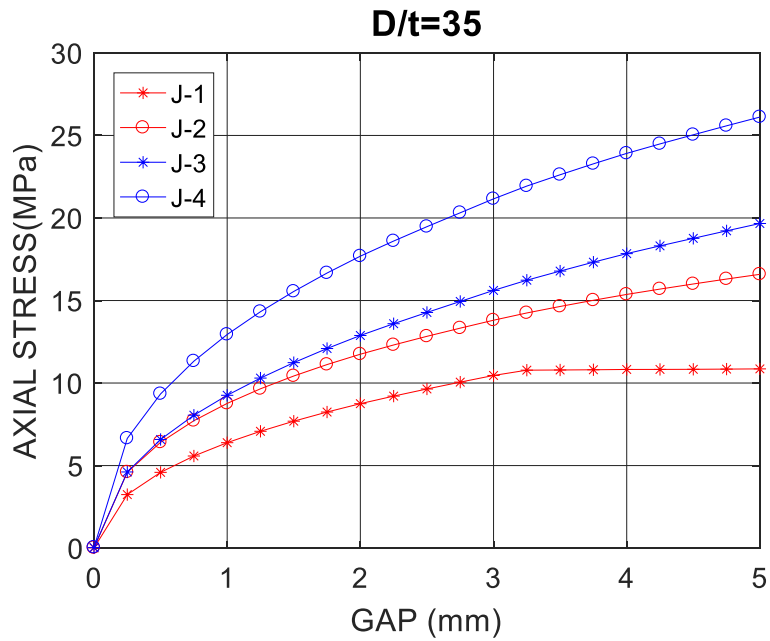


Figure 3.16 Maximum axial stress vs gap length of  $D/t=35$

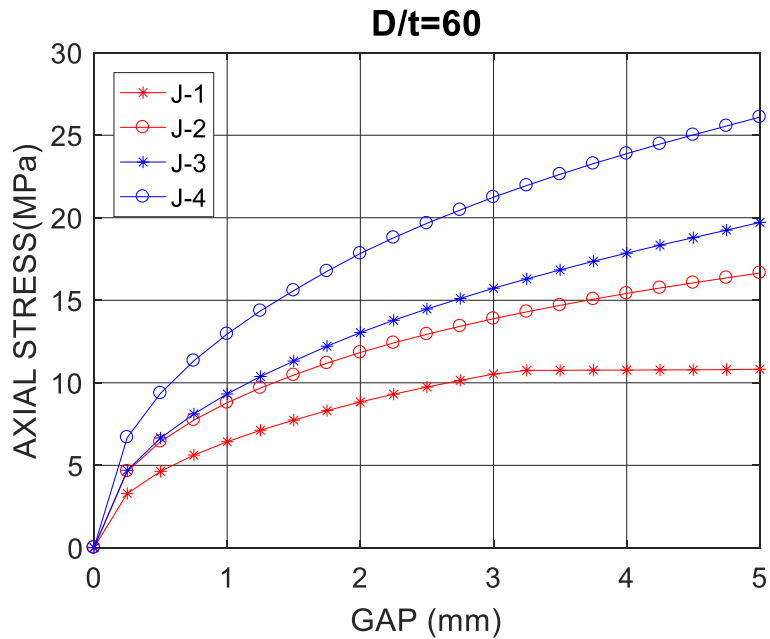


Figure 3.17 Maximum axial stress vs gap length of  $D/t=60$

## **Chapter 4: Influence of Local Gap Defect for Combined Internal Pressure and Flexural Loading**

### **4.1 Preface**

This chapter is prepared in the manuscript format. The current status of this manuscript is “prepared for submission” where the publication venue has yet to be identified. The principal investigator was Xiaohan He where he was the primary responsible person to define the problem statement, establish the analysis matrix used in the parameter study, develop the numerical modelling procedures, conduct the numerical simulations, and report on the data synthesis, analysis and conclusions. Guidance, mentorship and editorial support was provided by the supervisor, Dr. Shawn Kenny, in the development of the conference manuscript.

### **4.2 Introduction**

Allouche et al., (2005) identified six possible limit states that could affect the liner performance, stability and integrity. The fourth limit state occurs when the CIPP liner section spans a local ring fracture or pipe joint, within the host pipe, and is subjected to rotation or moment loading (Figure 4.1). The rotation angle ( $\alpha$ ), of one pipe segment relative to the adjacent segment, may be due to differential ground movement action (e.g. frost heave, subsidence, fault movement, liquefaction), where the net geotechnical loads impose an end moment ( $M_R$ ) on the buried pipe. The pipe response may be governed by the limiting moment ( $M_L$ ) on the compression face, or axial tension ( $T_L$ ) or equivalent stress on the opening face (tensile fibre), which may exceed the material yield stress.

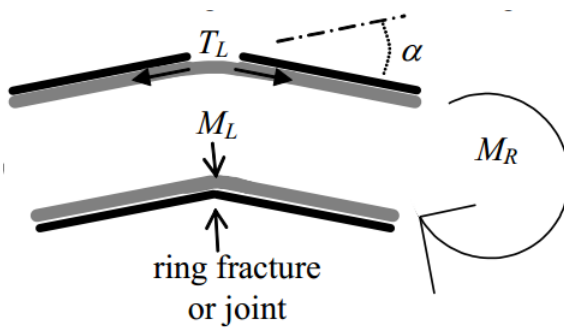
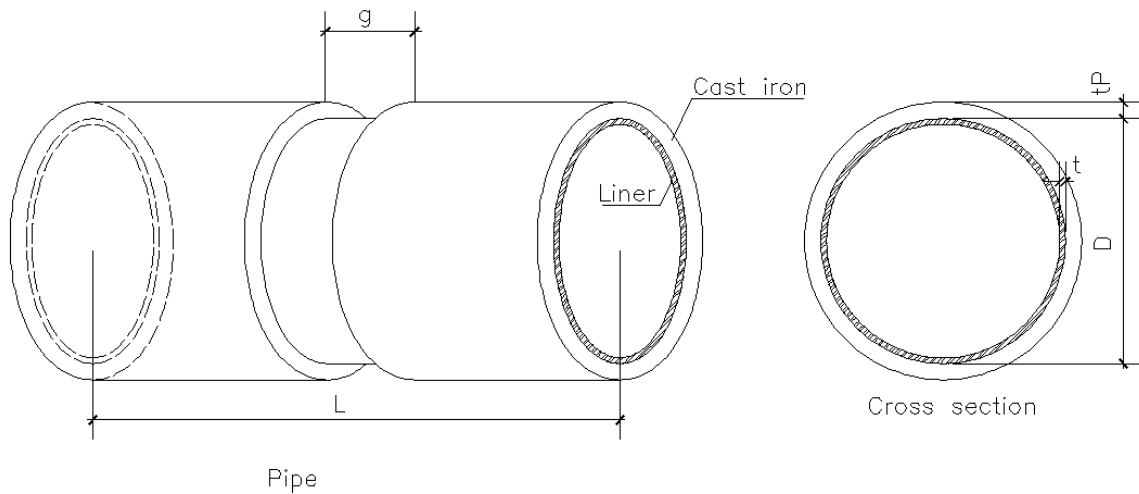


Figure 4.1 Rotation at ring fracture or pipe joint (After Allouche et al., 2005)

A recent study by Trickey et al., (2016) examined the effects of frost-induced bending moments on buried cast iron water pipes through a numerical parametric study. The sensitivity analysis assessed how pavement stiffness and trench backfill conditions influenced pipe deflection and flexural response. One of the conclusions from this study was that the longitudinal bending may be the dominant cause of failure of cast iron water pipes. In addition, pipe burial depth had the greatest impact on pipe flexural response, which is a major contributor to pipe failure due to ring fracture.

#### 4.2.1 Problem Statement and Study Objectives

The host pipe may develop a circumferential crack due to the local tensile stress state exceeding the fracture resistance of the host pipe material or may be caused by other mechanisms (e.g. wall loss due to corrosion). The CIPP liner pipe has an outer diameter,  $D$ , liner wall thickness,  $t$ , external cast iron pipe wall thickness,  $t_p$ , and is subject to a uniform internal pressure (Figure 4.2). In response to the imposed external geotechnical loads and relative pipe rotation, the circumferential crack may extend and create a local gap defect in the host pipe wall of width,  $g$ .



**Figure 4.2 Principal geometric parameters for the CIPP liner and cast iron pipe with circumferential crack**

In this study, the limit state for the liner section spanning across a gap in the cast iron pipe subject to longitudinal bending (LS4) is examined using continuum finite element modelling procedures. Although this limit state is identified by Allouche the author did not perform a detailed study on it. In Trickey's study, the author focused on the response of cast iron pipe only and the CIPP liner was not involved. This study integrates the CIPP liner and cast iron pipe with the presence of the internal pressure and flexural bending and considers the interaction between the CIPP liner and host pipe, which gives an insight of the response of the CIPP liner. A sensitivity analysis is conducted across a range of practical design parameters, which includes the pipe segment length, gap defect length, internal pressure and interface friction. The analysis also examined the influence of the essential (i.e. geometric) boundary condition on the CIPP liner mechanical response. The liner response is assessed with respect to ovality at different sections, moment-curvature relations, deformation modes and longitudinal profile response.

### 4.3 Finite Element Modelling Procedures

#### 4.3.1 Pipe Geometry, Topology and Boundary Conditions

To reduce the computational expense, a one-quarter pipe model was used in the analysis (Figure 4.3) with the plane of symmetry located at the pipe mid-length, normal to the pipe longitudinal axis and in-plane with the pipe circumference (i.e. global XY-plane).

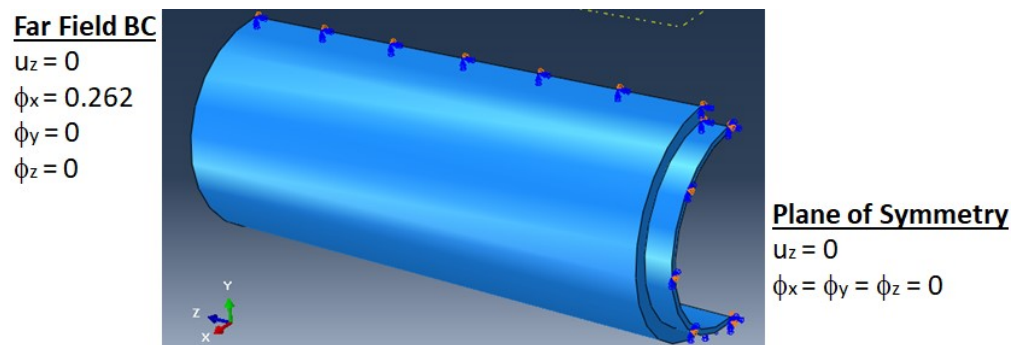
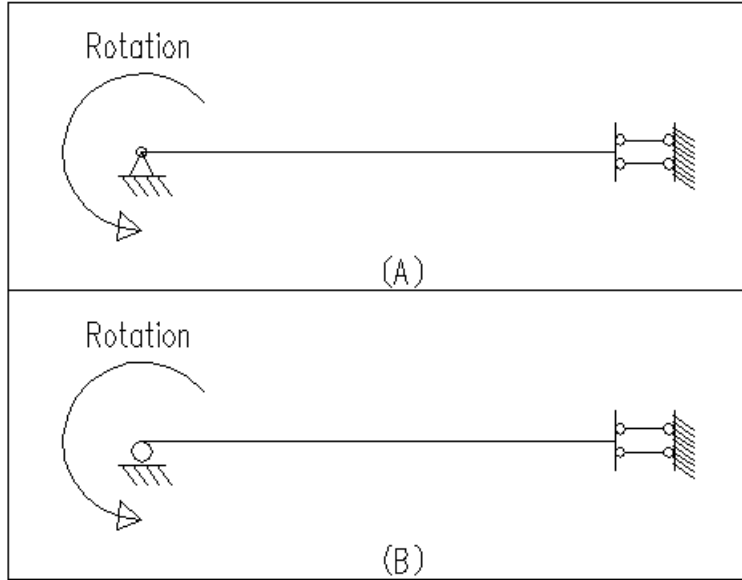


Figure 4.3 One-quarter model of CIPP liner and cast iron pipe

The CIPP liner and host pipe were modelled using the 3D, 8-node general purpose continuum element (C3D8I), with three translational degrees of freedom per node, that is a lower-order quadrilateral enhanced by an incompatible mode to improve element bending behavior. The incompatible deformation mode is used to mitigate ‘shear locking’ effects, which can be observed in fully integrated first-order isoparametric elements, and artificial stiffening due to Poisson's effect when subject to bending. For the load conditions and deformation modes examined in this study, these mechanisms are not of direct significance (e.g. Huo et al., 2016).

The edge of the cast iron host pipe that has lost its structural integrity (right hand side in Figure 4.3) is unconstrained in the radial (XY-plane) and the longitudinal (XZ-plane) pipe directions. In consideration of the virtual anchor that can develop due to relative motion and interface friction at the host pipe/soil interface, the left hand side of the host pipe, as shown in Figure 4.3, was fixed in the longitudinal pipe axis and unconstrained in the radial pipe direction.

For the CIPP liner, two boundary conditions for the far-field (i.e. left hand side in Figure 4.3) were considered to assess the effects of the boundary condition on the liner response, which are illustrated in Figure 4.4. In the radial direction, the liner was considered unconstrained and allowed to radially expand when subject to internal pressure and plane sections remaining plane during the analysis when subjected to flexural loads. In the longitudinal direction, the end of the liner at centerline (right hand side in Figure 4.3) is fixed, which represents the plane of symmetry, whereas the other end was defined as a pin or roller connection with the applied rotation to represent the effects of bending.



**Figure 4.4 Idealized models for the liner (A) Pin end (B) Roller end**

### **4.3.2 Solution Procedures and Material Properties**

The three-dimensional (3D) continuum finite element analysis was conducted using the software program Abaqus v6.13. Nonlinear, static stress analysis, finite element modeling procedures, with Newton-Raphson iterations, were used to account for large deformations and plastic material behavior in the CIPP liner, and interface contact between the CIPP liner and host pipe. Default solution controls and convergence criteria was used in the analysis.

In previous chapters, the reference stress-strain curve was the circumferential material behavior with a stress ratio of 0.94, which is relative to the longitudinal stress-strain material behavior. As shown in Figure 4.5, this approximation is reasonably accurate for true strain magnitudes less than 0.01. As discussed by Fatemi and Kenny (2017), depending on the nature of the anisotropic behavior then the Hill potential function could

be utilized for larger strain magnitudes associated with local buckling of high strength steel pipelines subject to internal pressure and bending loads. However, the true strain magnitudes exceed 0.01 in this bending case. Therefore, the longitudinal stress-strain curve was applied along both circumferential and longitudinal direction of the liner.

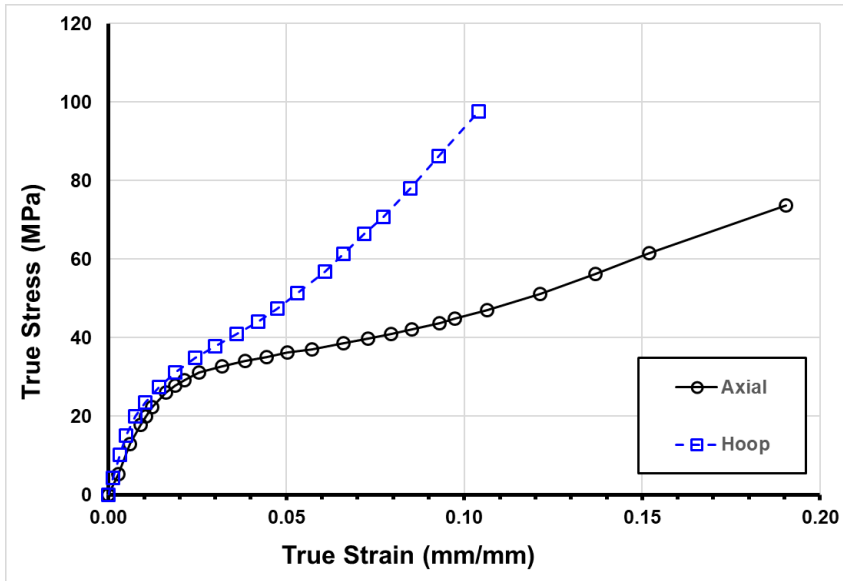


Figure 4.5 True stress-strain curves in the axial and hoop directions

#### 4.4 Assessment of Gap Defects on CIPP Liner Mechanical Response for Combined Loading

##### 4.4.1 Parameter Study

In this study, the CIPP liner outside diameter is 152 mm with a  $D/t$  of 36. Four key parameters that influence the CIPP liner mechanical behavior are assessed in this sensitivity analysis including the pipe segment length ( $L$ ), host pipe gap length to host pipe inside diameter ratio ( $g/D$ ), hoop stress due to internal pressure to yield stress ratio for the CIPP liner ( $\sigma_h/\sigma_y$ ), and CIPP liner/host pipe interface friction coefficient ( $\mu$ ). A

single pipe diameter of 152 mm is examined with the study parameter range summarized in Table 4.1.

**Table 4.1 Parameter range for 152 mm CIPP liner pipe diameter**

Parameter		Range
Term	Symbol	
Pipe length	$L$	$5D, 10D$
Gap ratio	$g/D$	10% & 25%
Hoop stress ratio	$\sigma_h/\sigma_y$	0, 0.8
Friction coefficient	$\mu$	0.2, 0.4

#### 4.4.2 Influence of Essential Boundary Conditions and Defect Gap Length

The influence of essential (i.e. geometric) boundary conditions, including pin and roller end supports (Figure 4.4), on the CIPP liner mechanical response was examined. For pipe sections subject to flexure, the pipe section ovalization provides a measure of the section beam response and stability with respect to local buckling mechanisms. The pipe section ovality was calculated, based on Equation 4.1, at three specific pipe sections located on the longitudinal axis that included the plane of symmetry (i.e. MID), and two other locations at a distance of 0.5D and 1.0D from the plane of symmetry.

$$Ovality = \frac{(D_{max} - D_{min})}{D_o} \times 100\% \quad \text{Equation 4.1}$$

$D_{max}$  — Maximum diameter of cross-section

$D_{min}$  — Minimum diameter of cross-section

$D_o$  — Nominal diameter of cross-section

The pipe section ovality-global curvature relationship is shown in Figure 4.6. In general, the type of far-field boundary condition (i.e. pin versus roller) did not have any

significant influence on the predicted pipe ovality at the same location (i.e. MID, 0.5D and 1.0D) across the global curvature magnitudes (i.e. related to compressive strain) investigated. The global curvature estimate was based on Equation 4.2.

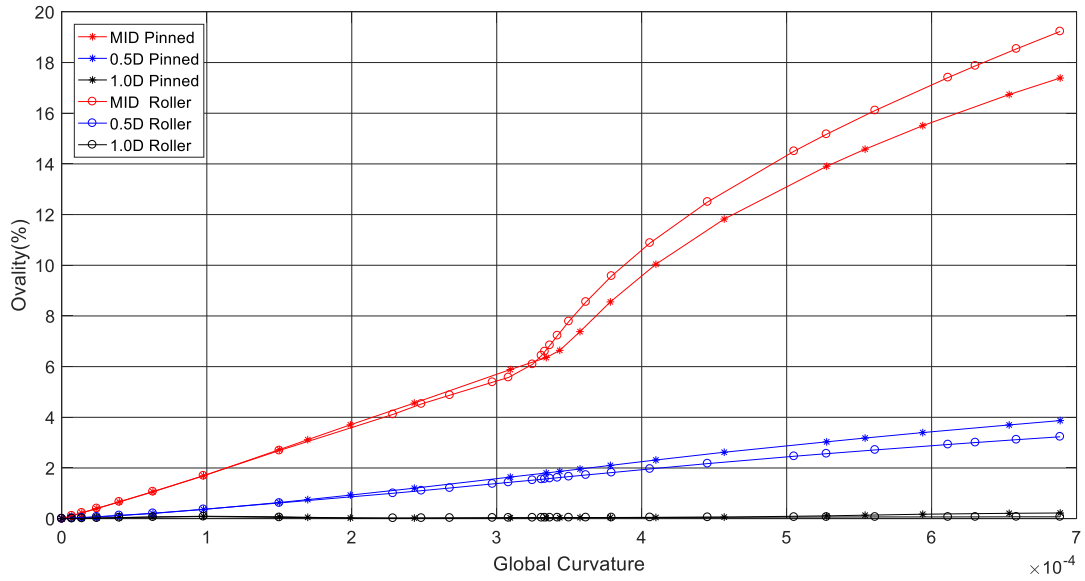


Figure 4.6 Liner ovality-global curvature relationship ( $L = 5D$ ,  $g/D = 10\%$ ,  $\sigma_h/\sigma_y = 0.8$ ,  $\mu = 0.4$ )

$$\kappa = \frac{1}{R} = \frac{\theta}{L} \quad \text{Equation 4.2}$$

$\kappa$  — Global curvature

$R$  — Radius of curvature

$\theta$  — Overall change of angle

$L$  — Length of neutral axis

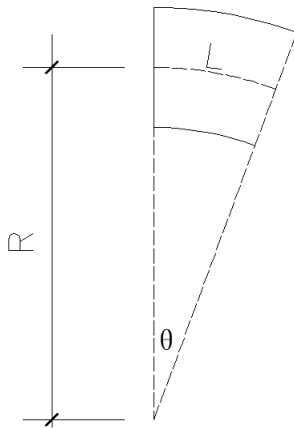


**Figure 4.7 Geometry of a segment of pipe**

The pipe ovalization-global curvature relationship is linear at all sampling points up to a global curvature of  $3.2 \times 10^{-4} \text{ mm}^{-1}$ . At the plane of symmetry (i.e. MID), a transition from a linear to non-linear relationship illustrates the localization of the deformation mechanisms associated with inward radial section collapse.

As shown in Figure 4.6, at pipe sections away from the local buckling site (i.e. 0.5D and 1.0D), the pipe ovality-curvature relationship remains linear, which is consistent with theoretical considerations of the Brazier effect of circular pipe sections subject to flexural loading effects (Brazier, 1927). The gradient of pipe ovality, which can be viewed as the

rate of change for pipe ovalization with increasing global pipe curvature for the same pipe section (e.g. MID), indicates the mechanism is localized. This is also supported by the contours of total displacement (Figure 4.8), which illustrates the localization of radially inward deformation of the liner at the centerline section (i.e. MID). At pipe sections more distant from the local collapse site (i.e. 0.5D and 1.0D) the deformation response is consistent with the Brazier effect, for bending of pipe segments subject to bending, where the section response is uniform. In reference to recent studies on the local buckling of energy pipelines, the near zero pipe ovality at the 1.0D section suggest the mechanical response is over-constrained by the pipe length and end boundary conditions (e.g. Fatemi and Kenny, 2017; Kenny et al., 2016), which has a significant moderating effect on the local buckling response. The influence of pipe length on the liner mechanical response is addressed later in this thesis study.

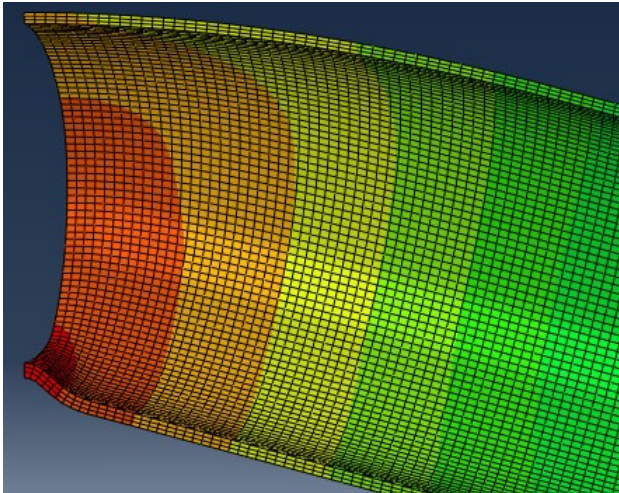


**Figure 4.8** Total displacement contour of 5D case ( $g/D = 10\%$ ,  $\sigma_h/\sigma_y = 0.8$ ,  $\mu = 0.4$ )

The magnitude of pipe ovality for the roller boundary condition models was observed to be greater than the pinned counterpart models only at the pipe mid-length (i.e. MID) section (Figure 4.6), where the liner deformation mode was radially inward (Figure 4.8). The response can be associated with constraint effects due to the imposed boundary condition (i.e. pin, roller) and, as discussed later, the effect of the gap defect length ( $g/D$ ).

In Figure 4.9, the influence of the boundary conditions (i.e. pin, roller) with an increased gap distance ( $g/D = 25\%$ ) on the section ovality-global curvature relationship is presented. The pipe ovalization-global curvature relationship, for the plane of symmetry (i.e. MID), exhibits an evolution in the local buckling mechanism, which can be identified by the inflection points and gradients (i.e. slope).

As shown in Figure 4.10, the inflection point from linear to non-linear relationship occurs at curvature of  $0.5 \times 10^{-4} \text{ mm}^{-1}$ . The first transition zone can be viewed as the onset of the local buckling. The liner at the plane of symmetry (i.e. MID) starts to buckle outward, which reduces the ovality of the centerline cross-section. The gradient change from inward radial deflection (i.e. Brazier effect) to outward radial deflection (i.e. local buckling toroid as shown in Figure 4.9) occurs at curvature of  $0.75 \times 10^{-4} \text{ mm}^{-1}$ . As the local buckling mechanism develops, from  $0.5 \times 10^{-4} \text{ mm}^{-1}$  to  $0.75 \times 10^{-4} \text{ mm}^{-1}$ , the increase of pipe section ovality slows down and reaches its peak value. After that, the buckling keeps developing. Then the ovality turns back to increase again.

Similar to what is shown in Figure 4.6, the pipe ovality-curvature relationship remains approximately linear at pipe sections away from the local buckling site (i.e. 0.5D and 1.0D), which is consistent with theoretical considerations of the Brazier effect.

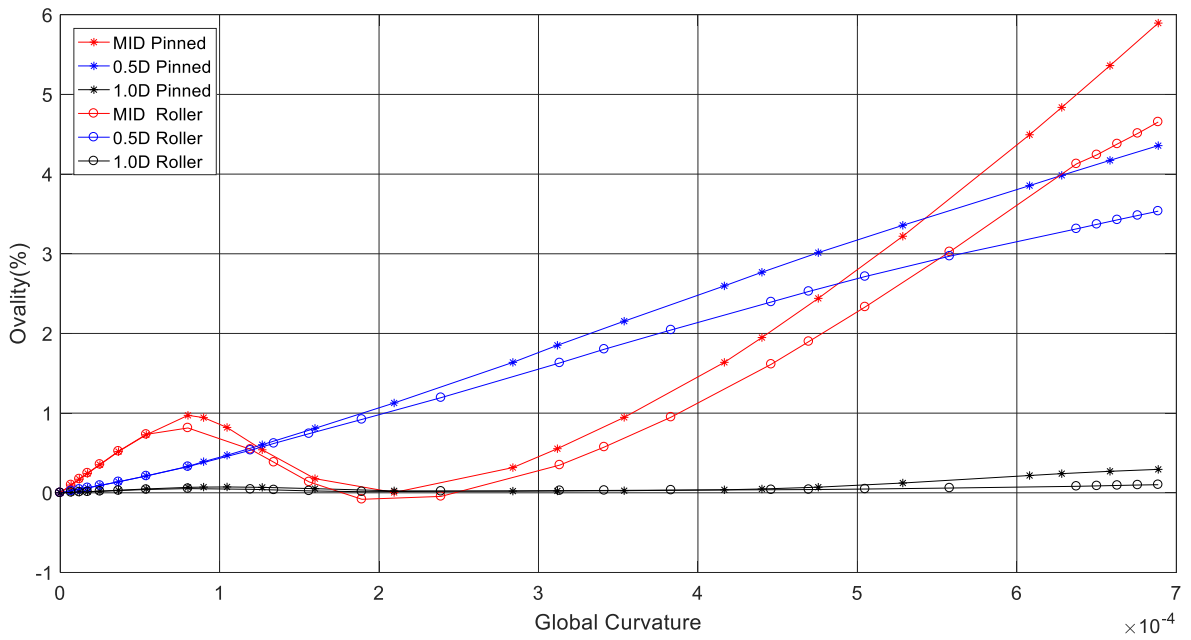
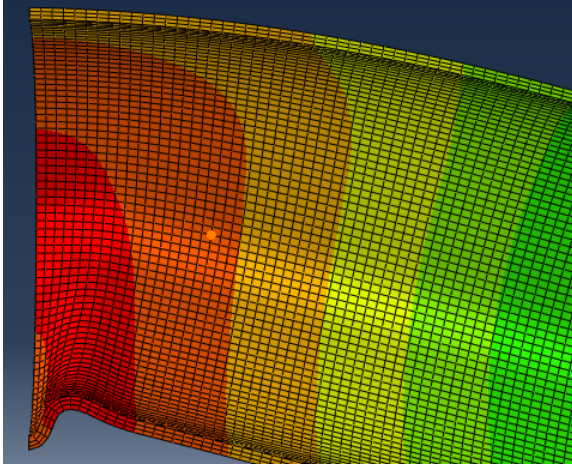


Figure 4.9 Ovality-global curvature relationship ( $g/D = 25\%$ ,  $\sigma_H/\sigma_y = 0.8$ ,  $\mu = 0.4$ )



**Figure 4.10 Total displacement contour of 5D case ( $g/D = 25\%$ ,  $\sigma_x/\sigma_y = 0.8$ ,  $\mu = 0.4$ )**

As shown in Figure 4.9, the bifurcation point (i.e. global curvature of  $2 \times 10^{-4} \text{ mm}^{-1}$ ) also highlights a change in the dominant pipe deformation mechanisms from a radial mode (i.e. Brazier effect) to a longitudinal mode (i.e. local buckle waveform), which is consistent with recent studies on the local buckling response of energy pipelines (e.g. Fatemi and Kenny, 2017; Kenny et al., 2016). The ovalization data also indicates the buckling mechanism remains localized at the pipe mid-length section (i.e. MID), which is highlighted by the non-linear ovalization-global curvature relationship, whereas other pipe section (i.e. 0.5D, 1.0D) exhibit a linear relationship.

Figure 4.11 illustrates the longitudinal distribution of pipe section ovality at the final simulated rotation angle (i.e.  $15^\circ$ ) for the two boundary conditions and gap defect length parameters investigated. The x-axis represents the normalized distance to the pipe centerline (i.e. axial coordinate/total length) and the y-axis is the liner ovality. For the same gap defect length, the longitudinal distribution of section ovality exhibits a similar

pattern for the two different boundary conditions investigated. However, the gap defect length influenced the longitudinal distribution of section ovality, which can be related to the local deformation response mechanisms. Supported by data presented in Figure 4.11, the smaller defect length ( $g/D = 10\%$ ) promoted local section collapse consistent with Brazier effect (Figure 4.8), whereas the longer defect length ( $g/D = 25\%$ ) triggered local buckling with an outward deformation profile (i.e. toroid shape, Figure 4.10).

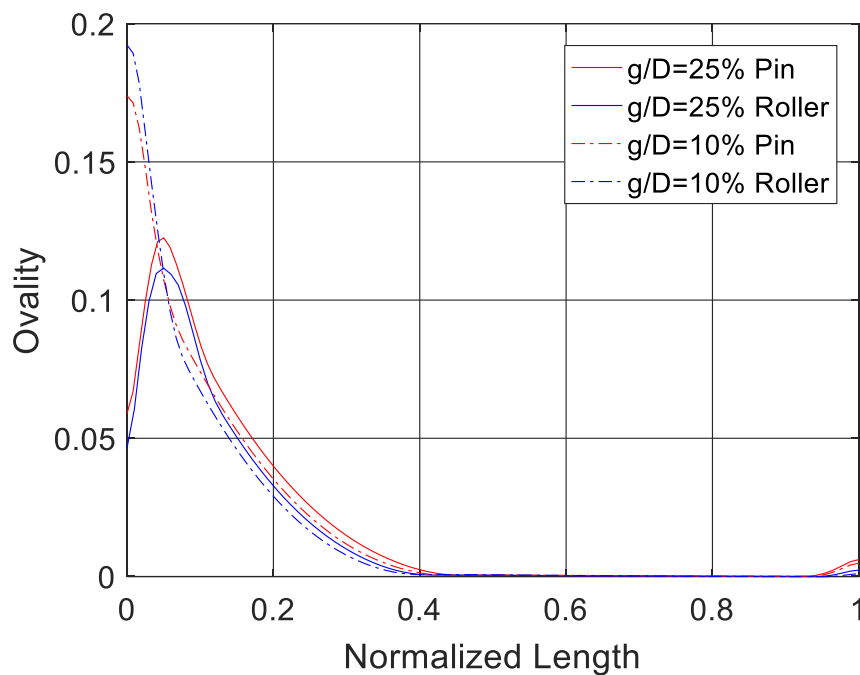


**Figure 4.11 Normalized longitudinal distribution of liner section ovality ( $L = 5D$ ,  $g/D = 10\%$ ,  $25\%$ ,  $\sigma_h/\sigma_y = 0.8$ ,  $\mu = 0.4$ ) for the rotation angle of  $15^\circ$**

As shown in Figure 4.11, due to different local buckling patterns at the plane of symmetry (i.e. MID), the ovality patterns of the liner for different gap lengths are different. For the longer defect length ( $g/D = 25\%$ ), as shown in Figure 4.10, starting from approximately  $0.4D$ , the liner ovalization progressively increases to its peak value and then the liner transfers to local buckling with sine waveform towards centerline. The

outward local buckling mode at the pipe centerline offsets the ovality caused by the Brazier effect, with two local ovality peaks (5% & 12%) highlighting the sine wave profile.

On the other hand, for the shorter defect length ( $g/D = 10\%$ ), the CIPP liner ovalizes from centerline to the location of  $0.4D$  due to Brazier effect. The ovality gradually decreases to zero with increasing distance. The location where the ovality approaches zero is close to that of 25% gap case, which indicates the far field pipe section response is not influenced by either the gap defect length ( $g/D$ ) or the boundary condition, and the bending response is consistent with beam theory.

Figure 4.12 illustrates the local moment-curvature relationship for the models with a pin and a roller boundary condition. The local section moment was calculated as a summation of the nodal force at each node multiplied by the corresponding moment arm to the neutral axis. From the origin, the two curves experience almost identical path until the local curvature exceeds  $1.1 \times 10^{-3}$ . After that, the moment of the pin end case grows faster than that of roller end case. This is due to the higher order effect of the axial force. Apparently, in the late stage of rotation, the axial force developed in pin case is much greater than that of roller case. Consequently, the contribution from axial force becomes significant after the local curvature exceeds  $1.1 \times 10^{-3}$ .

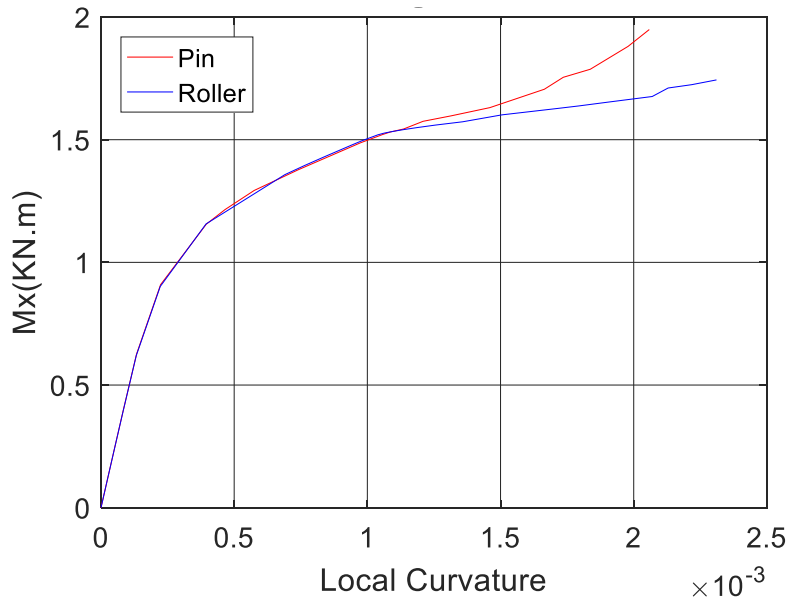


**Figure 4.12 Local moment-curvature relationship for the section at 0.5D ( $L = 5D$ ,  $g/D = 10\%$ ,  $\sigma_h/\sigma_y = 0.8$ ,  $\mu = 0.4$ )**

The deformed shapes of the gap length 15.2 mm and 38.0 mm (i.e.  $g/D = 10\%$ , 25%) exhibit two distinct deformation patterns (shown in Figure 4.13). In the 10% case, the bottom edge of the liner at the centerline deforms inward, whereas it deforms outward in the 25% case. Figure 4.14 shows the normalized profile of the bottom edge of the liner at the end of loading (i.e. rotation angle =  $15^\circ$ ). Four cases of the same gap length under different loading cases (i.e. various  $\mu$  and pressure) demonstrate the same deformation pattern. Therefore, the deformation pattern and failure mechanism depend on the gap length.

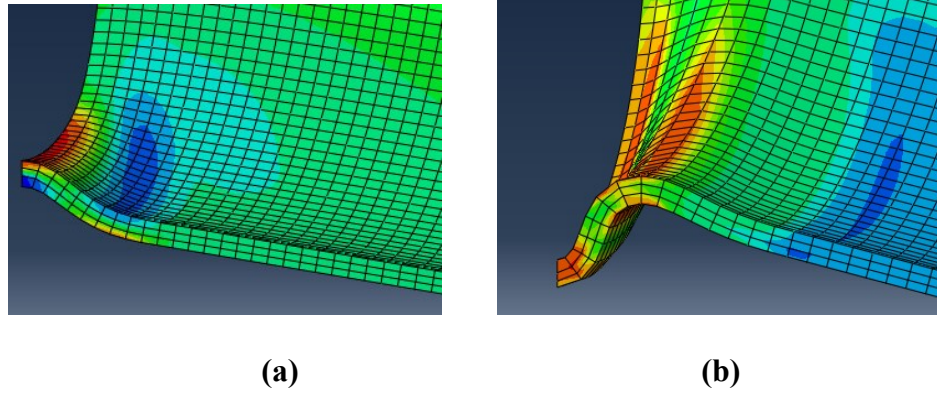


Figure 4.13 Deformed modes (a)  $g/D = 10\%$  for section collapse (Brazier effect) (b)  $g/D = 25\%$  for local buckling mode

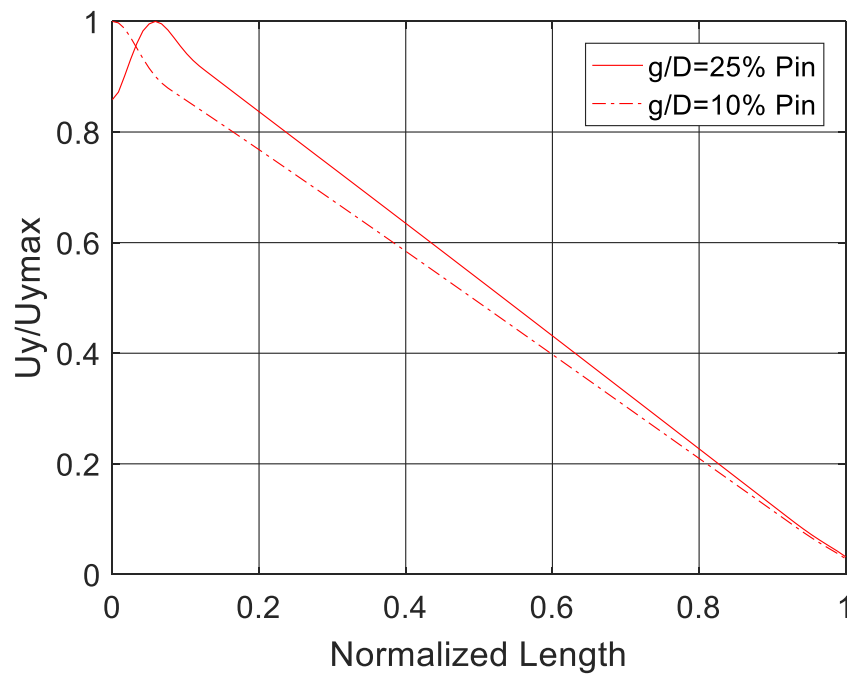
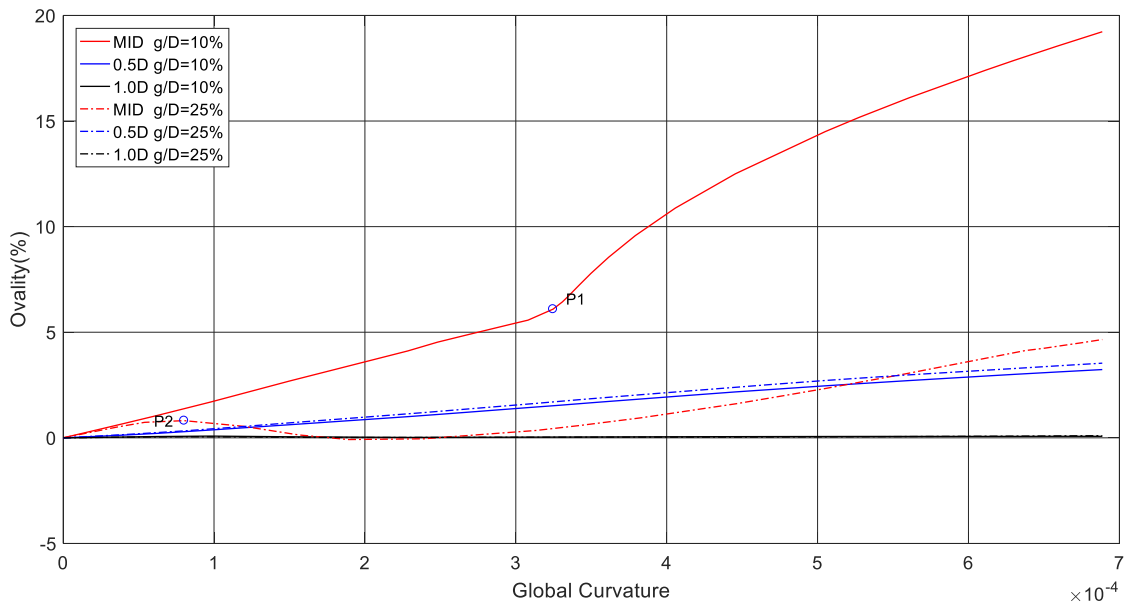


Figure 4.14 Normalized profile of different gap lengths ( $L = 5D$ ,  $g/D = 10\%$ ,  $\sigma_x/\sigma_y = 0.8$ ,  $\mu = 0.4$ )

Figure 4.15 shows the ovality at different locations of different gap lengths. The ovality at  $0.5D$  and  $1.0D$  progressively increases as the curvature increases for both gap lengths. However, the ovality at centerline (i.e. MID) demonstrates distinct characteristic for  $g/D$

= 10% and  $g/D = 25\%$ . In the case of 10% gap, the ovality increases approximately linearly until the global curvature reaches  $3.4 \times 10^{-4}$  (i.e. point P1). Then it shows a dramatic increase with an apparent greater slope. After the global curvature exceeds  $6.0 \times 10^{-4}$ , the slope declines back to the initial slope. In contrast, the ovality of 25% gap initially grows with a smaller slope comparing to that of 10% gap. Before the global curvature reaches  $1.0 \times 10^{-4}$ , the ovality reaches its first peak value 1.0% (i.e. point P2) after which it starts to decline to nearly 0.0%. Then it rises again with approximately the same slope of the initial one. The location where the inflection point occurs depends on the gap length.



**Figure 4.15 Ovality vs global curvature (Roller,  $L = 5D$ ,  $g/D = 10\%$ ,  $25\%$ ,  $\sigma_h/\sigma_y = 0.8$ ,  $\mu = 0.4$ )**

Figure 4.16 shows the global moment-curvature curves of  $g/D = 10\%$  and  $g/D = 25\%$  roller models. P1 corresponds to the turning point of  $g/D = 10\%$  at centerline in the global ovality-curvature, while P2 corresponds to the first peak ovality of  $g/D = 25\%$  at centerline. For the 10% gap case, the slope of global moment-curvature curve changes

from positive to negative at P1 (i.e. the global curvature reaches  $3.4 \times 10^{-4}$ ). After that, the moment experiences a slight decline and then increases again. For the 25% gap case, the slope of global moment-curvature curve shows an obvious decrease at P2 (the global curvature reaches  $0.8 \times 10^{-4}$ ). As the ovality keeps declining between curvature  $1.0 \times 10^{-4} \sim 2.0 \times 10^{-4}$ , the slope decreases rapidly between point G and H. At the same time, the moment keeps growing. After point H, it grows very slowly. According to points P1 and P2, the critical angles for 10% gap case and 25% gap case can be determined as  $7.1^\circ$  and  $1.7^\circ$ , respectively.

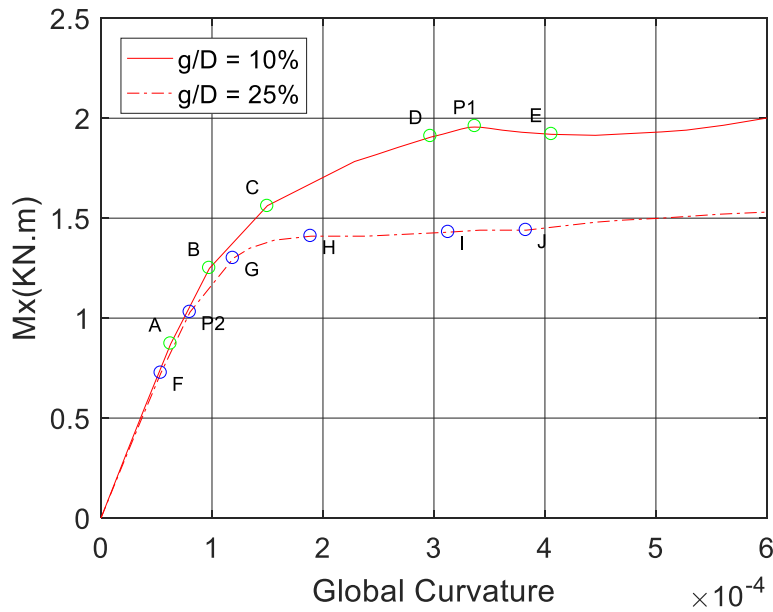


**Figure 4.16 Global moment-curvature (Roller,  $L = 5D$ ,  $g/D = 10\%$ ,  $25\%$ ,  $\sigma_n/\sigma_y = 0.8$ ,  $\mu = 0.4$ )**

Comparing the two global moment-curvature curves, the gap length greatly affects the resistant moment at the end of loading. The moment capacity of the 25% gap case is less than the corresponding 10% gap case by a factor of 0.75. The gap length has a significant impact on the global moment-curvature patterns.

Figures 4.17 and 4.18 show the ovality distribution along the length at certain points corresponding to those points in Figure 4.16. Figure 4.17 shows that in 10% gap case, the maximum ovality always occurs at the centerline (i.e. Brazier effect). By contrast, Figure 4.18 shows that in 25% gap case, the ovality at the centerline grows from ‘F’ to ‘P2’ and then declines to ‘H’. After that, it rises again from ‘H’ to ‘J’. During this process, the location where the maximum ovality occurs moves gradually towards the far end. This can also be observed in the development of profile of bottom edge (shown in Figure 4.19, 4.20).

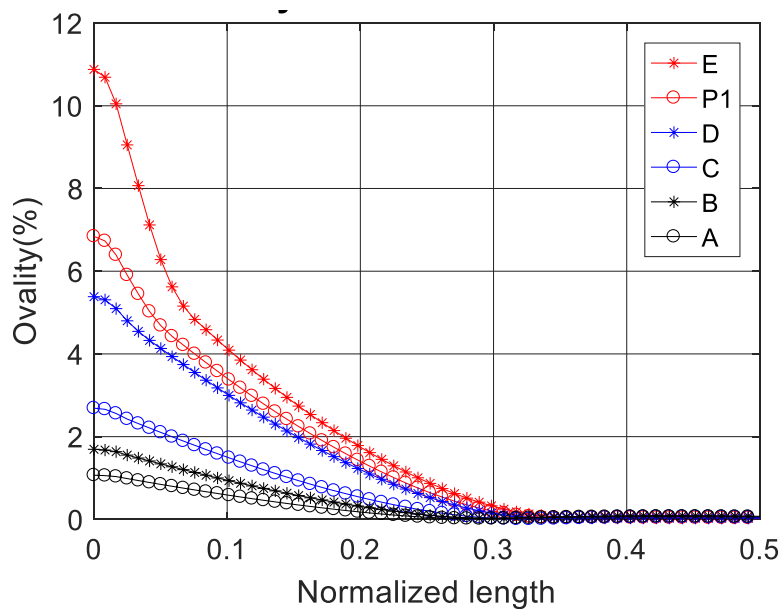


Figure 4.17 Ovality distribution at certain increments (Brazier effect) (Roller,  $L = 5D$ ,  $g/D = 10\%$ ,  $\sigma_x/\sigma_y = 0.8$ ,  $\mu = 0.4$ )

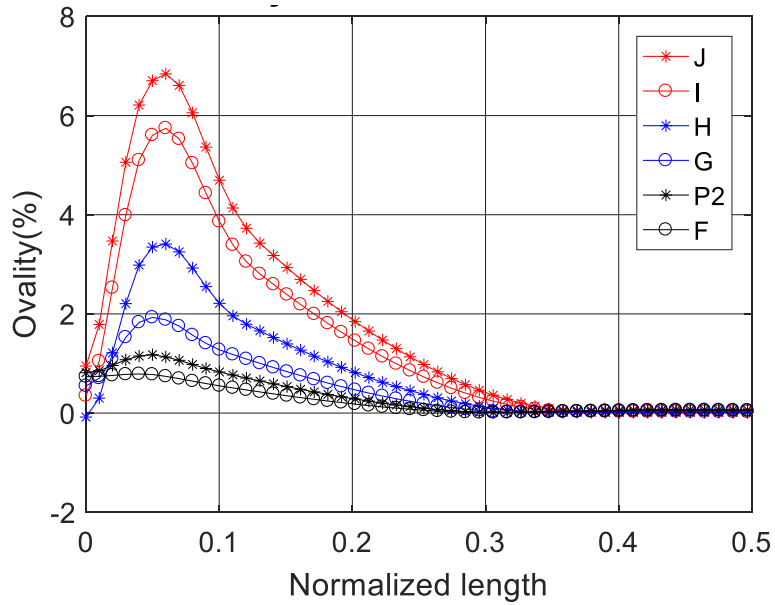


Figure 4.18 Ovality distribution at certain increments (local buckling) (Roller,  $L = 5D$ ,  $g/D = 25\%$ ,  $\sigma_h/\sigma_y = 0.8$ ,  $\mu = 0.4$ )

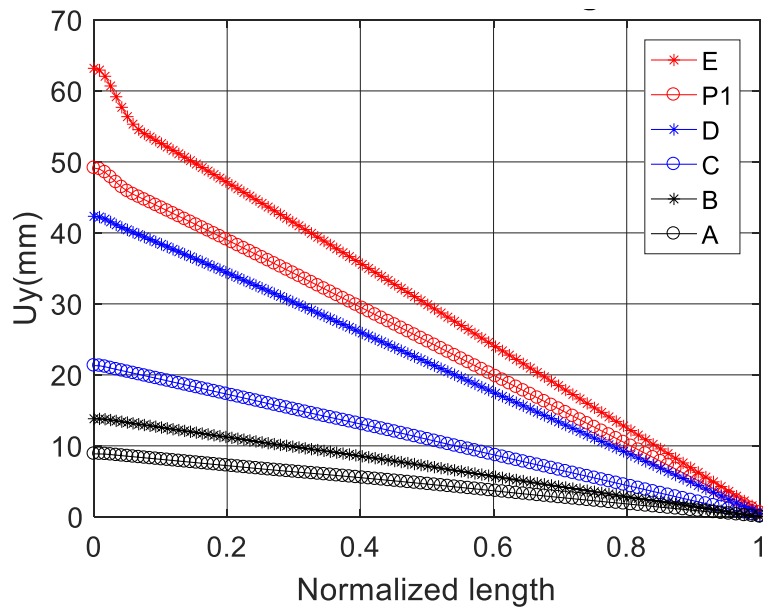


Figure 4.19 Profile of bottom edge (Brazier effect) (Roller,  $L = 5D$ ,  $g/D = 10\%$ ,  $\sigma_h/\sigma_y = 0.8$ ,  $\mu = 0.4$ )

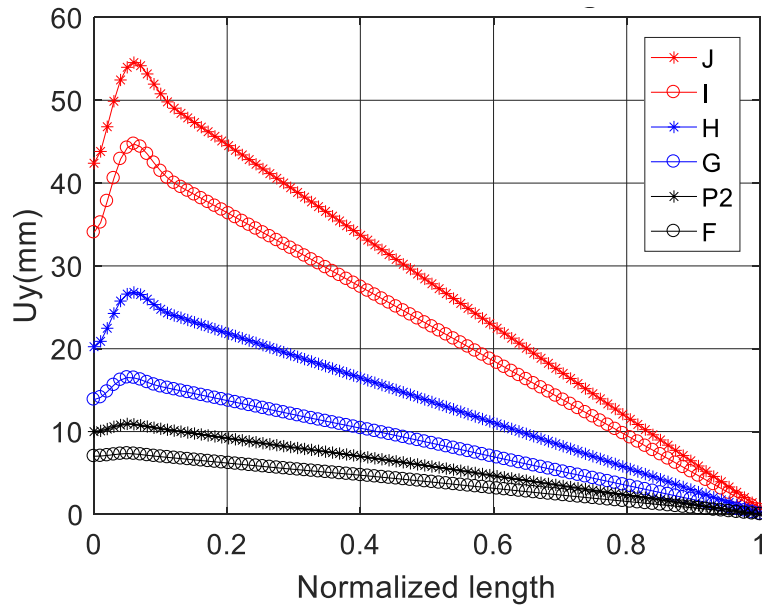


Figure 4.20 Profile of bottom edge (local buckling) (Roller,  $L = 5D$ ,  $g/D = 25\%$ ,  $\sigma_h/\sigma_y = 0.8$ ,  $\mu = 0.4$ )

#### 4.4.3 Influence of Loading Condition and Interface Friction Coefficient

This parameter study examined the influence of loading conditions (i.e. internal pressure) and liner/host pipe interface friction coefficients, as summarized in Table 4.2, on the liner mechanical response. The internal pressure loading conditions were based on the hoop stress, due to internal pressure, to the yield stress ratio ( $\sigma_h/\sigma_y$ ).

Table 4.2 Loading and interface friction study parameters

Hoop stress ratio	Internal Pressure	Friction coefficient
$\sigma_h/\sigma_y$	<i>Pressure (KPa)</i>	$\mu$
0	0	0.2
		0.4
0.8	914	0.2
		0.4

Figure 4.21 shows local moment-curvature of different loading conditions and friction coefficients at the location of  $0.5D$ . All the curves show approximately the same initial stiffness until the local curvature reaches  $0.25 \times 10^{-4}$ . After that, these curves demonstrate two different patterns. For the zero pressure cases (i.e. red color curves), the local moment-curvatures show a plateau with the increase of the local curvature. By contrast, the high pressure cases (i.e. blue color curves) show a bilinear relationship with increasing local curvature, which is due to pressure stiffening. There is slight difference between the results from two different friction coefficients. The moment capacity of the cases with  $\mu=0.2$  is a little higher than that of the cases with  $\mu=0.4$  except in last few increments of the zero pressure cases.

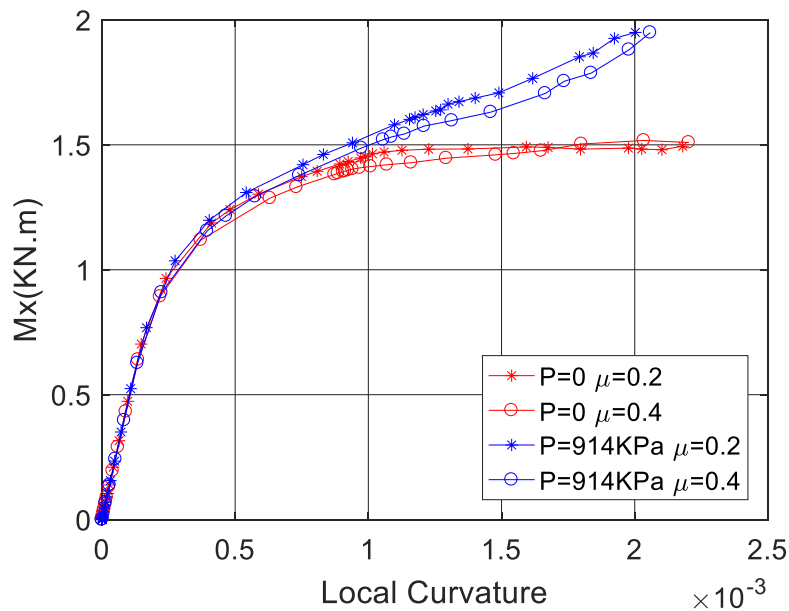


Figure 4.21 Local moment-curvature curves at the location of  $0.5D$  ( $P_{in}$ ,  $L = 5D$ ,  $g/D = 10\%$ )

The effect of interface friction was not significant for each loading condition. When the liner is subjected to the same pressure but with different friction coefficient  $\mu$ , there is slight difference between the ovality of  $\mu=0.2$  and  $\mu=0.4$ . However, it is negligible in the gap region. Pressure stiffening can also be observed in the ovality distribution diagram (Figure 4.22). When the friction coefficient  $\mu$  is the same, the ovality of liner subject to high pressure is much less than that of liner subject to zero pressure. The maximum ovality of  $\sigma_h/\sigma_y=0.8$  at the centerline is approximately half of that of  $\sigma_h/\sigma_y=0$ . The ovality declines sharply with the increase of distance away from the centerline. In the case of  $\sigma_h/\sigma_y=0.8$ , the ovality approaches zero when the distance is close to 1D (20% of 5D). After that, it stays at a steady value until the other end. On the other hand, the ovality becomes a stable value of 2% at the location 1.4D (28% of 5D) in the zero pressure cases.

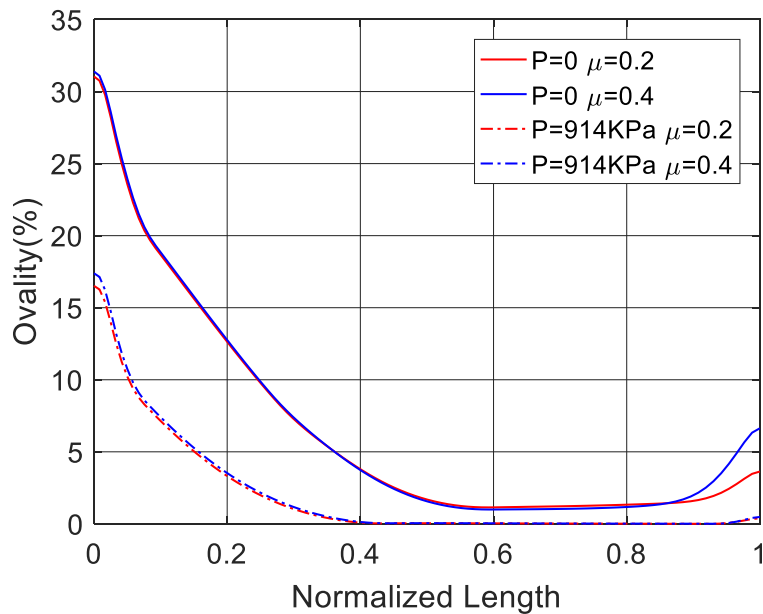


Figure 4.22 Ovality distribution of different cases ( $P_{in}$ ,  $L = 5D$ ,  $g/D = 25\%$ )

#### 4.4.4 Influence of Pipe Length

Due to the computational expense, this study only examined two different lengths (i.e. 5D and 10D) of the liner-pipe system. The results revealed some influence of the pipe length on the mechanical response of the CIPP system. Figure 4.23, 4.24 show the ovality at different locations for two gap lengths. In the case of 10% gap, the curve of 5D at the centerline cross section (i.e. MID) shows a significant increasing rate at global curvature of  $3.4 \times 10^{-4} \text{ mm}^{-1}$ . However, the curve of 10D at the centerline cross section has no such changing point. In contrast, in the case of 25% gap, both curves of 5D and 10D demonstrate a peak value of 1%, which indicates the local buckling of the liner in both cases. Comparing to the curve of 5D case, the ovality of 10D case at centerline cross section shows a little decrease (rather than declining to 0% in 5D case) after first peak value and then increases again with approximately the initial slope. As shown in Eq 4.2, when total angles are the same, the curvatures are inversely proportional to the total length.

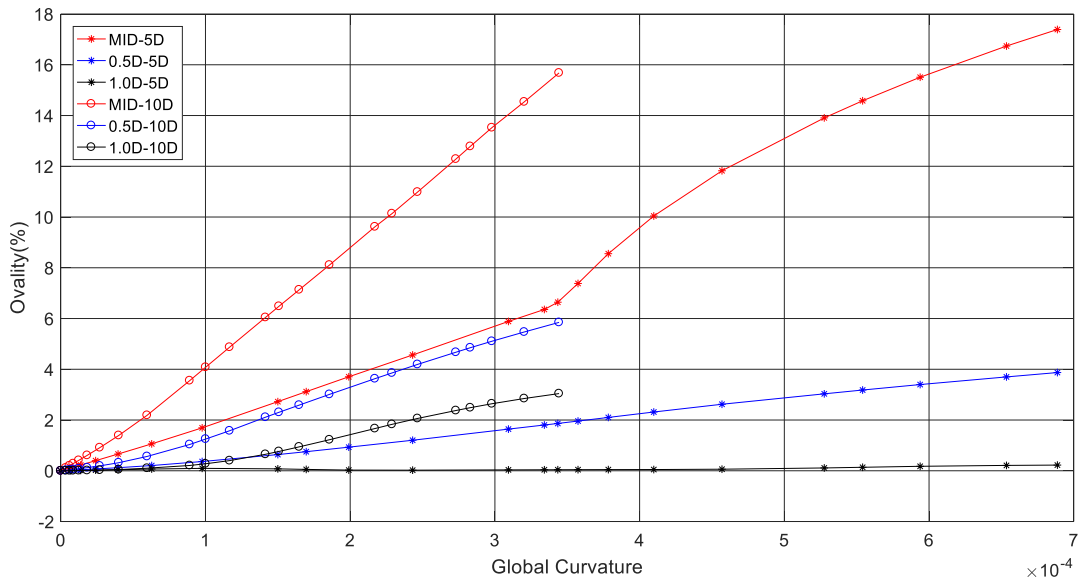
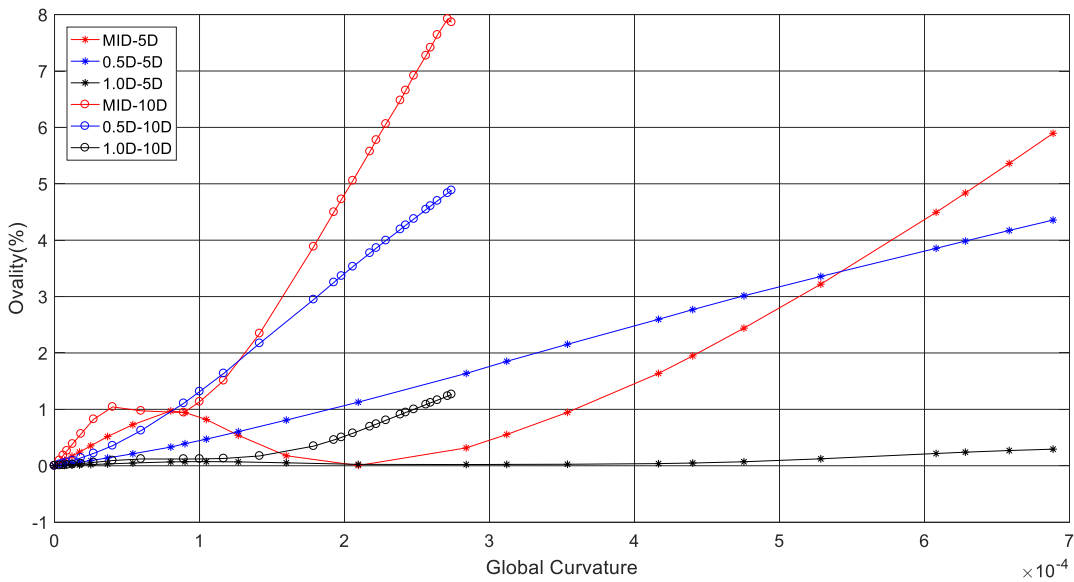


Figure 4.23 Ovality vs global curvatures (Pin,  $g/D = 10\%$ ,  $\sigma_h/\sigma_y = 0.8$ ,  $\mu = 0.4$ )



**Figure 4.24 Ovality vs global curvatures (Pin,  $g/D = 25\%$ ,  $\sigma_h/\sigma_y = 0.8$ ,  $\mu = 0.4$ )**

Figure 4.25 shows the local moment-curvature curves of 25% gap pin model for 5D and 10D lengths at different cross sections (i.e. 0.5D and 0.75D). At the same cross section location, the liners of 5D and 10D cases exhibit the same initial stiffness until some point between local curvature of  $0.2 \times 10^{-3}$  and  $0.3 \times 10^{-3}$ . Then the stiffness gradually decreases for both pipe lengths. Both curves present bilinear relation but with different final stiffnesses. The final stiffness of 10D case is significantly greater than that of the 5D case. Comparing the responses at different cross section locations, the initial stiffness at 0.5D location is greater than that at 0.75D.

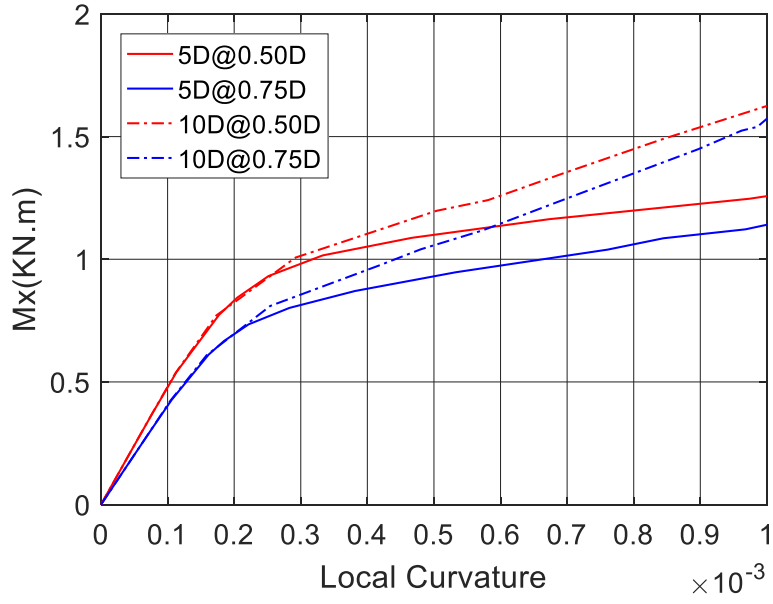


Figure 4.25 Local moment-curvature curves (Pin,  $g/D = 25\%$ ,  $\sigma_h/\sigma_y = 0.8$ ,  $\mu = 0.4$ )

## **Chapter 5: Conclusions and Recommendations**

### **5.1 Conclusions**

The deterioration of ageing water infrastructure system has drawn increasing attention from the public. This is due to the waste of water through leak paths (i.e. loss of 10% to 30% of the total water supplied) and the potential threat to public health and safety (i.e. penetration of contaminants through the deteriorated pipelines into potable water systems). Common failure modes include pitting, splitting, cracking, circumferential breaks and joint rupture. Trenchless rehabilitation technologies provide economic and technical advantages (e.g. reduced disruption of water service and public traffic) relative to conventional open trench methods. As a result, CIPP liners have become one of the primary methods to improve the integrity of existing water pipeline systems with local damage and deterioration that affects serviceability.

In response to service loads (e.g. internal pressure) and geohazards (e.g. frost heave), the CIPP liner may interact with features promoting stress concentrations (e. g. ring fracture, rotated pipe joints, lateral connections), or inherent defects (e.g. deteriorated pipe). The liner mechanical response is a function of the external pipe stiffness and damage state, joint condition, springline depth, soil mechanical properties, and load effects (e. g. operational, surface and geohazards). An assessment of the liner performance and condition is required to assess integrity and provide evidence for decision making within rational asset management practices for civil infrastructure. Consequently, there is a need to better understand the mechanical response of CIPP liners, across a range of practical

design parameters and defect features within the host pipe, and evaluate potential failure modes and mechanisms of the CIPP liner.

In this study, continuum finite element modelling procedures are used to examine the mechanical response and performance of a CIPP liner under different limit states (i.e. burst, global and local flexure) for pressure pipe. Two types of local defects (i.e. circular void and circumferential crack) were considered in the host pipe with a relatively high elastic modulus (i.e. comparatively rigid host pipe). Circular void defects can be caused by general corrosion; whereas, circumferential cracks (i.e. gap defect) can be generated by corrosion, ring splitting or relative axial displacement. In terms of load conditions, internal pressure is employed in the circular void model, while internal pressure and flexural loading are applied in the circumferential gap model.

For the circular void (i.e. local through wall area defect in the host pipe) analysis cases, the sensitivity study investigated the CIPP liner outside diameter to CIPP wall thickness ratio ( $D/t$ ), hoop stress due to internal pressure and yield stress ratio ( $\sigma_h/\sigma_y$ ), cast iron/CIPP liner interface friction coefficient, and defect diameter to pipe diameter ratio ( $d/D$ ). A performance envelope was developed that was consistent with current engineering practice and illustrated a class of parameters where an engineering condition assessment would be required to evaluate the CIPP liner performance. The material yield behaviour was observed for the higher liner dimension ( $D/t > 60$ ) and hoop stress to yield ratios ( $\sigma_h/\sigma_y \geq 0.6$ ). The limit state can be governed by axial tension rather than ring tension when void ratios are greater than 0.4. As the void ratio ( $d/D$ ) increases, the hoop

stress tends to behave as an unconstrained liner in the radial direction. The hoop stress decreased in magnitude for each hoop stress ratio ( $\sigma_h/\sigma_y$ ) examined. The results suggest for pipe with greater damage, as the void ratio ( $d/D$ ) increases, then the the von Mises yield stress may be a better performance measure. A fully bonded host pipe/CIPP liner interface reduces the axial, hoop and effective stress.

A numerical study also examined the influence of a local gap defect (i.e. circumferential or radial defect) in the host pipe with the liner subject to internal pressure. Several probable mechanisms can induce longitudinal tensile stresses into the water mains, such as changes of water and ground temperature, volume change of clays due to seasonal wet and dry conditions, inadequate support or expansion of clays underneath. Circumferential break makes up of the majority water main breaks and the length of the gap could increase over time due to the corrosive external environment. For a stiffer liner the axial stress increases with the increase of gap length in an approximately linear relation whereas for a softer liner, the axial stress increases nonlinearly with the increase of gap length. Across these examined cases, the axial and equivalent (von Mises) stress state was elastic. The normalized displacements under different hoop stress ratio with the same  $D/t$  ratio exhibited similar deflection patterns. In contrast, for different  $D/t$  ratios (i.e. related to pipe stiffness) the CIPP liner response exhibited distinct deflection patterns. The influence of interface friction (i.e.  $\mu = 0.2$  &  $0.4$ ) was to develop an ‘anchor point’ or ‘virtual anchor’ that allowed for the far-field boundary condition to be naturally established within the modeled pipe segment length. The interface friction did not

influence either the stress state and deflection response for the analysis cases investigated.

Finally, a numerical parameter study investigated the influence of a local gap defect in the host pipe on the mechanical performance of the CIPP liner when subjected to internal pressure and end rotation, which may be due to differential ground movement (e.g. frost heave, fault motion). The importance of pipe length, boundary conditions, gap length, loading condition and interface friction coefficient on the CIPP liner behaviour was explored. For the parameters investigated, the boundary conditions (i.e. pin, roller) did not have any significant impact on the liner deformational response (e.g. section ovality) but did influence the post-peak local moment-curvature behaviour. The defect gap length had an impact on the CIPP liner deformation pattern (i.e. mode response) at the pipe mid-length, plane of symmetry. For the relatively shorter gap length analysis case (i.e.  $g/D = 10\%$ ) the bottom edge of the liner deformed radially inward (i.e. Brazier type cross-section collapse), whereas for the longer gap defect length analysis case (i.e.  $g/D = 25\%$ ) the liner deformed radially outward (i.e. toroid buckle). The defect gap length, which can be related to discontinuities in local stiffness and stress concentration effects, influenced the section ovality-global curvature relationship and decreasing moment capacity (i.e. lower section modulus) with increasing gap defect length. The host pipe/CIPP liner interface friction coefficient ( $\mu = 0.2$  &  $0.4$ ) had a negligible influence on the CIPP liner response with the same model parameters (i.e. pipe length, defect length, internal pressure, boundary conditions). However, internal pressure effects (i.e. pressure factor of  $\sigma_h/\sigma_y = 0$  &  $0.8$ ) had a significant influence on the CIPP liner mechanical response.

Higher pressure factors reduced the section ovalization magnitude due to pressure stiffening effects. The local moment-curvature relationship for no internal pressure exhibited a nonlinear response whereas for high internal pressure load case, a bilinear response defined the moment-curvature relationship. The pipe segment length being modelled had a significant impact on the CIPP liner section ovality-global curvature relationship, particularly at the plane of symmetry, which is governed by local buckling deformation mechanisms, and with respect to the onset of nonlinear behaviour. The modelled pipe segment length did not influence the elastic global moment-local curvature relationship but did have an influence beyond the bifurcation point that resulted in different tangent stiffness response. In this study, only symmetric loading conditions were considered. The mechanical response of the liner may be different if asymmetrical loading conditions were applied, such as differential out of plane forces, local geometric imperfections or relative ground motion for a buried pipe system.

## **5.2 Recommendations**

### **5.2.1 Overview**

Future studies should address the potential limit state conditions for the CIPP liner with wider scope that integrates the findings across investigations. The recommendations can be broadly classified into physical modelling studies, numerical modelling studies and synthesis for the development of engineering practice and guidance.

### **5.2.2 Physical Modelling Studies**

Constitutive relation is the essential parameter for engineering design and numerical modelling. The physical experiments performed by Brown et al., (2008) only conducted

tensile tests in both longitudinal and circumferential directions. For further study, compression and through thickness shear stress-strain relationships also need to be identified.

In this study, a range of friction coefficients of host-pipe/CIPP interface was examined. However, the friction coefficient of the interface for two defined materials is usually a constant. Physical experiments need to be performed to determine the precise value for the interface friction coefficient and factors that may influence variability (e.g. host pipe damage state, axial or radial constraints, loading condition or stress state). In addition, shear strength-shear strain properties of the CIPP liner need to be investigated since this could be another potential limit state (i.e. shear failure) during the service lifespan.

Pipelines and shell structures are imperfection sensitive. These imperfections can be caused by a variety of factors, such as spatial variation in material properties, residual stress state, and geometric perturbations (Fatemi et al., 2007). Geometric imperfections may include variations in wall thickness, CIPP liner diameter, and installation factors (e.g. development of a local wrinkle due to an oversized liner). The influence of geometric imperfections, which may be due to in-situ conditions (e.g. host pipe ovality, local damage) and fabrication (e.g. local wrinkle in CIPP liner), should be established through physical measurements and investigations.

Laboratory tests can provide basic engineering information on component mechanical behaviour (e.g. isotropic or orthotropic constitutive relationships). Physical models can

provide insight on the system response and failure mechanisms, which is a practical and needed approach to calibrate numerical models simulating CIPP liner mechanical response. This will provide confidence in the numerical modelling procedures used to assess potential CIPP liner limit states (e.g. Allouche et al., 2005) and investigate other factors (e.g. influence of soil backfill restraint on pipe curvature response when subject to global loading) that may influence the CIPP liner mechanical response.

### **5.2.3 Numerical Modelling Studies**

Due to computational expense and model complexity, the parameters investigated in this study are limited to a certain range. In order to model the CIPP system in reality more precisely and accurately, the study can be extended and discussed with respect to the following aspects of parameters, which include pipe segment length modal and physical geometric imperfections, boundary conditions and geotechnical backfill conditions.

Two lengths of pipe were considered subjected to the limitation of computational expense. Apparently, the length effect has a considerable influence on the response of the CIPP system. It is expected that the response may vary if the length was increased. Considering the computational cost, extending the model with three-dimensional pipe elements or beam elements is a reasonable method to model actual stiffness of the liner and the pipe.

Local geometric imperfections (i.e. variation in CIPP liner wall thickness, ovality) were not considered in the numerical analysis. Future investigations should explore the

significance of modal imperfections, to initiate bifurcation and stabilize the numerical solution, and physical imperfections (i.e. natural, inherent defects) that may influence the mechanical response and deformation mechanisms.

End rotation was applied at the far field boundary condition, which did not account for either the axial or flexural stiffness of the liner and host pipe, and did not account for the geotechnical restraint of the soil backfill. A 5D long model with fixed-fixed end boundary conditions indicated the host pipe might experience large forces that may exceed the material yield strength. Enhancing the numerical modelling procedures to account for these boundary condition effects may identify other host pipe failure modes (e.g. tension splitting) that may further affect or impair the CIPP liner mechanical response. The significance of pipe length and end boundary conditions on the local buckling response of energy pipelines has been demonstrated in recent studies (e.g. Fatemi et al., 2007; Kenny et al., 2016).

The interaction between the soil surface and the cast iron pipe surface was not included in this study. However, the soil has a significant influence on the response of the CIPP system. As discussed by Trickey, (2005), trench backfill conditions greatly affect the deflection and moment of the cast iron pipe. In previous research, the soil spring was commonly used to account for the soil effect. The pipe-soil reaction modulus can be determined depending on the specific type of the soil with elastic properties or empirical relationships (Rajani, 1996). The drawback of this model is that it can hardly account for the actual uneven contact between the pipe and the soil. Therefore, the stress distribution

in the pipe and soil is not accurate. Under general bending loads, the presence of the soil will limit or affect the pipe curvature and influence the local distribution of moments or stress depending on the discontinuity dimensions. The three-dimensional model can overcome this problem by modeling the soil with solid elements and adding contact pair between the pipe and the soil. Nevertheless, this will add boundary nonlinearity into the model and meanwhile, the plasticity of the soil itself should be considered under large deformation. These factors will increase the numerical model and solution complexity, increase requirements for the acquisition of additional engineering data (e.g. constitutive relationships, interface behaviour), and drive the need to conduct physical modelling for calibration of the computational procedures with inherent confidence.

#### **5.2.4 Engineering Practice**

The integrated outcome of these future studies should aim for the development of improved engineering practices and guidance documents that may advance civil engineering design activities, enhance code or standards, and support governments and regulatory bodies for the management of these systems.

## References

- Allouche E.N., Bainbridge, K., Moore, I.D., (2005). "Laboratory examination of a cured in place pressure pipe liner for potable water distribution system." North American Society of Trenchless Technology (NASTT), NO-DIG 2005, Paper D-3-04, 10p.
- ASTM F1216 (2016). Standard Practice for Rehabilitation of Existing Pipelines and Conduits by the Inversion and Curing of a Resin-Impregnated Tube. ASTM International, 8p.
- ASTM F1743 (2017). Standard Practice for Rehabilitation of Existing Pipelines and Conduits by Pulled-in-Place Installation of Cured-in-Place Thermosetting Resin Pipe. ASTM International, 8p.
- AWWA (2014). M28 Rehabilitation of Water Mains, Third Edition. American Water Works Association (AWWA), ISBN 9781583219706, 132p.
- Brown, M., Fam, A., Moore, I.D., (2008). "Material characterization of components and assembled behavior of a composite liner for rehabilitation of cast iron pressure pipes." *Polym. Eng. Sci.* 48(7):1231-1239, doi:10.1002/pen.
- Brown, M., Moore, I.D., Fam, A., (2014). "Performance of a cured-in-place pressure pipe liner passing through a pipe section without structural integrity." *Tunnelling and Underground Space Technology*, Volume 42:87-95, doi: 10.1016/j.tust.2014.01.005.
- Brazier, L., (1927). "On the flexure of thin cylindrical shells and other thin sections." *Proc. R.Soc. Lond. A* 116 (1927) 104-114.
- Bueno, S.M., (2011). "CIPP Turns 40." *Trenchless technologies*, February 10, 2011.
- Dorey, A.B., D.W. Murray and J.J.R. Cheng (2006). "Critical buckling strain equations for energy pipelines – A parametric study." *Journal OMAE*, Vol.128, pp.248-255.

- Fatemi, A., Kenny, S., and Taheri, F., (2007). "Continuum finite element methods to establish compressive strain limits for offshore pipelines in ice gouge environments." Proc., OMAE2007-29152, 7p.
- Fatemi, A., Kenny, S., Taheri, F., Duan, D.-M., and Zhou, J. (2010). "End boundary effects on local buckling response of high strength linepipe." Proc., IPC2010-31397, 8p.
- Fatemi, A. and Kenny, S., (2017). "Parameters affecting local buckling response of high strength linepipe." J. OMAE-15-1119, 139(3):15p., doi: 10.1115/1.4035995.
- Hanif, W. and Kenny, S. (2013). "Assessment of parameters influencing mechanical response of constrained and unconstrained dents using finite element modeling." Proc., OMAE2013-10762:10p.
- Huo, X., Kenny, S., and Hussein, A., (2016). "Evaluation of back-bevel and counterbore-taper unequal wall thickness transition joint designs." Proc., IPC2016-64390:12p.
- Jeyapalan, J.K., (2003). Future of America's Water Is in our hands. New Pipeline Technologies, Security, and Safety, p1026-1032, doi:10.1061/40690(2003)52
- Kenny, S., Gordon, R. and Swank, G., (2016). "Alternative compressive strain capacity performance limits for strain based design applications." Proc., IPC2016-64578:10p.
- Konrad, J.M., (2001). Cold Region Engineering, Chapter 20, Ed. R. K. Rowe Geotechnical and Geoenvironmental Engineering Handbook. Norwell, Massachusetts, Kluwer Academic Publishers.
- Kyriakides, S. and Corona, E., (2007) Mechanics of Offshore Pipelines: Vol. I Buckling and Collapse. Elsevier, Amsterdam, The Netherlands, pp. 196-224.

- Makar, J.M., Desnoyets, R., MacDonald, S.E., (2001). Failure Modes and Mechanisms in Gray Cast Iron Pipe. Underground Infrastructure Research, Waterloo, Ontario, June 10-13 (Report NRCC-44218, Institute for Research in Construction, NRC, Ottawa), Canada.
- Palmer, A.C., Ling, M.T.S., (1981). "Movement of submarine pipelines close to platforms." Proceedings of the 13th offshore Technology conference, OTC 4067, 1981. p.17–24
- Paradkar, A.B., (2012). An Evaluation of failure Modes for Cast Iron and Ductile Iron Water Pipes. MSc Thesis, University of Texas at Arlington, December 2012, 82p.
- Rajani, B., Zhan, C. and Kuraoka, S., (1996) "Pipe-soil interaction analysis of jointed water mains." Canadian Geotechnical Journal, 33, pp.393-404.
- Seica, M.V., Packer, J.A., Grabinsky, M.W.F., and Adams, B.J., (2002). "Evaluation of the properties of Toronto iron water mains and surrounding soil." Can. J Civ. Eng., 29(2):222-237, doi: 10.1139/L01-090.
- Timoshenko, S.P. and Gere, J.M., (1961). Theory of Elastic Stability, ISBN 0070647496, 541p.
- Trickey, S.A., Moore, I.D., Balkaya, M., (2016) "Parametric study of frost-induced bending moments in buried cast iron water pipes." Tunnelling and Underground Space Technology 51 (2016) 291–300., doi: 10.1016/j.tust.2015.10.028.
- Trickey, S.A., (2005). Three Dimensional Finite Element Modeling of Buried Pipes Including Frost Action. M.Sc. Thesis, Department of Civil Engineering, Queen's University, Kingston, Ontario, Canada.

Ugural, A. C, Fenster, Saul K., (2003) Advanced Mechanics of Materials and Applied  
Elasticity, Fourth Edition, ISBN 0-13-047392-8, pp.315-316

## Appendices

### Appendix A Mesh topology, sensitivity and calibration studies

In the development of the calibrated modelling procedures, which were based on the studies by Brown et al. (2008, 2014), a sensitivity study was conducted to assess the effects of element type, mesh density on the pipe surface and through thickness, and material behaviour.

In terms of element type selection, the structural shell (S4, S4R) and general purpose, three-dimensional, continuum, 8-node linear brick (C3D8I) elements were used to discretize the CIPP liner. As shown in Figure A.1 and Figure A.2, in comparison with the shell element (S4R) model results, the C3D8I element provides an improved response relative to the prediction by Brown et al. (2012)<sup>1</sup>. The material behaviour was orthotropic.

---

<sup>1</sup> Brown, M., Moore, I. and Fam, A. (2012). “Design for Bending of Polymer Pressure Pipe Liners Spanning Between Intact and Damaged Pipe Sections.” Presentation at the International Conference on Underground Infrastructure Research..

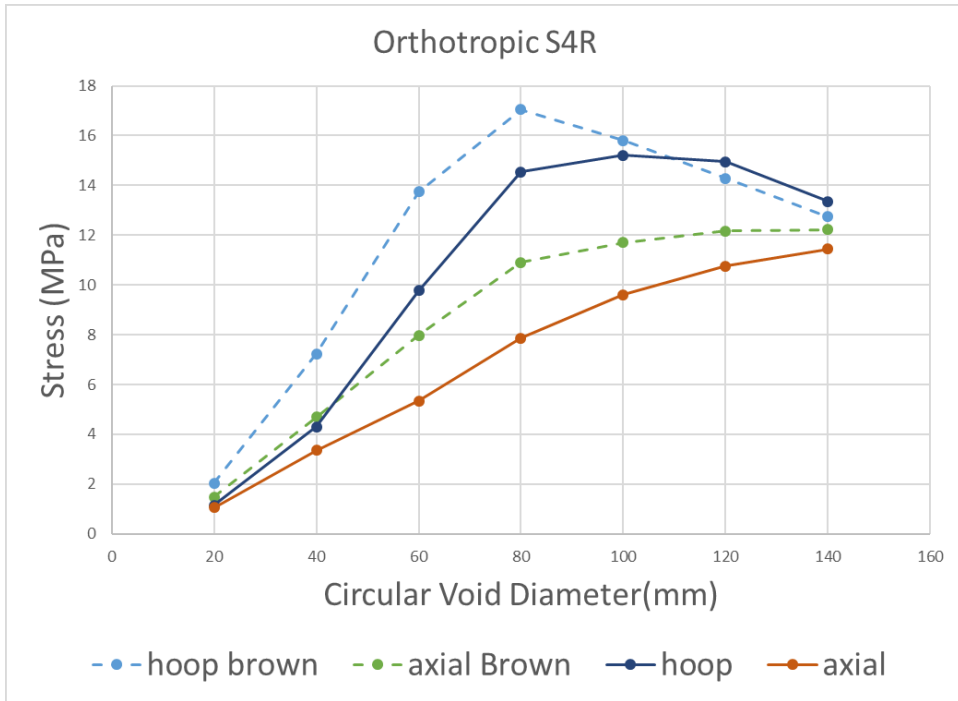


**Figure A.1 Comparison of FEA simulations using S4R elements in this study with the numerical prediction of Brown et al. (2012)**

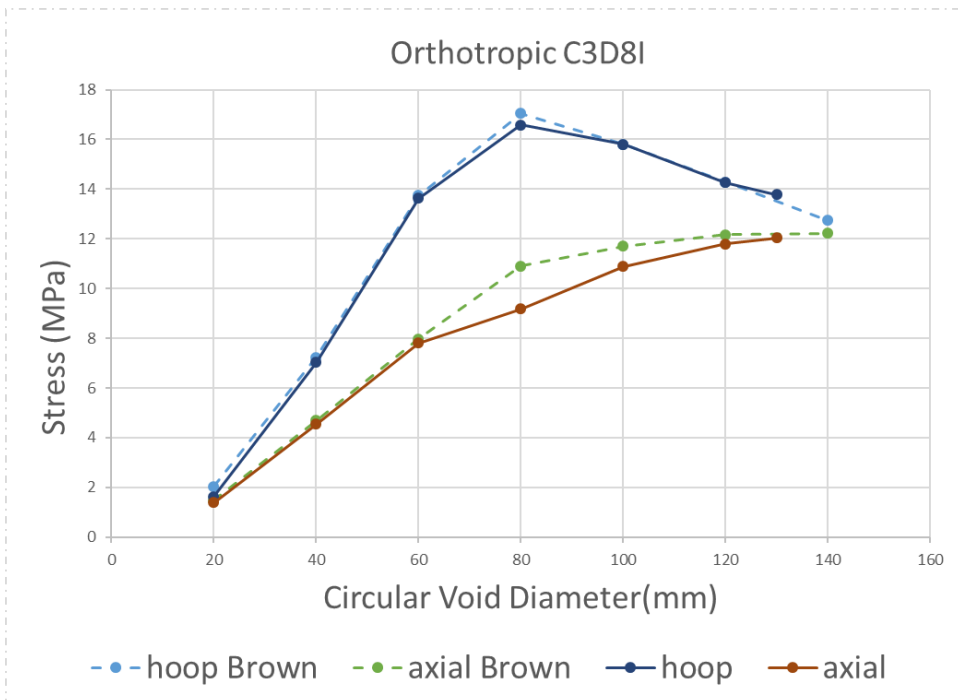


**Figure A.2 Comparison of FEA simulations using C3D8I elements in this study with the numerical prediction of Brown et al. (2012)**

The influence of element discretization in the through thickness direction for the CIPP liner was also investigated (Figure A.3 to Figure A.5). For the sensitivity analysis of through thickness mesh discretization, the number of elements used along a single path for each direction in the CIPP liner and host pipe; that is radial (i.e. through thickness), circumferential (i.e. hoop) and longitudinal (i.e. pipe length), is summarized in Table A.1. The study by Brown et al. (2012) appears to have used the 10-node quadratic tetrahedron (C3D10). In comparison with the numerical predictions by Brown et al. (2012), the FE models with 2 or 3 elements through thickness exhibited an improved response over the single element layer model. In this study, the host pipe was modelled using two layers through thickness and was relatively rigid in comparison with the more compliant CIPP layer. As shown in Figure A.4 and Figure A.5, for circular void diameters greater than 100 mm, there is a discrepancy between the prediction in this study with that of Brown et al. (2012) simulations. These differences may be related to differences between the two studies including element type, element response or performance due to mesh topology (e.g. shape factor, aspect ratio, face angle) and data sampling procedures (e.g. integration point, nodal average, area average).

**Table A.1 Numbers of elements used in each direction**

<b>Location</b>	<b>Radial</b>	<b>Circumferential</b>	<b>Longitudinal</b>
Liner	2 or 3	168	525
Host pipe	2	54	176

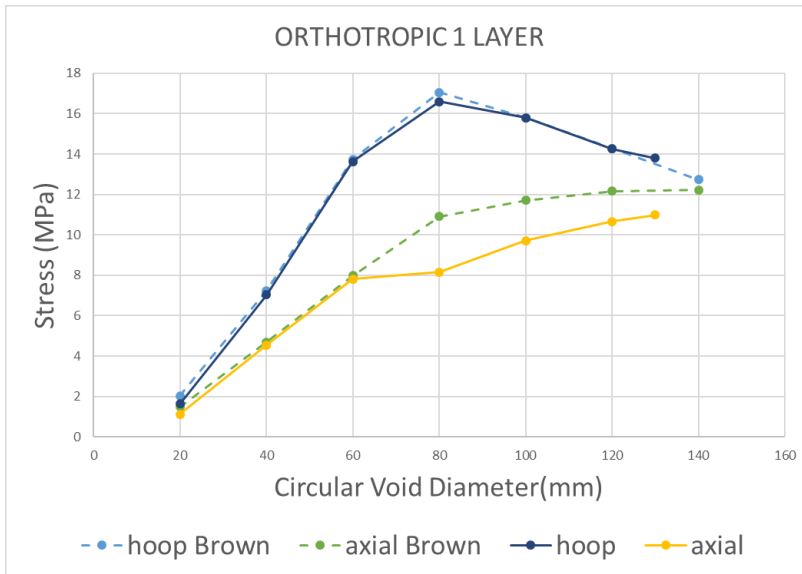


Figure A.3 Comparison of one layer model with Brown et al. (2012) predictions

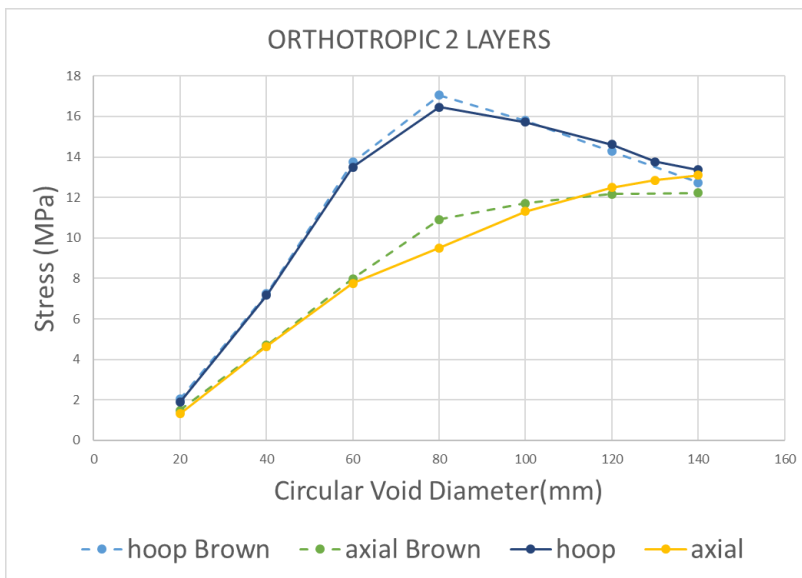
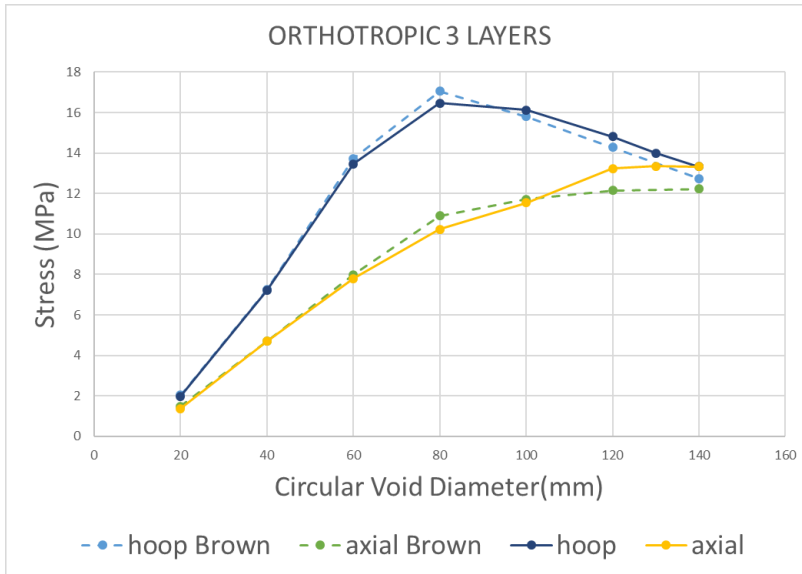


Figure A.4 Comparison of two layer model with Brown et al. (2012) predictions



**Figure A.5 Comparison of the three layer model with Brown et al. (2012) predictions**

The model pipeline length was selected to not be less than five times the nominal diameter. This was based on experience from other studies on the interaction between the pipe mechanical response and effects of end boundary conditions for energy pipelines subject to indentation and flexure (e.g. Dorey et al., 2006; Fatemi and Kenny, 2017; Fatemi et al., 2010; Hanif and Kenny, 2013).

Finally, the numerical predictions for axial stress and Poisson effects at the end boundary condition were compared with the theoretical solution (Eq A.1) for thick walled cylinder using Lamé's expression (Ugural and Fenster, 2003).

$$\sigma_h = \frac{(a^2 p_i - b^2 p_o)}{b^2 - a^2} + \frac{(p_i - p_o) a^2 b^2}{(b^2 - a^2) r} \quad \text{Equation A.1}$$

$a$ —inner radius

$b$ —outer radius

$r$ —location at which the displacement is calculated

$p_i$ —internal pressure

$p_o$ —external pressure

Results from the numerical simulations and theoretical calculations are summarized in Table A.2. The external pressure is mobilized by the relatively rigid host pipe surrounding the CIPP liner, which provides radial constraint during pressurization. The end boundary conditions allow for unconstrained or free radial motion of the host pipe and CIPP liner where the boundary condition is applied through a common reference point. For the calibration analysis the inner radius ( $a$ ) was 73.849 mm and the outer radius ( $b$ ) was 77.724 mm. The comparison indicates end effects from the boundary condition did not have any significant influence on the predicted stress response.

**Table A.2 Hoop stress through liner thickness**

Internal Pressure (MPa)	External Pressure (MPa)	Sampling Location (mm)	Theoretical Solution (Eq A.1)	FEA Prediction	Relative Error (%)
$p_i$	$p_o$	$r$			
0.200	0.193	73.9	-0.0478	-0.0471	1.5
0.200	0.193	75.1	-0.0504	-0.0502	0.4
0.200	0.193	76.4	-0.0528	-0.0527	0.2
0.200	0.193	77.7	-0.0552	-0.0555	-0.5